Title

Effects of Nanoscale Structure on the Magnetism and Transport Properties of Chromium and Chromium-Aluminum Alloys

Permalink

https://escholarship.org/uc/item/48g2x372

Author

Boekelheide, Zoe Austin

Publication Date

2011

Peer reviewed|Thesis/dissertation

Effects of Nanoscale Structure on the Magnetism and Transport Properties of
Chromium and Chromium-Aluminum Alloys

by

Zoe Austin Boekelheide

A dissertation submitted in partial satisfaction of the

requirements for the degree of

Doctor of Philosophy

in

Physics

and the Designated Emphasis

in

Nanoscale Science and Engineering

in the

Graduate Division

of the

University of California, Berkeley

Committee in charge:

Professor Frances Hellman, Chair
Professor Steven Louie
Professor Yuri Suzuki

Fall 2011

Effects of Nanoscale Structure on the Magnetism and Transport Properties of
Chromium and Chromium-Aluminum Alloys

Copyright 2011

by

Zoe Austin Boekelheide

Abstract

Effects of Nanoscale Structure on the Magnetism and Transport Properties of
Chromium and Chromium-Aluminum Alloys

by

Zoe Austin Boekelheide

Doctor of Philosophy in Physics

and the Designated Emphasis in Nanoscale Science and Engineering

University of California, Berkeley

Professor Frances Hellman, Chair

This thesis studies the unique properties of Cr and Cr-Al alloys; the first half focuses on Cr while the second half focuses on Cr-Al alloys. Both Cr and Cr-Al alloys have sharp features in their d bands which affect their magnetic properties and ultimately lead to anomalous electrical transport. Although the specifics of the element and the alloy are quite different, they are united by the sensitivity of their magnetic and electronic states to external perturbation. This thesis particularly focuses on the effects of nanoscale structure such as crystal defects, grain boundaries, and short- to medium-range chemical ordering, on both the magnetism and the electronic transport properties of Cr and Cr-Al.

Bulk chromium has an incommensurate spin density wave (ISDW) and has been widely studied as an archetypal band antiferromagnet. The ISDW results in a sinusoidal modulation of the antiferromagnetically aligned moments; this is due to delicate nesting of the Fermi surface which is easily disrupted by perturbation. Thus, the SDW transitions from incommensurate to commensurate (CSDW) or to paramagnetic with small amounts of dopant atoms (Mn or V) or with the application of pressure. These effects have been well studied in bulk Cr.

The 1988 discovery of giant magnetoresistance (GMR) in Fe/Cr multilayers, which was awarded the 2007 Nobel prize in physics, inspired further research on the SDW in Cr, and shifted the focus of that research towards films and multilayers, where variables such as thickness, strain, and disorder are crucial. Until recently, most studies of the SDW in Cr thin films have focused on ultrathin, epitaxial films; however many of the Fe/Cr multilayers studied in the literature are polycrystalline. In fact, the degree of disorder in a multilayer is an important variable, as some research has analyzed the effects of surface roughness on GMR. This thesis aimed to understand the SDW in polycrystalline Cr films such as those commonly used in GMR multilayers, where disorder and stress are the important variables.

Infrared reflectivity was used to measure the characteristic SDW pseudogap energies to distinguish the SDW state of Cr thin films grown under different deposition conditions (e-beam and sputtered at different argon pressures). The fundamental distinguishing properties of the films are stress and disorder, both strongly affected by the deposition conditions. Films with low stress and disorder are ISDW, like bulk Cr. Films with high

tensile stress are CSDW, like Mn-doped Cr. Finally, films with high disorder, determined from the resistivity, have regions of both ISDW and CSDW. Importantly, all of the Cr films measured showed SDW signatures, showing that the SDW is quite robust even in highly disordered thin films. A low temperature magnetic phase diagram was created for Cr films.

The SDW in Cr also leads to anomalous features in the electrical resistivity due to resonant impurity scattering. This occurs when impurities form quasilocalized states within the SDW pseudogap. When the quasilocal states are near the Fermi energy, resonant scattering occurs and causes features such as very high residual resistivity and a resistivity minimum with temperature. This has been studied in bulk samples due to dopant impurities, and theorized to occur for lattice defects such as vacancies as well. However, the defect concentrations in bulk are very low so this was not observed until our measurements on polycrystalline films.

It was shown that Cr thin films show unusual and extremely deposition condition-dependent resistivity due to resonant scattering, such as residual resistivity ranging between 3 and 400 $\mu\Omega$-cm, and significant resistivity minima at low temperature. Several experiments showed that these features are due to defects in the Cr lattice such as grain boundaries and vacancies. When a highly disordered, 400 $\mu\Omega$-cm film with a significant minimum is annealed to 800°C, the resistivity is decreased by $10\times$ and the depth of the minimum is decreased by $50\times$. On the other end of the spectrum, two low resistivity ($< 10\mu\Omega$-cm) samples grown in the same run but on different substrates show small but noticeable different sized resistivity minima (0.01 and 0.003 $\mu\Omega$-cm) because one is polycrystalline and the other epitaxial.

The anomalous resistivity and SDW behavior observed in Cr films led to the study of $Cr_{1-x}Al_x$ alloys. $Cr_{1-x}Al_x$ exhibits semiconducting behavior for $x \sim 0.25$. Initially, researchers studying $Cr_{1-x}Al_x$ suggested that the SDW pseudogap, which eliminates about 30% of the Fermi surface in pure Cr, may eliminate the entire Fermi surface in $Cr_{1-x}Al_x$, leading to a complete gap. However, the SDW gap primarily affects d electrons, while conduction occurs primarily through s electrons, so this suggestion does not explain the observed behavior.

The peak resistivity occurs around $x \sim 0.25$, suggesting a stoichiometric Cr_3Al compound could be responsible for the semiconducting behavior. Such a compound was suggested by a previous electron diffraction study, but the mechanism for affecting the transport behavior was not explained until now. The results of this thesis indicate that the semiconducting behavior in $Cr_{1-x}Al_x$ is due to a combination of a stoichiometric Cr_3Al compound causing a hybridization gap on one part of the Fermi surface with the SDW gap eliminating another part.

The atoms in Cr_3Al are observed to occupy the sites of a bcc lattice, like Cr. Density functional theoretical calculations were performed to compare possible types of chemical ordering and showed that the Cr_3Al structure proposed from electron diffraction, a chemically ordered rhombohedrally distorted phase with ordering along the <111> direction, is the lowest energy of those considered. In addition, the band structure for this structure shows a pseudogap, consistent with the observed transport behavior of Cr_3Al.

Experimental results also support the importance of an ordered phase. Nonequilibrium thin films of $Cr_{1-x}Al_x$ were grown at different substrate temperatures to vary the

properties. Samples grown below 400°C are semiconducting, while samples grown above 400°C are metallic. This is consistent with the proposed 400°C phase boundary for the ordered Cr_3Al structure.

The SDW pseudogap also plays an important role in the semiconducting behavior, but this is difficult to measure experimentally. The Neel temperature of Cr_3Al is about 500°C, at which point the resistivity is already quite metallic. For this reason, two previous studies on the resistivity around the Neel temperature came to different conclusions about the role of the SDW pseudogap on the semiconducting behavior.

To clarify this, neutron diffraction was performed to study the SDW state of $Cr_{1-x}Al_x$ films. Because of the sensitivity of the SDW state to deposition conditions in Cr thin films, and the significant variation in transport properties of $Cr_{1-x}Al_x$ films grown at different temperatures, a change in the magnetic state may be expected to accompany the variation in transport properties in $Cr_{1-x}Al_x$. It was found that both metallic and semiconducting $Cr_{1-x}Al_x$ films had robust antiferromagnetism, with Neel temperatures above the highest measured temperatures ($\sim 600K$).

Theoretical results quite clearly suggest that antiferromagnetism is a necessary condition for the semiconducting behavior. The density of states for antiferromagnetic and nonmagnetic Cr_3Al were calculated and show that the pseudogap is eliminated in the nonmagnetic case. Thus, antiferromagnetism was shown to be a necessary but not sufficient condition for producing the semiconducting behavior in $Cr_{1-x}Al_x$.

It is thus concluded that the semiconducting behavior in Cr_3Al arises from a combination of the antiferromagnetic pseudogap and a rhombohedral-type chemical ordering of the bcc lattice.

To my family: past, present, and future.

Contents

List of Figures

List of Tables

Acknowledgments

Graduate school has been quite a journey, and there are so many people who have contributed, in some small or large way, to that journey.

I must first acknowledge my advisor, Frances Hellman, for providing me with the opportunity to pursue my own research interests and really take charge of my own project. This has been both a pleasure (once I found my feet) and a valuable experience.

I would also like to thank Steve Louie and Yuri Suzuki, for taking the time to serve on both my qualifying exam committee and my thesis committee. Both also contributed to my formal education through their teaching of excellent courses: Solid State Physics and Magnetic Materials.

The Hellman Lab has been my home and family for the past 6 years, and the camaraderie I have found there has been essential to making my way through graduate school. Dave Cooke, Daniel Queen, Mark Wong, Erik Helgren, and Li Zeng transmitted to me the lore of the Lab, with stories of "bottle rockets" and "rat-blasters". Daniel and Dave especially taught me everything I know about microfabrication, and a lot of what I know about working in a lab. Julie Karel has been my partner-in-crime on the e-beam chamber, proof that two brains (and four hands) are better than one (or two). Chloe Baldasseroni, Micol Alemani, Hyeon-Jun Lee, Catherine Bordel, and Cory Antonakos have made the lab a fun place to be, and have helped me in countless other ways.

My collaborators outside the Hellman lab have also been important and a pleasure to work with. Derek Stewart, at Cornell, was a huge help guiding me in my DFT calculations. Alex Gray and Chuck Fadley, at LBNL, motivated the photoemission measurements which turned into a really nice experiment. Thomas Saerbeck and Anton Stampfl, at ANSTO, welcomed me to their beamline and gave me a crash course in neutron scattering. The students and postdocs in the Stacy lab, Ramesh lab, and Suzuki lab here at Berkeley have been extremely helpful whenever I had questions about XRD measurements.

Finally, I want to acknowledge the support I've had in my personal life. Graduate school has challenged me in many ways, not only academically, and forced me to grow and improve in many avenues: self-esteem, communication skills, decision making, and fact-finding. None of this would have been possible without the support of my friends and family.

My friends have been making school cool since 1994. Back then we did math homework together; now we write theses together (sometimes from afar).

My parents have been great supporters of my education, but they never forgot to support love, sleep, and play in equal quantities. When I wavered, they reminded me of my strengths.

My sister helped me develop my competitive spirit. She was a fierce competitor for someone half my size. (And still is! Fortunately we've grown past that now.)

Most important during this time has been Jason. We have made a life together for the past 11 years, and sometimes that life has seemed to revolve around my schoolwork. He has been a great balancer, supporting me in my efforts but keeping me grounded in the other parts of life too. We've had some adventures together but some of my favorites have been the non-adventures - walks, trips to the pool, and eating takeout on the couch.

Finally, I want to acknowledge the new addition we're expecting in our family. He has given me one thing that every graduate student needs at a certain point - a deadline. I can't wait to meet him and start this new chapter of our lives.

Chapter 1

Introduction

Chromium is a unique material in that its magnetic and transport properties show rich, complex physics, but it comes in a simple package: a single element crystallizing in the bcc crystal structure. This has made it an ideal playground for physicists and has led to extensive study and understanding of chromium.[30, 31] At the same time the complexity is enough that there are still open questions being explored currently.[33, 136]

In addition to the rich physics, Cr plays an important part in technological applications. For example, it is used as a coating on STM tips to achieve spin-polarized detection. The antiferromagnetism of Cr yields spin polarized detection without the problematic stray fields of ferromagnetic tips.[74] And it is one of the key ingredients in Fe/Cr multilayers, the first system to show giant magnetoresistance (GMR), for which the Nobel prize was awarded in 2007.[34] This application in particular utilizes the unique magnetic properties of chromium, the spin-density wave (SDW) antiferromagnetism.

Since the Nobel-prize winning discovery in 1988[10], research on Cr has begun to focus less on bulk and more on thin film samples.[104, 93] Thin film growth often yields nonequilibrium crystal structures due to kinetic and surface effects, and this can be exploited to manipulate the structure of materials. Extrinsic effects such as nanosized grains and strain are also common in thin films.

This thesis focuses on the effects of nanoscale structure on the magnetism and transport properties of Cr and Cr-Al alloys. The nanoscale structures considered here are primarily those occurring due to the thin film growth process: the effect of grain boundaries in polycrystalline films, where grain sizes are on the order of 20 nm; the effect of large tensile strains, made possible by these nanoscale grains; the effect of crystal structures occurring in nanodomains separated by anti-phase boundaries. The experimental growth and characterization processes necessary for these experiments are described in Chapter 2.

Chapter 3 probes the magnetism of Cr thin films, which departs markedly from bulk behavior. Bulk chromium is a SDW material and has been widely studied as an archetypal band antiferromagnet. [30] The SDW in bulk Cr is incommensurate (ISDW), meaning that the wavelength is not an integer number of lattice constants. The transition to the paramagnetic state occurs at a Neel temperature (T_N) of 311 K. Small perturbations by dopant atoms, strain, and disorder can change the SDW to commensurate (CSDW), where the wavelength is an integer number of lattice constants, or to the paramagnetic

(a) Spin structure for ISDW (shown: transverse)

(b) Spin structure for CSDW

(c) SDW phase diagram for bulk Cr with dilute (V, Mn) doping
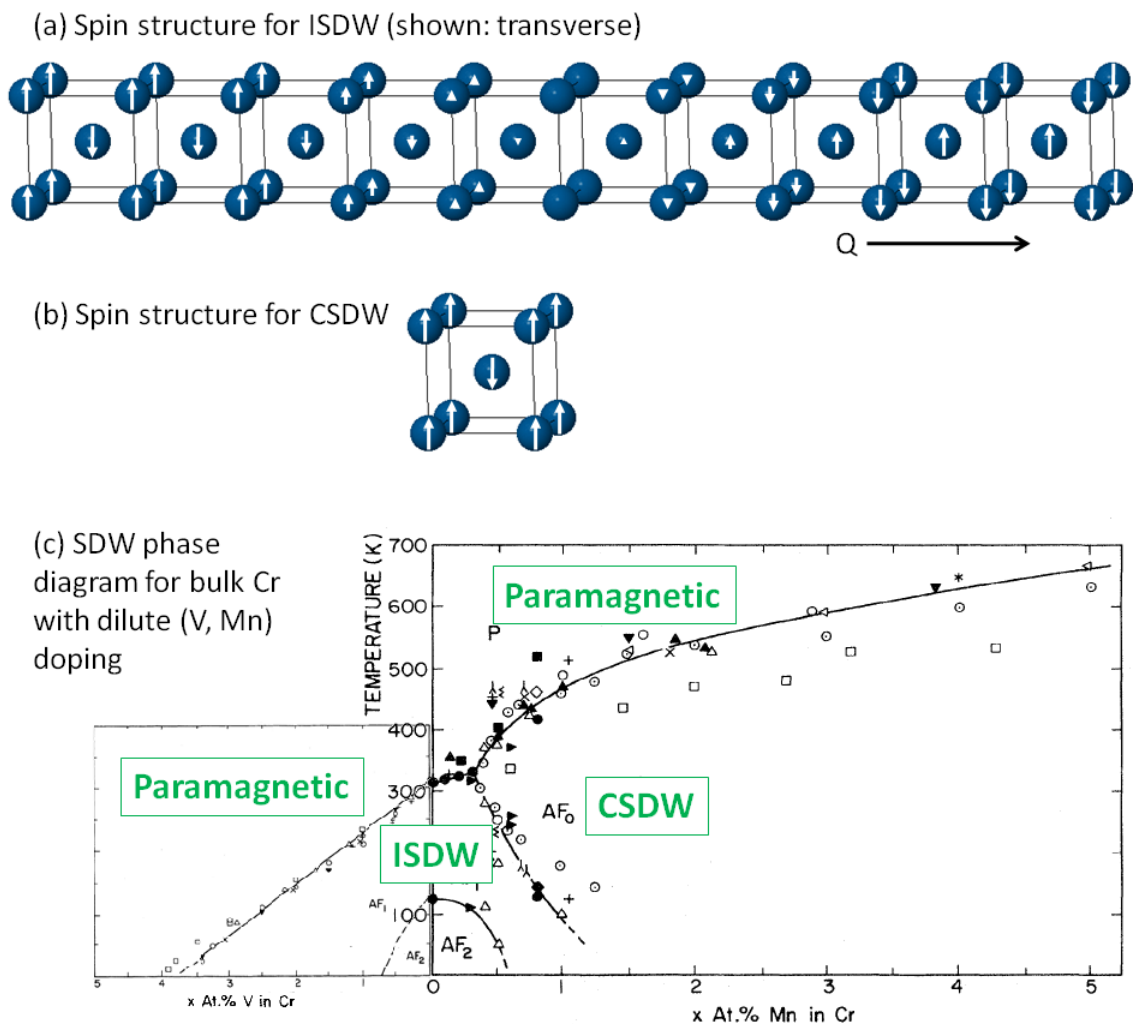
Figure 1.1: Overview of SDW behavior in bulk Cr. (a) Example of spin structure in the ISDW state. (Shown: the transverse or AF1 structure, $S \perp Q$). Here, the SDW wavelength is about 60 Å, the approximate value for bulk Cr at 10 K.[93] (b) Spin structure in CSDW state. (c) SDW phase diagram for bulk Cr with dilute (Mn, V) doping (valence -1, +1). Both the AF1 (ISDW transverse, $S \perp Q$) and AF2 (ISDW longitudinal, $S \parallel Q$) are shown. Phase diagram adapted from E. Fawcett (1988).[30]

state. The spin structures of the ISDW and CSDW are shown in Figure 1.1(a-b).

The classic example of this sensitivity is that adding 0.3-1.0 at. % Mn into bulk Cr introduces a CSDW phase between the low temperature ISDW and high temperature paramagnetic phases; above 1.0 at. % Mn the ISDW phase is entirely replaced by the CSDW. On the other hand, with the addition of V the ISDW remains, but the Neel temperature slowly decreases until 4 at. % V, at which point the resulting material is paramagnetic at all temperatures. The explanation given for this zero temperature quantum phase transition is that the electron concentration is increased with the addition of Mn, while it is decreased with the addition of V (Mn has +1 and V -1 valence compared to Cr). The change in electron concentration disrupts the delicate Fermi surface nesting responsible for the ISDW.[31] The SDW phase diagram of Cr with dilute (Mn, V) doping is shown in Figure 1.1(c)

Pressure and stress have been shown to affect the SDW state of bulk chromium in a similar way to doping.[30] The application of pressure decreases the Neel temperature, much like V doping. Attempts have been made to explain the close comparison between pressure and doping as having the same effect on the Fermi surface. However, this has been shown to be a naive argument.[31] In fact, recent results show that, at very high pressures, a divergence is seen between the effect of hydrostatic pressure and V doping.[33]

Tensile stress may be expected to mimic the effect of Mn doping.[9, 135]. Creating tensile stress in a bulk sample is a difficult experiment, but thin film growth provides an excellent tool for addressing this issue. Thin films often sustain high tensile stress: 1-2 GPa is commonly observed.[58] This is in striking contrast to bulk Cr, which has a ultimate tensile strength of only 300 MPa.[59] This is possible due to the well known effect of grain boundaries on the strength of materials.[77] In addition, thin film growth allows the disorder provided by grain boundaries to be studied. In this way, thin film growth and nanoscale structure opens up regions of phase space not possible in bulk material. Chapter 3 describes the effects of stress and disorder on the SDW, and provides a low temperature SDW phase diagram in the stress-disorder plane.

Chapter 4 studies the effect of disorder on the transport properties of Cr. Like the SDW, the transport poperties of Cr are also sensitive to perturbation, with even dilutely doped samples showing interesting features in the resistivity. These features are described by the theory of resonant impurity scattering. The theory predicts that dopants cause localized impurity states within the "forbidden" SDW gap. When those states exist near the Fermi energy, resonant scattering occurs, leading to high residual resistivity, resistivity minima, and occasionally resistivity maxima at low temperature.[127, 45, 44, 46, 47]

Theoretically, the type of impurity atom is not very important to formation of a localized state, and even defects in pure Cr should lead to resonant impurity scattering.[127] This has never been observed in bulk samples, presumably because the density of defects is very small. However, thin films provide many defects in the form of grain boundaries, point defects, and dislocations. In our study, almost all Cr thin films grown have minima in the resistivity. Some of the films also have anomalously high residual resistivity (ρ_0), up to 400 $\mu\Omega$-cm. Chapter 4 studies the anomalous transport properties seen in Cr thin films in the context of resonant impurity scattering and electron-phonon scattering.

To illustrate how unexpected such a high resistivity is in a metal, Figure 1.2 shows the resistivity of some well-understood materials on a log scale. Typically, metals have

Resistivity (ρ) of materials (μΩ-cm) | dρ/dT | Applications

0.001
0 – Superconductor below T_C
0.0015 μΩ-cm – 99.999% pure Cu at 0 K

Positive dρ/dT   Current-carrying wires

1

4 μΩ-cm – ordered, crystalline CuAu (room temp)

14 μΩ-cm – disordered, crystalline CuAu (room temp)

150 μΩ-cm – typical amorphous metal alloy mean free path ~ inter-atomic distance   dρ/dT ~ 0   Resistors
400 μΩ-cm – most resistive Cr thin film

1000

3600 μΩ-cm – bulk Cr_3Al (0 K)
4000 μΩ-cm – highly doped semiconductor (0 K) Si:P, n = 7 x 10^{18}/cm^3 P   Thermoelectrics

Negative dρ/dT

500,000 μΩ-cm – very close to metal-insulator transition (0 K)
Si:P, n = 3.55 x 10^{18}/cm^3 P

1000000

∞ – True insulator (0 K) Si:P, n < 3.50x 10^{18}/cm^3 Transistors

Figure 1.2: Overview of resistivity of materials. Cu and Cu-Au data from Kittel[65]; typical amorphous metal alloy data from Mooij[88] and Gurvitch[52]; Cr_3Al data from Chakrabarti[18] and Nomerovannaya[91]; Si:P data from Stupp[114]. $d\rho/dT$ is roughly correlated to ρ, is positive for metals and negative for insulators, transitioning through zero around 150 $\mu\Omega$-cm.[88] However, there are some exceptions to this correlation.[6]

very low ρ_0, and $\rho(T)$ which increases with temperature. The addition of impurity atoms increases this resistivity: in the case of a crystalline CuAu alloy with site disorder, $\rho(300K)$ increases from 4 to 14 $\mu\Omega$-cm. Amorphous alloys yield even higher resistivities, as the mean free path (l) is reduced to about the interatomic distance; it has been shown that for a typical amorphous metal alloy, having about 1 e^-/atom, the resistivity reaches a value around 150 $\mu\Omega$-cm. Because l smaller than the interatomic distance is unphysical ($l \not< a$), the resistivity often saturates around this value.[88] A more formal description is that the mean free path cannot be smaller than the de Broglie wavelength of the electron ($l \not< \lambda$), which is an approximately equivalent statement because $\lambda = \lambda_F \sim a$ in a metal with one electron per atom. This is called the Ioffe-Regel limit.[52]

In the simple Drude model, the resistivity of a material is given by[65]:

$$\rho = m/ne^2\tau \tag{1.1}$$

Thus, the primary variables leading to the resistivity are the scattering time τ (related to l) and the number of carriers n. Typically, materials with $\rho \ll 150\mu\Omega$-cm and positive $d\rho/dT$ are constrained by τ while materials with $\rho \gg 150\mu\Omega$-cm and negative $d\rho/dT$ are constrained by n. The high resistivity seen in Cr films is primarily due to resonant scattering (τ) and extrinsic geometry effects, which are described in detail in Chapter 4.

Anomalies in the resistivity of Cr, such as resistivity minima and sometimes even maxima at low temperatures, occur for many different dilute dopants.[31, 46] A particularly anomalous example is the case of Al doping in Cr. Crystalline Cr with about 5 at. % Al has a resistivity around 100 $\mu\Omega$-cm. The resistivity reaches a maximum of 3600 $\mu\Omega$-cm at about 25 at. % Al (Cr_3Al stoichiometry), with a negative $d\rho/dT$.[18, 91] Such high resistivity, well above what is seen even in amorphous alloys, is most likely due to a decrease in n rather than τ. This behavior is characteristic of a highly doped or small gap semiconductor, or semimetal. Such materials are not used in the traditional semiconductor applications such as transistors, but are of increasing interest in new fields such as thermoelectric power generation.[110, 111]

The transport behavior of Cr-Al alloys is intuitively surprising, as alloys and compounds made of metallic elements are generally expected to be metallic. Indeed most are; however, some intermetallic compounds are semiconducting or semimetallic, for example $RuAl_2$ or Fe_2VAl.[129] In theory, any compound with an even number of valence electrons in the primitive unit cell can be semiconducting because the electrons can completely fill the valence band. However, transition metals usually have several overlapping bands at the Fermi energy (E_F), so even in compounds with an even number of electrons typically several bands are partially filled, resulting in a metal. For an intermetallic compound to be semiconducting, hybridization must shift the bands in a fortuitous way, leaving a gap at E_F.

For the Cr_3Al stoichiometry, there are a total of 21 valence electrons in the formula unit. Even if there is a gap in the band structure, how is it possible to completely fill a band with an odd number of valence electrons? This question is one reason why the semiconducting behavior in Cr-Al has never been explained. The high resistivity seen in Cr-Al alloys is unexpected and intriguing, and is the subject of Chapters 5, 6 and 7.

Chapter 5 discusses hard x-ray photoemission measurements of a $Cr_{0.80}Al_{0.20}$ thin film. The measurements confirm a band gap or pseudogap, showing that the valence band

edge is about 95 meV below E_F in this film. The next chapters explain the reason for such a gap.

Chapter 6 investigates the possibility that an ordered Cr_3Al structure is responsible for the unexpected properties. This has been suggested in literature, as one study showed extra spots in electron diffraction. The spots were attributed to an ordered structure occuring in nano-sized domains separated by anti-phase boundaries, contained within large bcc crystallites.[24] A mechanism for how the ordered structure would lead to the observed transport properties had not been suggested previously, but is discussed in this work.

In order to study this, we again made use of the unique properties of thin film growth in order to manipulate the structure. Growth at different substrate temperatures stabilized nonequilibrium structures so that we could compare their properties. Density functional theory (DFT) calculations were also used to calculate the DOS and band structure of different possible structures. We find that a rhombohedrally distorted, chemically ordered structure has the lowest ground state energy by DFT. This structure also shows a pseudogap in the DOS and a semimetallic-type band structure, made possible by the fact that there are 42 valence electrons in this structure's primitive cell (Cr_6Al_2). A semimetal has slightly overlapping bands at E_F, so the calculated band structure does not show a full gap. DFT often underestimates the gap in semiconductors, and can show overlapping bands where a true gap exists.[84] On the other hand, experimentally, semimetals can have similar transport behavior to degenerate semiconductors[133], and the properties of Cr_3Al are more consistent with a semimetal than a semiconductor (such as a nonzero electronic specific heat coefficient[95] and non-activated resistivity behavior[18, 91]). Whether perfectly ordered Cr_3Al would be a true semiconductor or a semimetal is still unclear.

Chapter 7 discusses the role of magnetism in the transport properties of Cr-Al alloys. In Cr, the SDW leads to a pseudogap at E_F, with a significantly decreased DOS(E_F) compared to paramagnetic Cr.[30] It has been suggested that in Cr-Al, the antiferromagnetic pseudogap is enhanced compared to Cr, leading to a fully semiconducting or semimetallic band structure.[18] Cr-Al (with greater than 3 at. % Al) has CSDW structure and a high Neel temperature (up to 900 K) based on neutron scattering.[62] Experimentally, it is difficult to measure the role of the antiferromagnetism in the semiconducting behavior. Two different studies have attempted to determine this by measuring the resistivity below and above the Neel temperature, with different conclusions.[18, 105] Because the Neel temperature is so high, and the transport behavior indicative of a narrow gap semiconductor or semimetal, the resistivity is already practically metallic near the Neel temperature. In addition, some feature in the resistivity is expected to occur due to the magnetic transition (as is seen in Cr[30]); this can be difficult to separate from a semiconducting-to-metal transition. Thus, the results are difficult to interpret.

In Chapter 7, we use DFT calculations to theoretically determine the role of magnetism in the anomalous transport behavior. Experimentally, we also verify the CSDW antiferromagnetism in Cr-Al thin films grown under different conditions, such that one is semiconducting and one is metallic. Ultimately, we show that the magnetism is a necessary but not sufficient condition for creation of a gap in Cr-Al.

This thesis addresses important materials, Cr and Cr-Al alloys, and how they

are affected by structure at the nanoscale level. The results have implications for both applications and basic physics. For example, on the applications side, we show how the magnetism in Cr changes with thin film deposition conditions, which could affect how GMR multilayers are made in the future. On the basic physics side, we show how the anomalous electronic transport behavior in Cr-Al alloys can be explained by nanodomains of chemical ordering, as well as antiferromagnetism, resulting in a pseudogap in the band structure, something that was never previously understood. We hope these developments make an impact on both the magnetism industry and basic solid state physics research communities.

Chapter 2

Growth and characterization of Cr and Cr-Al alloy thin films

Physical vapor deposition (PVD) of thin film samples can lead to nonequilibrium structures which we can manipulate to study the connection between structure and function. Cr and Cr-Al thin films were deposited under various conditions in order to control the thin film structure. This chapter describes the deposition techniques and post-deposition characterization. For Chapters 3 and 4, the Cr thin film samples were mostly grown by sputtering (Section 2.1.3), except for certain films which were grown by e-beam evaporation (Section 2.1.2). For Chapters 5, 6 and 7, the Cr-Al samples were grown by co-deposition of Cr from an e-beam source and Al from an effusion cell (Section 2.1.1).

2.1 Deposition methods

All PVD deposition methods are qualitatively similar. The source materials (in this case, Cr and Al) are inside a vacuum chamber and are slowly vaporized such that there is a flux of source material onto the substrates and surrounding area. The substrates are held on a sample plate. Often, the temperature of the sample plate is controlled by a heater. Figure 2.1 shows an example PVD system. Although systems vary, the sources are often at the bottom for practical reasons (for example so that melted source material does not fall out during evaporation), and the substrates are often at the top, facing down, so that the surfaces will not be contaminated by falling dust or flakes during deposition. In sputtering systems, the orientation is more flexible because the material is not melted.

2.1.1 Thermal evaporation

Thermal evaporation is the simplest method of PVD. The source material is placed in a W boat and a current is run through the boat. Joule heating causes the boat to heat up, and the source material is therefore heated until evaporation begins.

A cleaner way to perform thermal evaporation is to use an effusion cell. An effusion cell contains the source material within a ceramic crucible, with W filaments around the
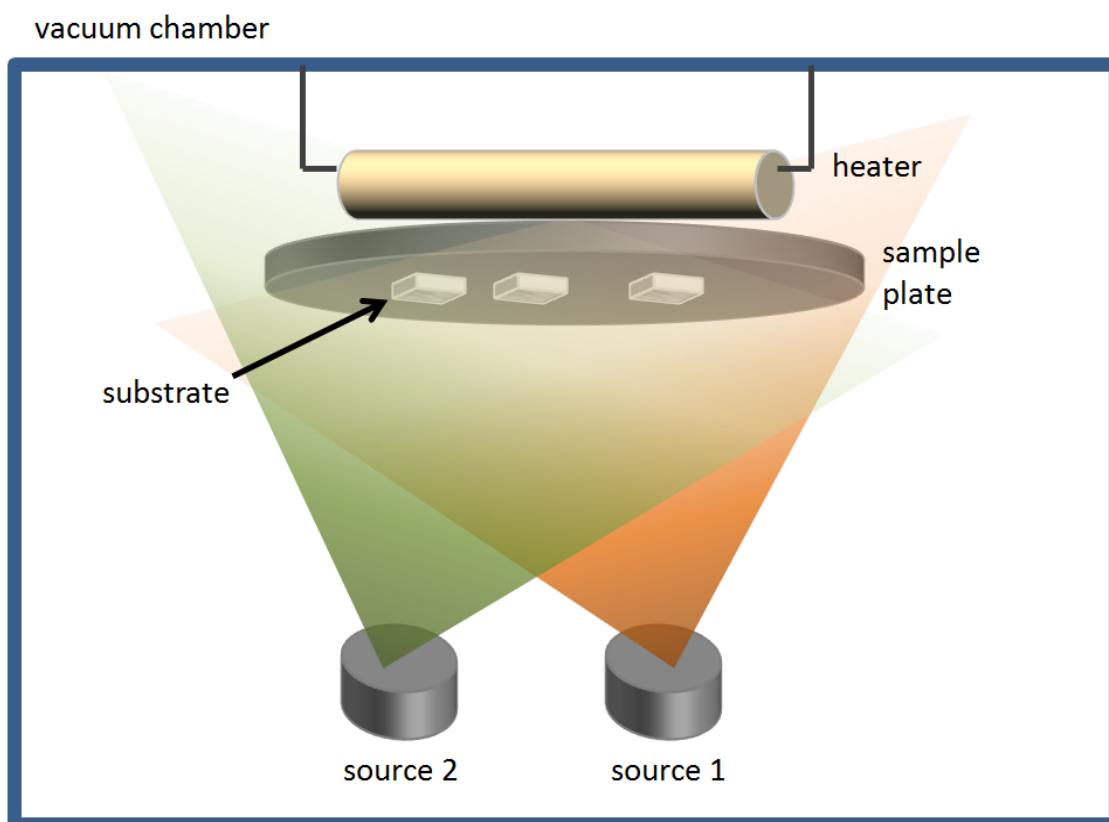
Figure 2.1: Diagram of typical PVD setup.

crucible to provide heating. This leads to a more uniform and controlled temperature and therefore evaporation rate.

Cr sublimes, which means it does not melt before reaching an appreciable evaporation rate. For this reason, rather than placing pieces in a W boat, which would lead to extremely nonuniform heating of the Cr, often a Cr-coated W wire is used for evaporation. In addition, for evaporation of Cr from an effusion cell, a special cell is required to reach a high enough temperature for evaporation to occur.[118, 20]

Al can be deposited fairly well from an effusion cell due to its low evaporation temperature. We evaporated Al from a standard single-filament effusion cell at a temperature of 1140 °C. Special considerations must be taken for Al, as molten Al has a tendency to "creep" outside the crucible, potentially shorting the W heater. A special effusion cell is recommended for Al in order to avoid this problem: a "cold lip" cell or dual-filament cell, where the top of the crucible can be kept at a lower temperature than the bottom, can solve this problem.[118] However, we were able to manage with a standard cell. By keeping the temperature under 1140 °C, we were able to avoid any "creep" outside the crucible. The only problem is the accumulation of molten Al "droplets" near the lip of the crucible, which can lead to slight variations in evaporation rate, which must be watched for.

2.1.2   Electron beam deposition

E-beam deposition uses a focused electron beam aimed at the source material to heat it, rather than Joule heating through a filament. The source material is placed in a Cu crucible, which is placed in a water-cooled hearth. This method ensures that the hottest part is always the source material, which decreases the chance of contamination problems.

E-beam is a good method to evaporate Cr. In order to ensure a constant rate, a large, flat piece of Cr is used for a source material (99.95% pure, 1" diameter disk, 0.25" thickness - Kurt Lesker Part no. EJTCRXX351A4).[20] Because Cr does not melt, it is important to make sure that the Cr makes good contact to the cooled Cu crucible. This can be done by lining the crucible with smaller Cr pieces, as shown in Figure 2.2. A custom-made Cr target can be made in the shape of the crucible, but it is more expensive and must be made to fit exactly or the heat flow will not be sufficient.

Figure 2.2(c) shows a Cr target after significant deposition has occurred. A hole has been created in the center of the electron beam location. Ideally, a flat source surface should be maintained to avoid beaming effects; typically the largest beam spot size is used to keep the surface as flat as possible. The beam can also be moved across the surface, however this changes the tooling factor of the crystal monitor used to track the deposition rate. Once a hole is seen in the target, it should be replaced with a fresh source.

The growth rate is controlled by the power supplied to the electron gun. To achieve the most stable rate, the gun power must be ramped slowly and then controlled by a PID feedback loop linked to the crystal rate monitor through a Sycon STC-2000A deposition rate controller. For Cr, a stable rate can achieved with the parameters shown in Table 2.1.

Parameter	Value
P	40
I	2.0
D	1.0
Soak 1 power level	19%
Power ramp 1 time	4:00 minutes
Power soak 1 time	2:00 minutes
Soak 2 power level	24%
Power ramp 2 time	12:00 minutes
Power soak 2 time	99:59 minutes (perform growth)
Max power limit	28%
Average power during deposition	$\sim 26\%$

Table 2.1: Deposition rate controller parameters for achieving a stable rate for Cr sublimation
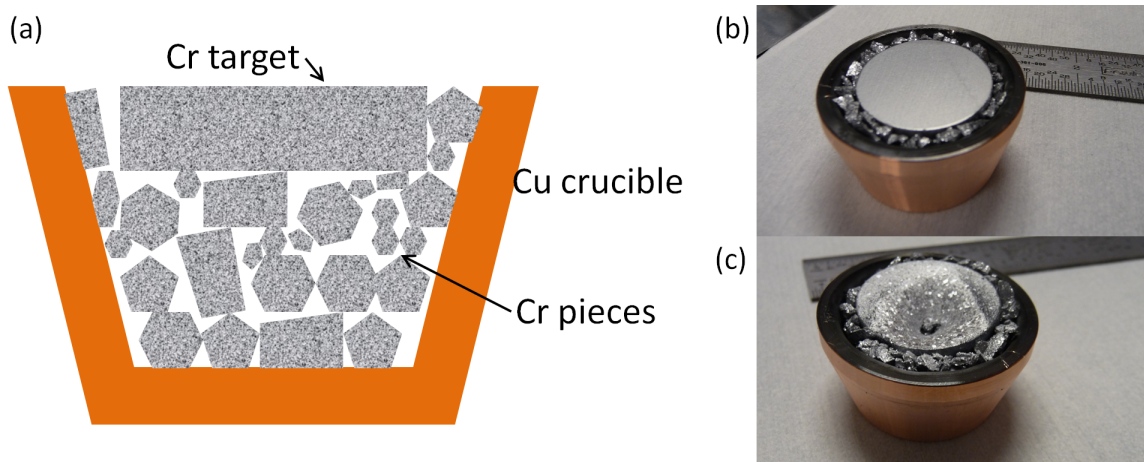
Figure 2.2: Cr source for e-beam evaporation. (a) Diagram: cross-sectional view of source. (b) Photo of fresh Cr source. (c) Photo of spent Cr source. Notice the hole in the middle where the center of the beam hit.

2.1.3 Sputtering deposition

Sputtering deposition refers to a PVD process where the source material is vaporized, not by heating, but by gaseous ions (in this case Ar^+) impinging on the surface at high energy and "sputtering" source atoms into a vapor. Modern sputtering systems typically use "magnetron sputtering", where the ionized gas is confined to the source material area by a magnetic field. This prevents contamination of the sample due to sputtered material from the chamber walls, etc.

Unlike thermal or e-beam deposition, sputtering deposition can vary greatly depending on the sputtering gas pressure, adding an extra variable to tune the growth process. This is due to thermalization of atoms as they pass through the gas on their way to the substrate; thus both the pressure and the source-substrate distance are important. Sputtering gas pressure cannot be compared between chambers on a one-to-one basis, the pressures cited here are for the Hellman Lab's AJA 5-gun sputtering system with an approximate source-substrate distance of 20cm.

Typical parameters used for sputtering Cr in this system are: base pressure $<$ 5×10^{-8} Torr, DC gun power 150W (range 75-250W), sputtering gas (Ar) pressure 0.75-8 mTorr.

To achieve the most bulk-like Cr films, the recipe used was: substrate temperature $350°$C, Ar pressure 0.75 mTorr. The resulting films have a low residual resistivity (see Chapter 4) and have the incommensurate SDW (see Chapter 3).[15, 14]

For growth on room temperature substrates, growth at the lowest possible Ar pressure results in the lowest residual resistivity (see Chapter 4) and no measurable oxygen contamination (see Section 2.3.2.3). The lowest achievable Ar pressure in our chamber was 0.75 mTorr; pressures lower than this cannot sustain a plasma at the source. Films grown at 0.75 mTorr on room temperature substrates show the commensurate SDW rather than the incommensurate SDW seen in bulk Cr and in films grown at $350°$C (see Chapter 3).[15, 14]

2.1.4 Post-deposition annealing

Often, samples are annealed after deposition. This can be done in situ, by heating the sample plate within the deposition chamber directly after deposition, or ex situ, by using an annealing furnace. We have an RTA (rapid thermal annealer) furnace for post-deposition annealing, which flows gas through a tube while heating quickly with quartz lamps. The annealing temperature can be reached within a few minutes, held steady for about a minute, and then cooled rapidly. An example RTA temperature profile is shown in Figure 2.3. The RTA is especially useful for annealing samples which need to be cooled rapidly (quenched), for example to lock in a high-temperature phase. However the RTA can be used for standard annealing as well.
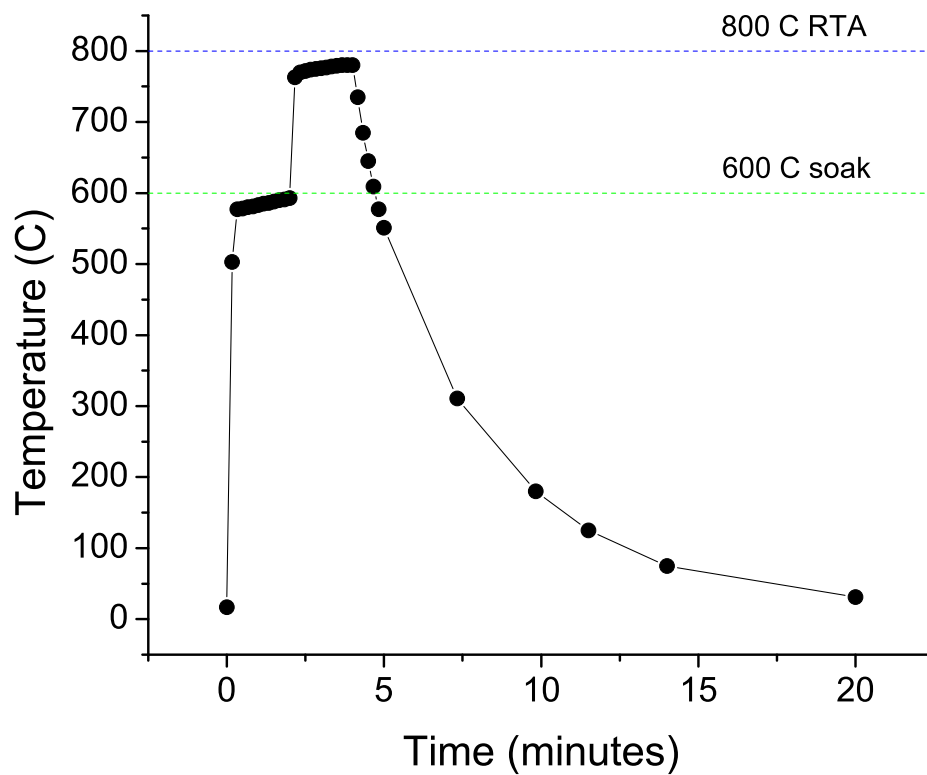
Figure 2.3: Temperature vs. time profile for a typical rapid thermal anneal (RTA). This run soaks at 600 °C for 2 minutes with a rapid thermal anneal for another 2 minutes at 800 °C. This routine was used for the sputtered, polycrystalline Cr films discussed in Chapter 4. Data shown is for sample S06-114.

Condition	Temperature (°C)
T_m	1857[20]
$T_s = 0.3T_m$	366
$T_s = 0.5T_m$	792

Table 2.2: Approximate temperatures relevant to zone model

2.2 Structural characterization

2.2.1 Polycrystalline Cr films

The microstructure of polycrystalline thin films has been well studied and depends on how much energy and time the atoms forming the film have to find equilibrium. The primary factor is the thermal energy of the atoms (substrate temperature), and for sputtered films, the additional energy transferred to the surface by the sputtering process. The growth rate is also important, as surface atoms will be buried before finding equilibrium if the rate is too high.

2.2.1.1 Grain structure

Except for very high temperature or epitaxial growth, PVD-grown thin films typically have a columnar structure with a grain size that increases with film thickness. Even amorphous films can have a columnar structure, with columns of higher density material separated by smaller regions of low density.[137]

A good estimate of the mobility of atoms on the surface is the reduced temperature, or ratio of the substrate temperature to the material's melting temperature: T_s/T_m (in Kelvin). For $T_s/T_m \lesssim 0.3$, surface atoms have little mobility and form columnar grains of poor crystalline quality, separated by voids and grain boundaries a few nm wide. For $T_s/T_m \gtrsim 0.3$, surface atoms have more mobility and transition to a structure that is still columnar but with much narrower grain boundaries. For $T_s/T_m \gtrsim 0.5$, the grains are larger and can be non-columnar. These growth modes are sometimes described as "zones".[109] The melting point of Cr, and the relevant values of T_s/T_m are shown in Table 2.2.

For sputtered films, additional energy can be transferred to the surface by high energy species, either Ar atoms or atoms of the source material. This can lead to very different film microstructures for different Ar pressures, even when the substrate is kept at room temperature. Paradoxically, although the added energy comes largely from Ar atoms bombarding the film surface, this effect is actually larger at low Ar pressures. This is because although more Ar is available to bombard the surface at high pressures, each individual atom has lower energy as it has gone through more collisions (thermalized) on its way to the substrate.

This effect has been well studied, with room temperature grown Cr films used as a test. It was shown that at high Ar pressures, the low energy, voided structure is found, while at low energies, tighter grain boundaries are found.[56, 121, 57, 58, 55] This also has an important impact on stress, which will be discussed in Section 2.2.1.2.

2.2.1.1.1 Electron microscopy of microstructure Electron microscopy is a technique for imaging the microstructure of thin films, and is also applied to bulk materials and biological samples. It has much higher resolution than optical microscopy, which is limited by the wavelength of visible light ($\sim 1\mu$m). Scanning electron microscopes (SEMs) typically operate with 10-20 keV electrons (which have a wavelength of ~ 0.1Å), while transmission electron microscopes (TEMs) typically operate with ~ 200 keV electrons (wavelength ~ 0.01Å). In practice, the resolution of an SEM ranges between 1-20nm, while TEMs often have atomic resolution.[132, 131]

SEMs image using backscattered electrons, thus showing the topography of surfaces. TEMs use transmitted electrons, thus they require that the samples are thin enough to be electron-transparent ($\lesssim 100$nm). This, and other technical issues, means that SEMs are significantly more user-friendly than TEMs, which require significant sample preparation before use. The SEM images shown in this thesis were taken by myself using a Hitachi S-4300SE/N at Lawrence Berkeley National Lab. TEM was done with collaborators, including D. J. Smith at Arizona State University.

Figure 2.4 shows SEM images of the surfaces of some polycrystalline Cr films as well as TEM cross-sectional images of two films. (a-b) show two e-beam deposited Cr films, grown at 300 °C. Both show elongated, acicular grain structure. The grains shown in (a) are oriented in three primary directions due to the Al_2O_3 substrate, this is discussed further in Section 2.2.2.1.2. (c-d) show two sputtered Cr films, grown at room temperature under different sputtering pressures. The film grown at higher pressure (8 mTorr) shows more surface roughness than the film grown at lower pressure. (e) shows an 8 mTorr sputtered film (similar to the one seen in (d)) after annealing at 800 °C. Although the grain size remains the same, the grain shape and structure has changed significantly. It looks as though grains have coalesced, leaving larger voids rather than many small voids. (f-g) shows TEM cross-sectional images of a low and a high pressure sputtered Cr film. The cross-sectional view confirms the columnar structure and puts a scale to the surface roughness which from SEM can only be qualitatively discussed. The 0.75 mTorr sample shows a very flat surface, while the 8 mTorr sample shows a very rough surface, with roughness on the order of 20 nm. In addition, the 8 mTorr sample shows some amorphous material between grains and a growth mode of increasing grain size with thickness.

An interesting point to note is that all films shown in Figure 2.4 have similar grain sizes of about 20 nm. However, the details of grain structure vary, and thus the properties. The effects of this are seen in Chapters 3 and 4.

2.2.1.1.2 X-ray diffraction (XRD) X-ray diffraction (XRD) is a useful tool, used as early as 1912, for studying the atomic arrangements of crystals. The Bragg condition states that constructive interference of x-rays occurs when:[65]

$$2d \; \text{sin}\theta = n\lambda \qquad (2.1)$$

The most basic XRD experiment consists of scanning the angle θ and finding "peaks" at certain values where the condition is met. This is called a $\theta - 2\theta$ scan. An example of a $\theta - 2\theta$ scan is shown in Figure 2.5. For polycrystalline films, theoretically peaks should be seen at many angles θ corresponding to different atomic planes, as is seen for the 1 μm thick

SEM: 250nm

TEM: 100nm

(a) e-beam Cr/Al$_2$O$_3$

(b) e-beam Cr/a-SiO$_2$/Si

(f) sputtered 0.75 mTorr

(c) sputtered 0.75 mTorr

(d) sputtered 8 mTorr

(e) 8 mTorr ann. 800 ºC
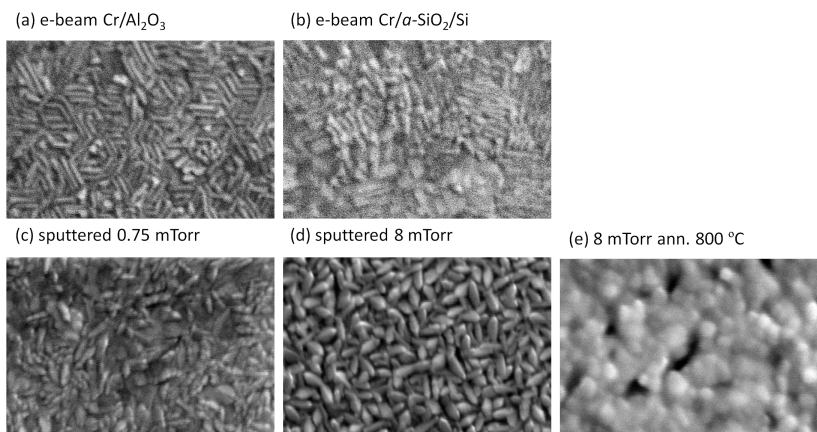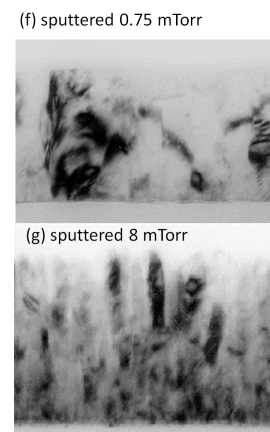
(g) sputtered 8 mTorr

Figure 2.4: (a-e) SEM top-down images of samples: (a) e-beam deposited Cr/Al$_2$O$_3$, (b) e-beam deposited Cr/a-SiO$_2$/Si, (c) sputtered 0.75 mTorr, (d) sputtered 8 mTorr, (e) sputtered 8 mTorr annealed at 800 °C (f-g) Cross-sectional TEM images: (f) sputtered 0.75 mTorr (100nm film), (g) sputtered 8 mTorr (130nm film).

film shown in Figure 2.5. In practice, for thinner films and short counting times, only the most intense peak(s) are usually seen.

A powder diffractometer is most appropriate for measuring polycrystalline films. The polycrystalline films in this thesis were measured in a Siemens D5000 automated powder x-Ray diffractometer with a diffracted beam graphite monochromator and scintillation counter, found in the Stacy group lab in the UC-Berkeley Chemistry department.[51] This diffractometer has enough intensity to detect the weak signal from polycrystalline films, unlike the Panalytical diffractometer discussed in Section 2.2.2.

One drawback to the powder diffractometer is that the monochromator is not as efficient (as a tradeoff for higher intensity). As you can see in Figure 2.5, some $\lambda/2$ (second harmonic) contamination of the x-rays can lead to extraneous peaks (in the figure, an Si peak at 33°). The intensity of the $\lambda/2$ contamination is at the 0.1% level, so that it is only seen for the very strong substrate peaks. The other drawback of using a powder diffractometer is that the geometry is limited to $\theta - 2\theta$ scans. For polycrystalline films, this is not a problem as there should not be a strong directional dependence of the XRD peaks.

XRD patterns for known materials can be found by searching the Powder Diffraction Files (PDF), compiled by the International Centre for Diffraction Data.[37] For unknown materials, the peaks must be calculated using Equation 2.1. Cr in the usual bcc structure has well-known diffraction peaks. A few publications in the literature report thin films of Cr with alternative, non-bcc crystal structure, such as the δ phase or A-15 phase.[64, 63, 25] No evidence of these or other non-bcc phases was seen in our measurements, with all films showing at least one of the known bcc peaks (generally the intense (011) peak).
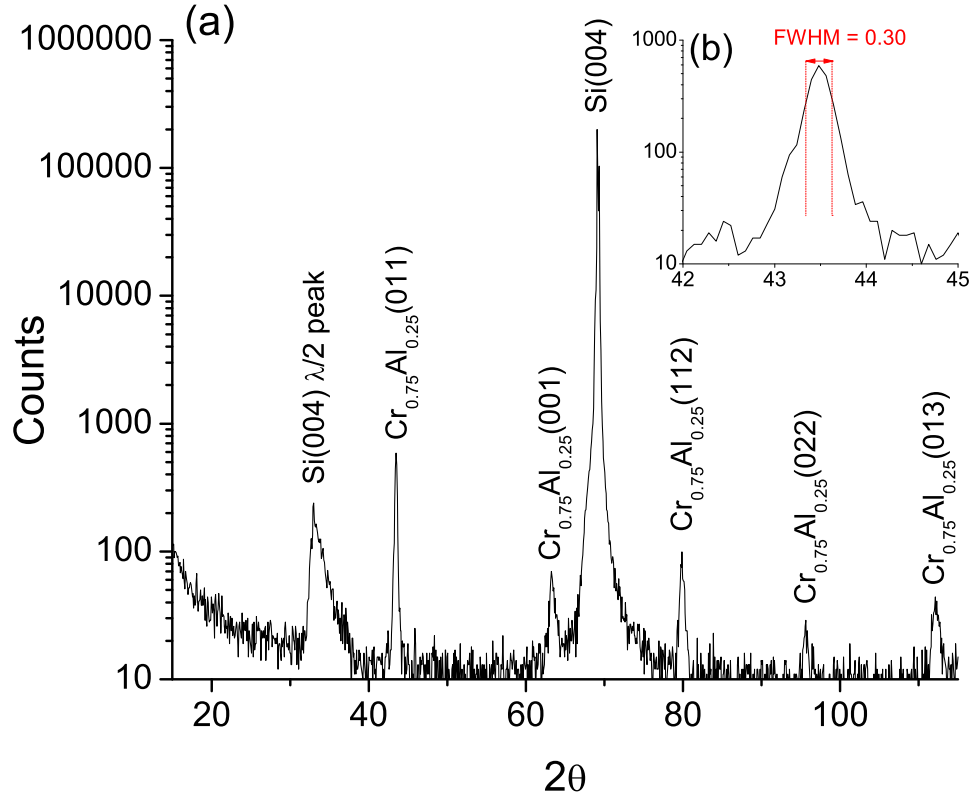
Figure 2.5: XRD $\theta - 2\theta$ scan of a 1 μm thick polycrystalline $Cr_{0.75}Al_{0.25}$ film, grown on a-SiO$_2$/Si. The Si(002) peak is normally disallowed, but is seen here due to $\lambda/2$ contamination of the XRD source. Data shown is for sample T11-007.

X-ray diffraction can also be used to calculate the correlation length, or grain size. For a typical $\theta - 2\theta$ scan in the normal geometry (normal to the film plane), this grain size refers to the vertical (out-of-plane) correlation length, which may differ from the in-plane grain size as seen in SEM. The correlation length is related to the full-width at half maximum (FWHM) of the diffraction peak by the Scherrer formula:[109]

$$b = 0.9\lambda/\Delta(2\theta)\cos\theta \tag{2.2}$$

From the data shown in Figure 2.5, the FWHM of the Cr-Al(011) peak is 0.30°. Subtracting quadratically the 0.15° instrument broadening, the out-of-plane correlation length is found to be 361Å. This is much smaller than the 1 μm film thickness, suggesting that there are many defects or grain boundaries interrupting the long-range order throughout the thickness of the film.

Sample	Density (g/cm^3)
Bulk Cr	7.2[20]
Sputtered Cr, 0.75 mTorr, 350°C substrate	7.6 ± 0.7
Sputtered Cr, 0.75 mTorr, room temp substrate	7.4 ± 0.2
Sputtered Cr, 8 mTorr, room temp substrate	5.5 ± 0.5

Table 2.3: Density of sputtered Cr thin films

2.2.1.1.3 Density Because of the varying microstructures found in polycrystalline films, film density may vary from bulk as well. The film density can be measured directly by measuring the mass and volume of the films. The substrate mass was measured with a microbalance before film deposition, and then again after deposition. Film volume was measured with a ruler (length and width for film area) and KLA-Tencor Alpha-Step IQ profilometer (thickness). Density from 5-10 samples of each type was calculated and averaged, with an error defined by the standard deviation.

Results of the density measurements are found in Table 2.3. Films grown at low pressure have bulk density (within error), regardless of substrate temperature. Films grown at 8 mTorr have reduced density. Because the films grown at 8 mTorr are confirmed by XRD to have the usual Cr bcc crystal structure, the reduced density is due primarily to microstructural effects rather than atomic-scale effects.

One reason for reduced density can be seen in the cross-sectional TEM image in Figure 2.4(g). The rough surface, consisting of "peaks" and "valleys", has a small lateral length scale ($\sim$ 20nm), less than the width of a profilometer tip. Thus, the "thickness" measured by the profilometer is the height of the peaks rather than the average thickness. The valleys between peaks are empty, contributing to the reduced density measurement. Other reasons for reduced density could be voids between grains, which are more obvious in the annealed 8 mTorr sample shown in Figure 2.4(e). Additionally, amorphous material between grains could lead to reduced density.

2.2.1.2 Stress and strain

As mentioned in Chapter 1, thin films often sustain high tensile stress: 1-2 GPa is commonly observed.[58] This is in striking contrast to bulk Cr, which has a yield strength under tension of only 300 MPa.[59] This is possible due to the well known effect of grain boundaries on the strength of materials.[77]

Stress occurs in polycrystalline films for two reasons: "intrinsic" stress caused by the growth method, and stress due to differences in thermal expansion between the sample and susbtrate. The latter reason is only relevant for films grown at an elevated temperature, while most of the polycrystalline films discussed here were grown at room temeprature.

The intrinsic stress is strongly dependent on microstructure (Section 2.2.1.1). Many thin films naturally grow with a columnar microstructure, which leads to the formation of tensile stress between grains. This is certainly the case for e-beam deposited Cr films.[115] Deviations from this microstructure and stress is caused by a difference in the

energy of surface atoms as the film grows.

For sputtered films, the stress in films grown at room temperature is strongly dependent on the sputtering gas pressure in a nonmonatonic way. For very low sputtering pressures, incident atoms impinge on the sample surface with a very high energy, pushing atoms into the sample and resulting in compressive stress. For moderate sputtering pressures, columnar grains form, which causes tensile stress from connected grains at the grain boundaries. For high sputtering pressures, the tensile strain begins to decrease as the columnar grains start to become isolated from each other and voids form between grains.[58]

The sputtering gas pressures associated with these stress regimes depends on the atomic mass of the material and of the sputtering gas. This is because the energy of atoms incident on the surface depends on the energy lost due to collisions between the source and substrate. The energy loss can be estimated with a simple billiard ball model.

2.2.1.2.1   Wafer curvature   We measured the stress in our sputtered films using a Tencor FLX-2320 stress measurement system. This system requires that a film is deposited onto a 4" wafer. The curvature of the wafer is measured before and after film deposition using a laser. The stress of the film is then calculated by the change in curvature of the wafer and the material properties of the wafer. The results are shown in Figure 2.6.

Because Cr is a relatively light element, in our system we only observe the mid and high pressure stress regimes, as the low pressure regime cannot be reached while sustaining a plasma at the source. This is consistent with previous studies of Cr.[58]

2.2.2   Epitaxial films

The epitaxial films in this research were grown by e-beam deposition of Cr, with Al from an effusion cell when necessary. This is due to the lower background pressure of the e-beam chamber which can be important for epitaxy. However, Cr films have been grown epitaxially by sputtering as well, both in the Hellman Lab's AJA sputtering chamber and by other researchers.[38, 40]

2.2.2.1   Epitaxial relations

2.2.2.1.1   MgO(001) substrate   Cr(001)/MgO(001) epitaxy is well known[38, 40] and robust, so MgO(001) was the primary substrate used for epitaxy in this research. Epitaxy on MgO(001) was observed in our Cr and $Cr_{1-x}Al_x$ films grown at substrate temperatures between 200 and 600°C (typically 300°C), at growth rates of about 0.5 Å/s, with a base pressure below 5×10^{-8} Torr.

The epitaxial relation is shown visually in Figure 2.7. The lattice constant of MgO is 4.21Å, while that of Cr is 2.88Å. The difference is about a factor of $\sqrt{2}$, so that the Cr cubic unit cell grows 45° rotated on the cubic MgO unit cell. The epitaxial mismatch is 3.4% for Cr on MgO. However, for $Cr_{1-x}Al_x$, the addition of Al increases the lattice constant and improves the mismatch. For $x = 0.25$, the mismatch is decreased to 0.9%. Epitaxial growth of $Cr_{1-x}Al_x(001)/MgO(001)$ was found for $x = 0 - 0.37$.

Evidence for epitaxy is shown in Figure 2.8. In (a), a typical XRD $\theta - 2\theta$ scan is shown, showing only strong MgO(002) and Cr-Al(002) diffraction peaks. This is in contrast
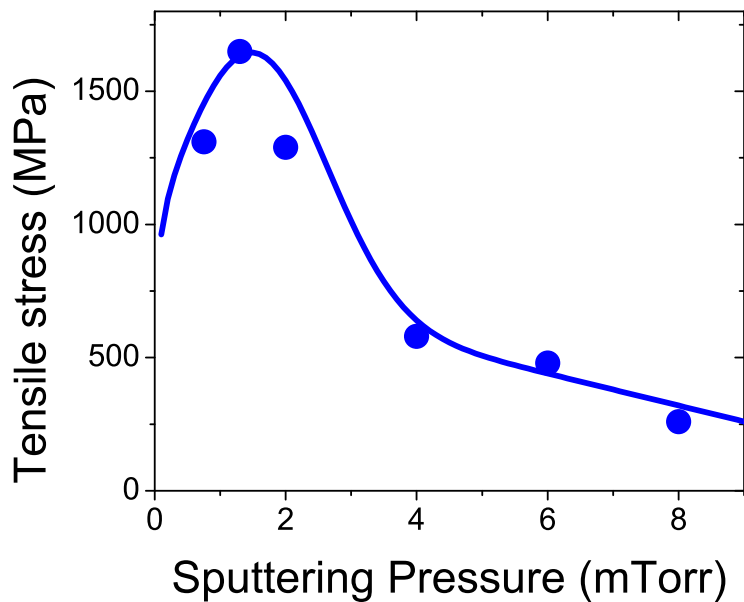
Figure 2.6: Stress, as measured by the wafer curvature method, vs. sputtering pressure for Cr films.
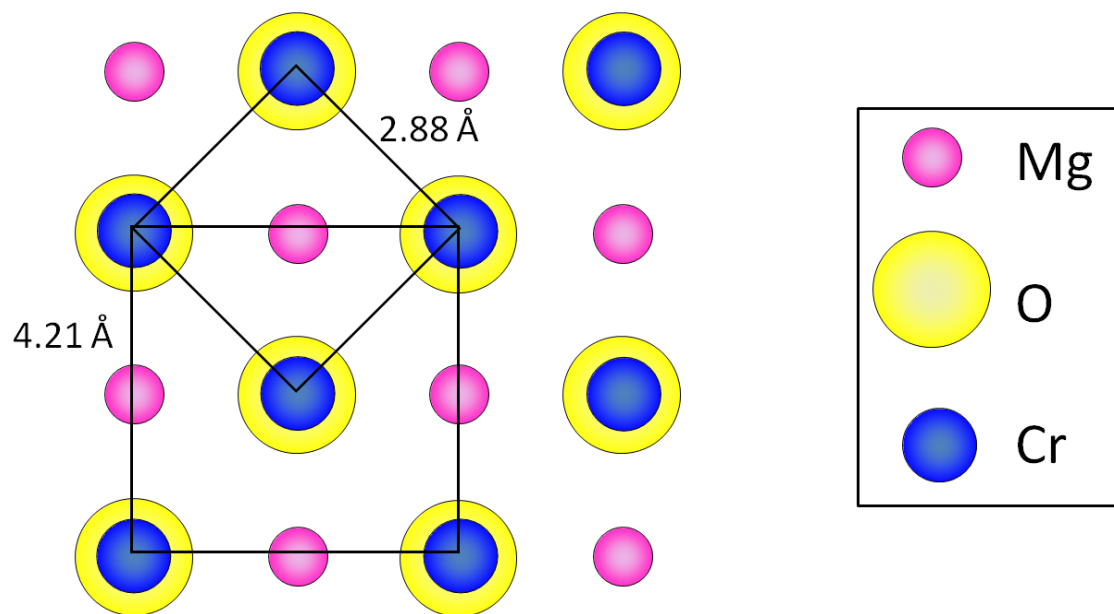
Figure 2.7: Epitaxial relation of Cr(001) growth on MgO(001).
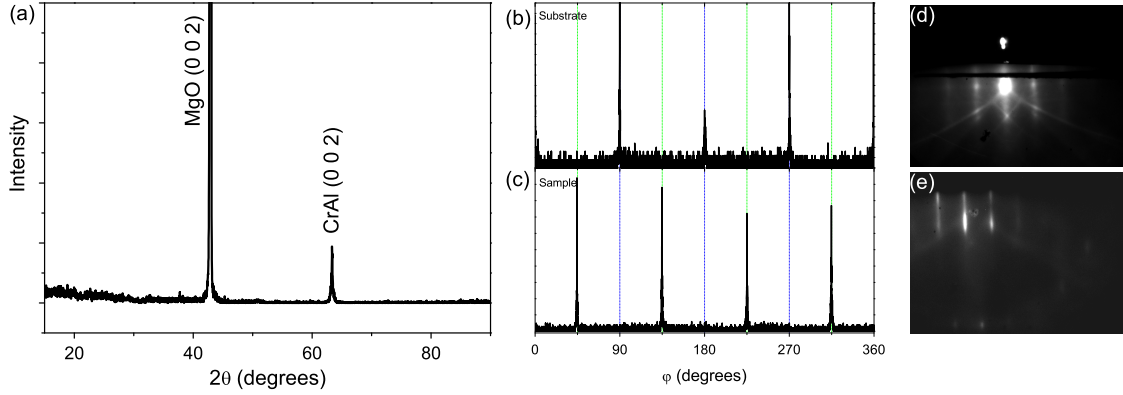
Figure 2.8: Evidence of Cr-Al(001) epitaxy on MgO(001). (a-c) XRD of a 400Å thick $Cr_{0.78}Al_{0.22}$ film on MgO(001). (a) $\theta - 2\theta$ scan showing only Cr (001) orientation out of plane. (b-c) ϕ (azimuthal) scans of (b) the MgO substrate {011} peaks measured at 45° from normal and (c) Cr sample {011} peaks measured at 45° from normal (d-e) RHEED patterns for (d) bare MgO(001) substrate and (e) 500Å $Cr_{0.80}Al_{0.20}$(001)/MgO(001). Data shown is for samples (a-c) T08-068 and (d-e) T09-049.

to the multiple weak diffraction peaks shown in a polycrystalline film (Figure 2.5). However, the presence of a single diffraction peak does not definitively mean epitaxy.

To confirm epitaxy, the powder diffractometer used to measure polycrystalline films is not appropriate, and instead we use a diffractometer optimized for thin films. We used the Panalytical XPert MRD Pro 4-circle diffractometer, found in the Ramesh lab in the UC-Berkeley Materials Science and Engineering department. This diffractometer has a more discriminating monochromator, explaining why no $\lambda/2$ MgO(002) peak is seen in Figure 2.8(a). In addition, the 4-circle diffractometer is capable of reaching more combinations of sample, beam, and detector angles.

Figure 2.8(b) shows a ϕ (azimuthal) scan from 0-360° around an axis 45° tilted from the sample normal, with the angle 2θ fixed at the MgO011 peak angle. This shows the four-fold symmetry of the MgO single-crystal substrate, as expected.

Figure 2.8(c) shows the same scan performed with the angle 2θ fixed at the Cr(011) peak. This plot also shows four-fold symmetry, confirming that the lattice symmetry of the Cr sample is bound to that of the MgO substrate, i.e. the film is epitaxial. A polycrystalline film with no preferred orientation would show no peaks in a ϕ scan.

The $\theta - 2\theta$ scan and ϕ scans shown in Figure 2.8(a-c) allow us to write an epitaxial relation for Cr(001) growth on MgO(001).

$$
\begin{aligned}
Cr(001) \quad &\| \quad MgO(001) \\
Cr[110] \quad &\| \quad MgO[010]
\end{aligned}
\tag{2.3}
$$

Figure 2.8(d-e) shows reflection high energy electron diffraction (RHEED) patterns
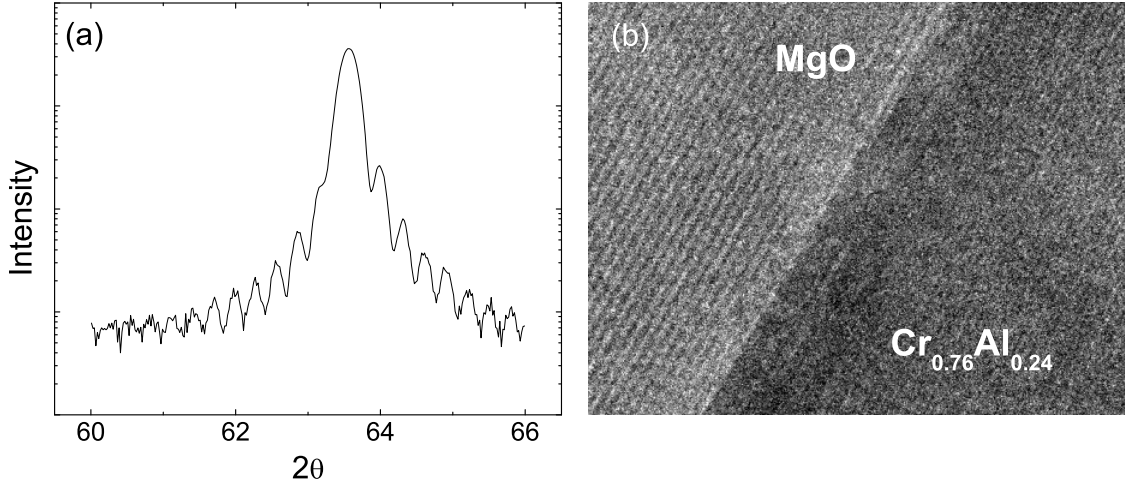
Figure 2.9: (a) Thickness oscillations in an XRD $\theta - 2\theta$ scan seen in a $Cr_{0.76}Al_{0.24}(001)/$ MgO(001) film grown at 400°C. The peak positions correspond to a thickness of 355Å, while the profilometer gives a thickness of 356 ± 21Å. Data shown is for sample T09-088. (b) Cross-sectional TEM image of a $Cr_{0.76}Al_{0.24}(001)/$ MgO(001) interface for film grown at 300°C. Image shown for sample T09-086.

from a Cr(001)/MgO(001) growth. (d) shows the bare substrate, while (e) shows the Cr film on the substrate, after deposition but before exposure to air. A "streaky" pattern, like the one seen here, implies 2-dimensional, layer-by-layer epitaxial growth.[60]

Further evidence of high quality epitaxial growth is shown in Figure 2.9. Part (a) shows an XRD $\theta - 2\theta$ scan, around the $Cr_{0.76}Al_{0.24}$ (002) diffraction peak. The oscillatory background on top of the lattice (002) peak corresponds to Bragg diffraction from a 355Åfeature: the film thickness. Bragg diffraction from the film is dependent on smooth interfaces, so this is strong evidence of a smooth film.

Figure 2.9(b) shows a high-resolution TEM image of the interface between a $Cr_{0.76}Al_{0.24}(001)$ film and the MgO(001) substrate. One-dimensional lattice fringes are seen in the film plane, and indicate a single-crystal film and smooth interface. Lattice fringes in the out-of-plane direction are not seen due to a slight tilt of the sample.

2.2.2.1.2 Al$_2$O$_3$(0001) (c-plane) substrate Cr(011)/Al$_2$O$_3$(0001) epitaxy has been reported in the literature a few times[128, 124], but it is not well-known and has some additional complications compared to Cr(001)/MgO(001) epitaxy. We found Cr(011)/Al$_2$O$_3$(0001) to be robust, but addition of Al destroyed the epitaxy for $Cr_{1-x}Al_x$ for $x \gtrsim 0.05$. Thus Cr(011)/Al$_2$O$_3$(0001) played a smaller role in the research presented here.

Cr(011)/Al$_2$O$_3$(0001) epitaxy is reported in the literature to occur with two possible in-plane orientation relationships: OR-I and OR-II.[128, 124]

$$
\begin{aligned}
\text{OR-I}: \quad & \text{Cr}(011) && \parallel && \text{Al}_2\text{O}_3(0001) \\
& \text{Cr}[100] && \parallel && \text{Al}_2\text{O}_3[01\bar{1}0] \\
& \text{Cr}[0\bar{1}1] && \parallel && \text{Al}_2\text{O}_3[2\bar{1}\bar{1}0] \\
\text{OR-II}: \quad & \text{Cr}(011) && \parallel && \text{Al}_2\text{O}_3(0001) \\
& \text{Cr}[1\bar{1}1] && \parallel && \text{Al}_2\text{O}_3[10\bar{1}0] \\
& \text{Cr}[\bar{2}1\bar{1}] && \parallel && \text{Al}_2\text{O}_3[1\bar{2}10]
\end{aligned}
\tag{2.4}
$$

These epitaxial relations are shown graphically in Figure 2.10. Because Al_2O_3 has hexagonal symmetry while Cr has cubic symmetry, there are actually three different in-plane orientations which satisfy OR-I. OR-II is similar to OR-I, but rotated $5.26°$ to the right or left of OR-II. Thus, six possible in-plane orientations exist which satisfy OR-II.

Figure 2.11 shows evidence of $Cr(011)/Al_2O_3(0001)$ epitaxy in our films. Part (a) shows a $\theta - 2\theta$ scan showing only Cr (011) and (022) peaks out-of-plane. Parts (b-c) show ϕ scans of the sample and substrate, similar to those shown for $Cr(001)/MgO(001)$ in Figure 2.8(b-c). Figure 2.11(b) shows a ϕ scan of the $Al_2O_3\{1102\}$ peaks, showing the six-fold symmetry of the Al_2O_3 single-crystal substrate. Figure 2.11(c) shows a ϕ scan of the Cr $\{001\}$ peaks, also showing six-fold symmetry. How can six-fold symmetry be seen in a cubic Cr lattice? Theoretically, a ϕ scan of the $45°$ off-axis $\{001\}$ peak in a single crystal $Cr(011)$ oriented film should yield two peaks. However, because there are three different possible orientations satisfying OR-I, we see a total of six peaks. Additionally, the six orientations which satisfy OR-II are only $5.26°$ away from OR-I on either side, so that the peaks cannot be distinguished, but rather contributes to an overall broadening of the peaks seen in Figure 2.11(c).

The different orientations of OR-I and OR-II occur in different grains, so that a more appropriate description of these films is polycrystalline films with strong $Cr(011)$ texture induced by epitaxy on $Al_2O_3(0001)$. An SEM image of one of these films is shown in Figure 2.12(a). The image shows the polycrystalline nature of the films, and also interestingly shows some three-fold symmetry in the orientation of the grains, which are acicular and elongated along three directions. The orientation of the SEM image in regards to the XRD ϕ scans is shown in part (b). Using the stereographic projection of the cubic (011) orientation, shown in (c), along with the XRD results from Figure 2.11, it can be shown that the measured $\{001\}$ peaks at $45°$ from normal, and therefore the $<110>$ directions in-plane, occur at angles $\phi \sim 0, 60, 120, 180, 240, 300$. Meanwhile, the elongation of the acicular grains occurs at angles $\phi \sim 30, 90, 150, 210, 270, 330$. This shows that the grain elongation occurs along the $<001>$ directions, with grain boundaries occuring at the $\{110\}$ planes. This is consistent with $\{110\}$, as the close-packed planes, the low energy planes in the bcc structure.[134]

The RHEED patterns shown in Figure 2.11(d-e) show a spotted pattern for the $Cr(011)$ film rather than the streaky pattern shown for $Cr(001)/MgO(001)$. A spotted pattern indicates three-dimensional growth rather than layer-by-layer growth, consistent with the polycrystalline nature of the $Cr(011)/Al_2O_3(0001)$ films.
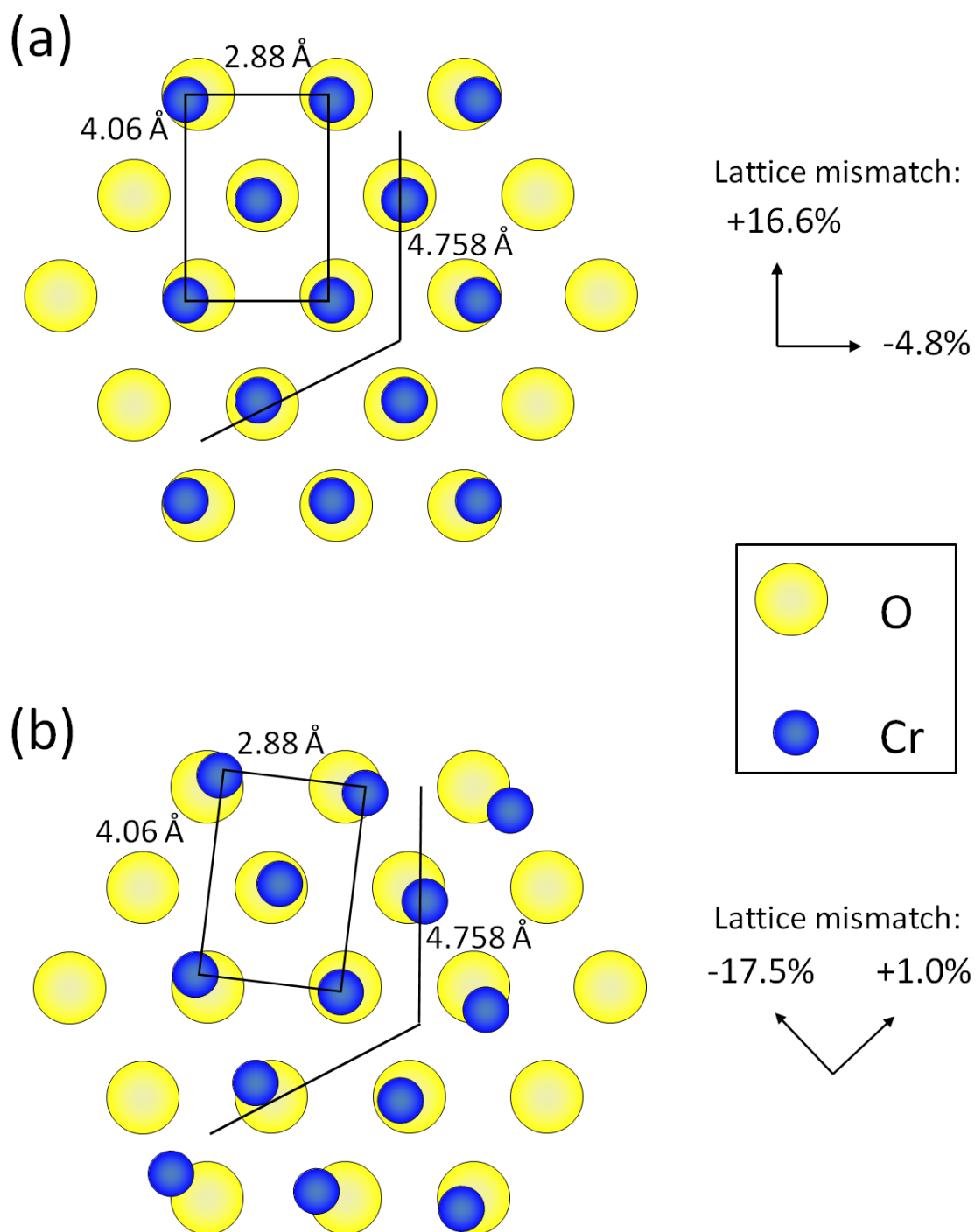
Figure 2.10: Epitaxial relations of Cr(011) growth on $Al_2O_3(0001)$ for (a) OR-I and (b) OR-II.
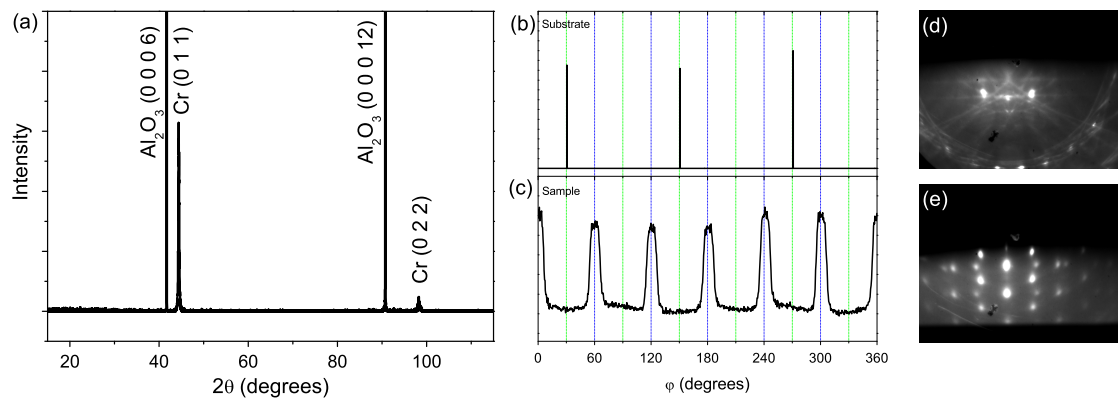
Figure 2.11: XRD of a 2000Å Cr film on $Al_2O_3(0001)$. (a) $\theta - 2\theta$ scan showing only Cr (011) orientation out of plane. (b-c) ϕ (azimuthal) scans of (b) the Al_2O_3 substrate $\{1102\}$ peaks measured at $52.583°$ from normal and (c) Cr sample $\{001\}$ peaks measured at $45°$ from normal. (d-e) RHEED patterns for (d) bare $Al_2O_3(0001)$ substrate and (e) 1000Å $Cr(011)/Al_2O_3(0001)$. Data shown is for samples (a-c) T08-084 and (d-e) T08-047.
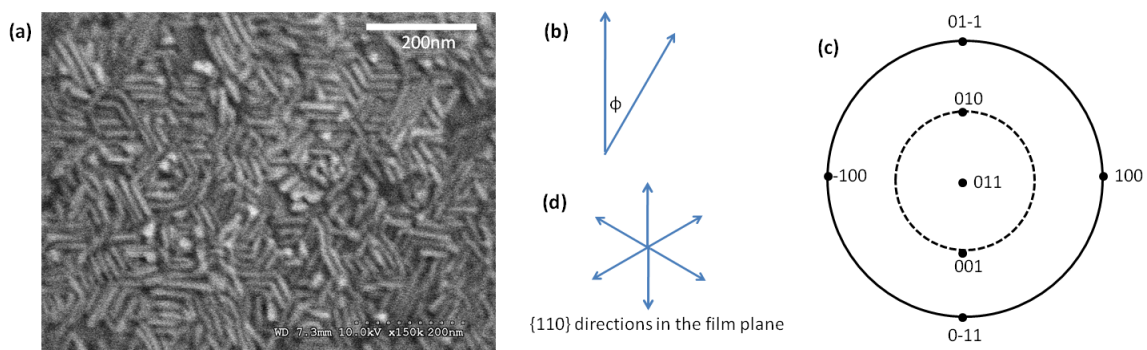
Figure 2.12: (a) Stereographic projection of cubic Cr(011), adapted from Ref. [41]. (b) Definition of angle ϕ referenced to Figure 2.11. (c) Inferred from (a-b) and Figure 2.11, $\{011\}$ directions in the film plane. (d) SEM image of a 2000Å Cr film on $Al_2O_3(0001)$ (T08-084) showing grain elongation along the $\{001\}$ directions with grain boundaries at $\{011\}$ planes.
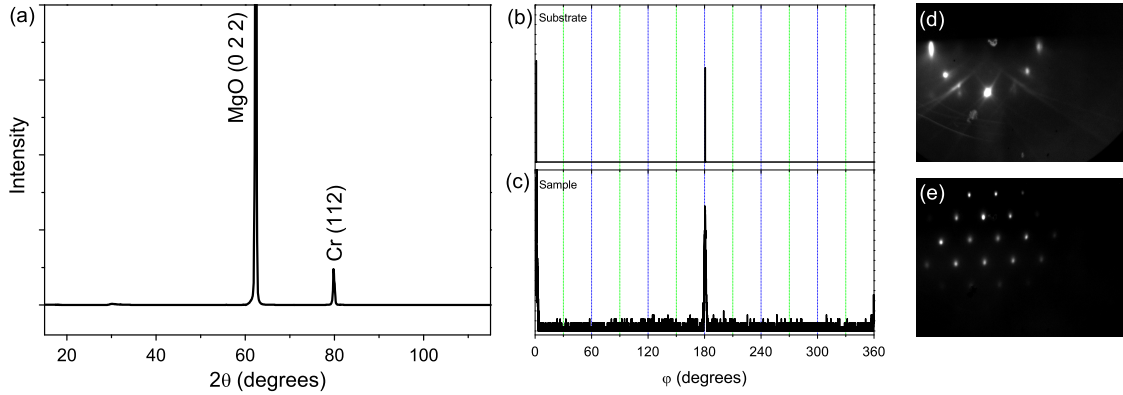
Figure 2.13: XRD of a 2000Å Cr$_{0.80}$Al$_{0.20}$ film on MgO(011). (a) $\theta - 2\theta$ scan showing only Cr (211) orientation out of plane. (b-c) ϕ (azimuthal) scans of (b) the MgO substrate {001} peaks measured at 45° from normal and (c) Cr$_{0.80}$Al$_{0.20}$ sample {001} peaks measured at 35.26° from normal. (d-e) RHEED patterns for (d) bare MgO(011) substrate and (e) 2000Å Cr(211)/MgO(011). Data shown is for sample T09-048.

2.2.2.1.3   MgO(011) substrate   Another known epitaxial relation for Cr is Cr(112)/MgO(011).[39] We found this epitaxy to be less reliable than that of Cr(001)/MgO(001). This may be due to increased sensitivity of the MgO (011) surface to contaminants such as H$_2$O vapor. MgO is known to absorb H$_2$O and should be shipped with dessicator material and kept in a dessicator cabinet until use. Substrates should also never be exposed to H$_2$O during cleaning. Upon leaving MgO(001) and MgO(011) substrates outside of a dessicator cabinet for 5 days, it was found that the RHEED pattern of the bare MgO(011) substrate was significantly altered, while that of MgO(001) showed no noticeable change.

The stated epitaxial relation for Cr(112)/MgO(011) is:[39]

$$\begin{aligned}
\text{Cr}(112) \quad &|| \quad \text{MgO}(011) \\
\text{Cr}[10\bar{1}] \quad &|| \quad \text{MgO}[100]
\end{aligned} \tag{2.5}$$

Figure 2.13 shows the evidence of epitaxy for Cr(112)/MgO(011). Part (a) shows the XRD $\theta - 2\theta$ scan, with only Cr(112) orientation out-of-plane. (b-c) show the ϕ scans of sample and substrate. In this case, it shows two-fold symmetry of both the MgO(011) substrate and Cr(112) film. Finally, (d-c) shows the RHEED pattern of the substrate and film. Again, the Cr(112) shows a spotted pattern indicative of three-dimensional growth. In this case, we do not expect polycrystalline growth due to the strict two-fold symmetry seen in the XRD ϕ scans. Instead, this could indicate faceting of the surface.

2.2.2.1.4   NaCl substrate   Epitaxial growth of Cr and Cr$_{1-x}$Al$_x$ on NaCl would be beneficial because NaCl is soluble in H$_2$O. Thus, epitaxial films grown on NaCl can be soaked in H$_2$O in order to remove them from the substrate and have a freestanding film for

measurement in a TEM. This eliminates the need for complicated TEM sample preparation procedures, especially considering that substrates such as MgO and Al_2O_3 are brittle and often break during preparation for TEM. The NaCl growth surface must be freshly cleaved before growth so the surface does not absorb H_2O vapor. In this way, the substrates are similar to MgO but even more reactive. We purchased 1cm × 1cm cubes of NaCl and cleaved (001) surfaces in air, then transferred the substrates to vacuum for growth as soon as possible.[116]

NaCl has a lattice constant 5.64Å, or about twice that of Cr (2.88Å). Thus, epitaxy can reasonably be expected. One article suggests that Cr does grow epitaxially on NaCl with a single orientation relationship OR-A (Relation 2.6), however the evidence is scant.[98] Another article suggested some epitaxy with two different possible orientation relationships OR-A and OR-B.[107]

$$
\begin{array}{cccc}
\text{OR-A} & \text{Cr(001)} & || & \text{NaCl(001)} \\
 & \text{Cr[010]} & || & \text{NaCl[010]} \\
\text{OR-B} & \text{Cr(001)} & || & \text{NaCl(001)} \\
 & \text{Cr[010]} & || & \text{NaCl[110]}
\end{array}
\tag{2.6}
$$

We attempted Cr/NaCl epitaxy by growing at three different temperatures: 200, 300, and 400°C. The XRD $\theta - 2\theta$ results are shown in Figure 2.14(a). All films showed a Cr(011) peak, contrary to both orientation relationships suggested in Relation 2.6. The film grown at 400°C also appeared semi-transparent, suggesting a reaction between the NaCl substrate and the Cr film. This is most likely due to the formation of a chromium chloride.[98, 101] The films grown at 200 and 300°C showed both Cr(011) and Cr(002) peaks in XRD, strongly suggesting polycrystallinity.

The film grown at 200°C showed the strongest Cr(002) peak and a decreased magnitude of Cr(011), possibly indicating that epitaxy occurred in some portion of the film but polycrystallinity occurred elsewhere. The RHEED image in Figure 2.14(b) is consistent with this, showing some diffuse spots which could indicate epitaxial regions as well as circular arcs around the beam, which indicate a random orientation of polycrystalline grains.

Dissolution of the NaCl substrate in H_2O did not result in a cohesive Cr film being released but rather many small particles of Cr. These would be nontrivial to attach to a TEM grid. The quality of epitaxy was not at all comparable to that of samples grown on MgO(001), so the NaCl substrates were no longer pursued.

2.2.2.2 Stress and strain

Like polycrystalline films, epitaxial films also typically have some degree of stress. In epitaxial films, the stress is often related to the lattice mismatch between the sample and substrate. This stress typically relaxes through creation of dislocations in the film, and the degree of relaxation is dependent on the film thickness. Although the exact mechanisms for stress relaxation vary, a simple model gives a relationship between the lattice mismatch (f) and the critical thickness for relaxation (h_c):[109]
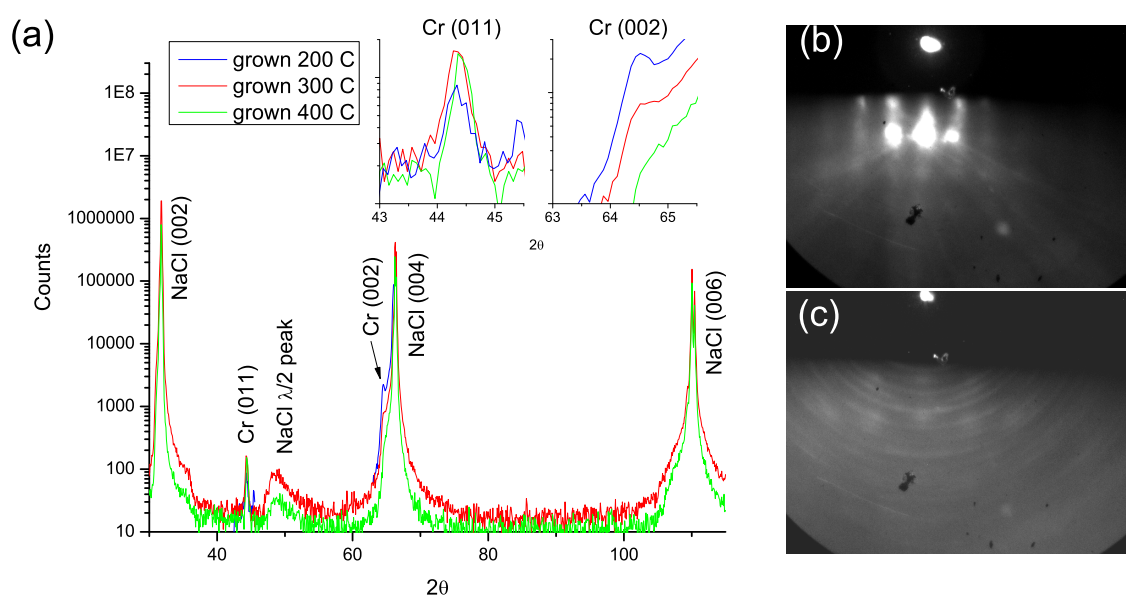
Figure 2.14: (a) XRD $\theta - 2\theta$ scans of 400Å Cr films on NaCl(001) showing both Cr (001) and (011) orientation out of plane. (b) RHEED pattern from freshly cleaved NaCl(001) substrate. (c) RHEED pattern from 400Å Cr grown on NaCl(001) at 200°. Data shown is from samples T09-010 (200°C), T09-001 (300°C), T09-008 (400°C).
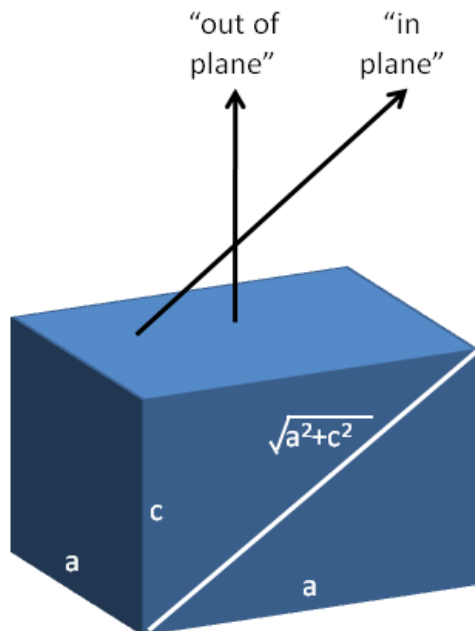
Figure 2.15: Diagram of biaxially stressed cubic unit cell.

$$f = \frac{b}{h_c} \frac{1}{8\pi(1+\nu)} \ln \frac{4h_c}{b} \tag{2.7}$$

Here, b is the magnitude of the Burger's vector of the primary type of dislocation causing relaxation, and ν is Poisson's ratio (0.22 for Cr).[59] Assuming b is equal to the lattice constant, for Cr(001)/MgO(001), with a lattice mismatch of 3.4%, the critical thickness is about 6Å. For $Cr_{0.75}Al_{0.25}$(001)/MgO(001), with a lattice mismatch of 0.9%, the critical thickness is about 44Å. Because all of the films measured here are 400Å or thicker, we assume that strain due to epitaxial lattice mismatch is negligible.

However, stress can still occur, for example due to the difference in thermal expansion between the sample and substrate or imperfect relaxation of stress due to lattice mismatch.

Although the wafer curvature method of measuring film stress (Section 2.2.1.2.1) can theoretically be applied to either polycrystalline or epitaxial films, for our films it was not practical to do so. The 4" wafers necessary for the measurement would be very costly for an MgO substrate, and in any case the e-beam deposition system we used does not fit a 4" sample on the sample plate.

2.2.2.2.1 X-ray diffraction Instead, the strain in our epitaxial films were measured with XRD. Because all unit cells in the film are aligned, XRD can be used to measure both an out of plane and in plane lattice constant by performing a $\theta-2\theta$ scan around the appropriate diffraction points. In the case of Cr(001)/MgO(001) and $Cr_{1-x}Al_x$(001)/MgO(001), we

measure the "out of plane" lattice constant c (002 peak) and the "in plane" lattice constant $\sqrt{c^2 + a^2}$ (022 peak).

The strain (ϵ) is defined as:

$$
\begin{aligned}
\epsilon_x &= (a - a_{relaxed})/a_{relaxed} \\
\epsilon_y &= (a - a_{relaxed})/a_{relaxed} \\
\epsilon_z &= (c - a_{relaxed})/a_{relaxed}
\end{aligned}
\tag{2.8}
$$

Here, $a_{relaxed}$ refers to the relaxed lattice constant (the lattice constant in the unstrained state). Because the relaxed lattice constant is not known exactly except in the case of pure Cr, to calculate the strain we need to first estimate $a_{relaxed}$ using Poisson's ratio. We assumed $\nu = 0.22$, the value for pure Cr,[59] because ν for Cr-Al alloys has not been reported. For biaxial stress, the relations between stress (σ) and strain are the following:

$$
\begin{aligned}
\epsilon_x &= (1/E)(\sigma_x - \nu(\sigma_y + \sigma_z)) \\
\epsilon_y &= (1/E)(\sigma_y - \nu(\sigma_z + \sigma_x)) \\
\epsilon_z &= (1/E)(\sigma_z - \nu(\sigma_x + \sigma_y))
\end{aligned}
$$

For stress due to thin film growth,

$$
\begin{aligned}
\sigma_x &= \sigma_y \\
\sigma_z &= 0
\end{aligned}
\tag{2.9}
$$

Simplifying,

$$
\begin{aligned}
\epsilon_{x,y} &= ((1 - \nu)/E)\sigma_{x,y} \\
\epsilon_z &= (-2\nu/E)\sigma_{x,y}
\end{aligned}
$$

Thus, the ratio of strain out of plane to strain in plane is:

$$
-\epsilon_z/\epsilon_{x,y} = 2\nu/(1 - \nu)
$$

Here, E is the Young's modulus. Thus, the lattice constants c and a can be measured from XRD. From c, a, and Equations 2.8 and 2.9, $a_{relaxed}$ can be solved for. Finally, the strain is calculated from Equation 2.8. The accuracy of this method depends on many things: the assumed Poisson's ratio, the degree to which strain in the plane results in curvature out of the plane, and the alignment of the x-ray diffractometer.

It was found that, for Cr and $Cr_{1-x}Al_x(001)/MgO(001)$ films grown by e-beam, the strain is tensile for all temperature ranges, presumably due to a larger coefficient of thermal expansion for MgO than Cr or $Cr_{1-x}Al_x$.[27, 30] Table 2.4 shows an example strain calculation:

An alternative method for assessing strain in epitaxial films using a four-circle XRD is the reciprocal lattice map (RSM). This method typically measures a 2D map of neighboring sample and substrate XRD peaks in reciprocal space, to determine whether the in-plane q vectors are the same or different (relaxed).[35] RSM was not used for our films, due to the $\sim \sqrt{2}$ difference in lattice constant between the MgO substrate and the film. This causes there to be no neighboring sample and substrate diffraction peaks except in the direction of the film plane, which is not accessible.

	$2\theta(°)$	Lattice constant
Measured 002	63.24	$c = 2.938\text{Å}$
Measured 022	95.20	$\sqrt{a^2 - c^2} = 4.172\text{Å}$
Calculated		$a = 2.962\text{Å}$
Calculated relaxed lattice constant		$a_{relaxed} = 2.947\text{Å}$
Calculated strain		$\sigma_{x,y} = -0.17\%$, $\sigma_z = 0.10\%$

Table 2.4: Example strain calculation for T09-086 ($\text{Cr}_{0.76}\text{Al}_{0.24}$)

2.3 Chemical characterization

2.3.1 Cr-Al alloy concentration

The Al concentration x in $\text{Cr}_{1-x}\text{Al}_x$ films is controlled by the relative growth rates of Cr and Al in the growth chamber. Both the Cr and Al sources have crystal thickness monitors near the source in order to measure the amount of material being evaporated. In the case of Al, a relatively constant rate is obtained by keeping the effusion cell at a constant temperature (typically 1140°C) with the shutter open. Approximately one hour is needed for the temperature to equilibrate and the rate to become constant. For Cr growth by e-beam evaporation, the rate is highly sensitive to the power to the e-gun; the power is therefore determined by feedback from the crystal thickness monitor in PID mode as discussed in Section 2.1.2.

Crystal thickness monitors determine the rate or amount of material deposited at the position of the monitor. The rate or amount of material at the position of the substrate must be extrapolated using a tooling factor.[61] This tooling factor can vary slightly depending on, for example, the position of the electron beam on the Cr source, the topography of the Cr source surface which changes as deposition occurs (see Figure 2.2, and in the effusion cell, the amount of material evaporating from the sides of the crucible compared to the bottom, or any "droplets" near the mouth of the crucible.

Thus, while the alloy concentration can be roughly controlled by the relative growth rates, additional testing is required post facto in order to confirm more exactly the alloy concentration.

2.3.1.1 X-ray diffraction (XRD)

The simplest way to determine the Al concentration in $\text{Cr}_{1-x}\text{Al}_x$ alloys is through XRD. The lattice constant of $\text{Cr}_{1-x}\text{Al}_x$ increases linearly with x (to first order), following Vegard's law.[126] An example of this behavior is shown in Figure 2.16. Part (a) shows the decreasing trend in 2θ for the $\text{Cr}_{1-x}\text{Al}_x(002)$ peak with x for some $\text{Cr}_{1-x}\text{Al}_x(001)/\text{MgO}(001)$ films, with epitaxy and a nice (002) peak disappearing around $x = 0.40$. Part (b) shows a vs. x from literature data[18], showing approximately linear behavior in agreement with Vegard's law. To first order, the concentration x of our films is determined from interpolatation of this plot.
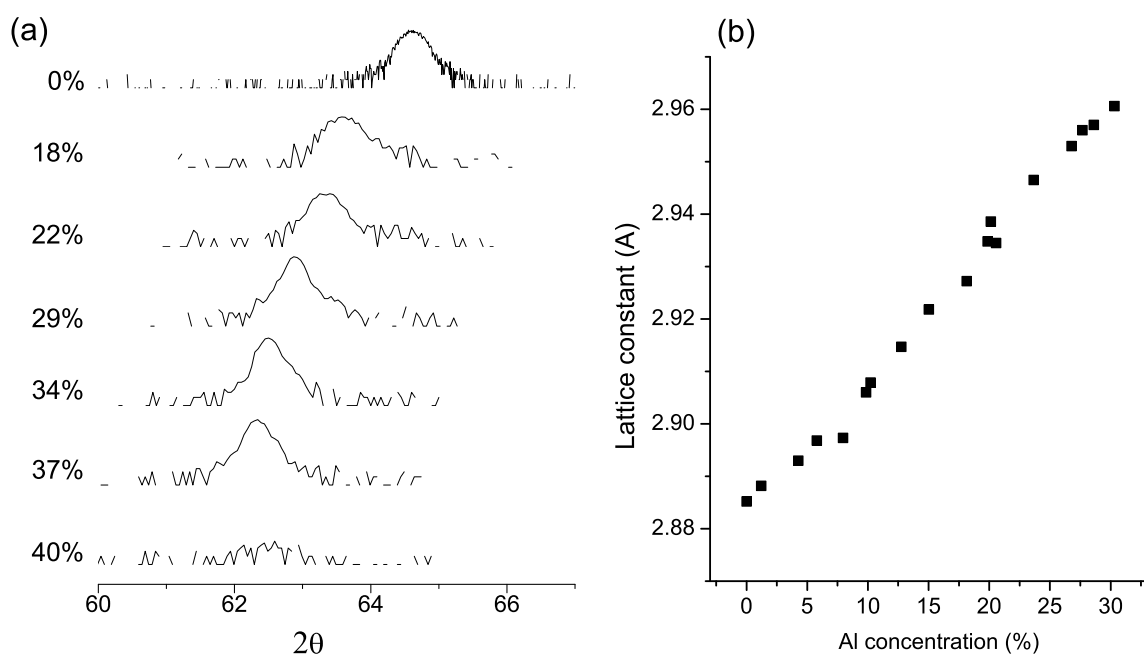
Figure 2.16: (a) XRD Cr(002) peak for $\mathrm{Cr}_{1-x}\mathrm{Al}_x$ samples grown on MgO(001). Data shown for samples T08-022, T08-059, T08-060, T08-062, T08-067, T08-068, and T08-070. (b) Bulk $\mathrm{Cr}_{1-x}\mathrm{Al}_x$ lattice constant vs. Al concentration, adapted from Ref. [18].
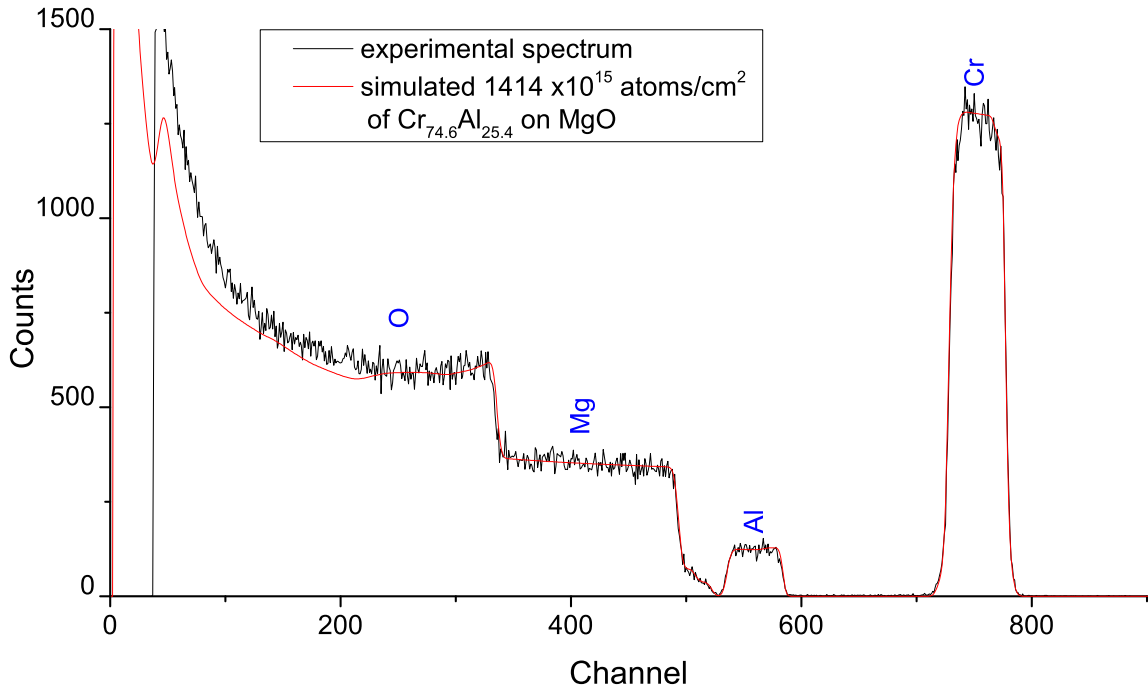
Figure 2.17: Experimental RBS spectrum of a 2000Å $Cr_{0.75}Al_{0.25}(001)/MgO(001)$ thin film with simulation for $1414 \times 10^{15}/cm^2$ atoms of $Cr_{0.746}Al_{0.254}$ to confirm concentration.

2.3.1.2 Rutherford backscattering spectroscopy (RBS)

While XRD is a good first step towards determining alloy concentration, other factors such as strain (see Section 2.2.2.2), or formation of ordered phases can also affect the lattice constant, so Rutherford backscattering spectroscopy (RBS) is also sometimes used in conjunction with XRD to confirm the alloy concentration.

RBS involves shooting a beam of approximately 3 MeV α-particles (He^{2+}) at the sample, and measuring the backscattered α-particles as a function of particle energy. Particles rebounding from large atoms retain most of their kinetic energy, while particles rebounding from smaller atoms transfer more of their energy to the sample atom. Thus, this is a good method for determining alloy concentrations, especially for elements with a reasonably large difference in atomic mass.

Software, for example SIMNRA[85], can be used to simulate an RBS spectrum and match the data to sample composition. An example is shown in Figure 2.17.

2.3.2 Sample purity

In addition to alloy concentration, chemical characterization is also necessary to determine sample purity. Contaminants of concern include: Ar (possibly incorporated from the sputtering process[58]), O (oxidation of the film), N (speculated to be absorbed
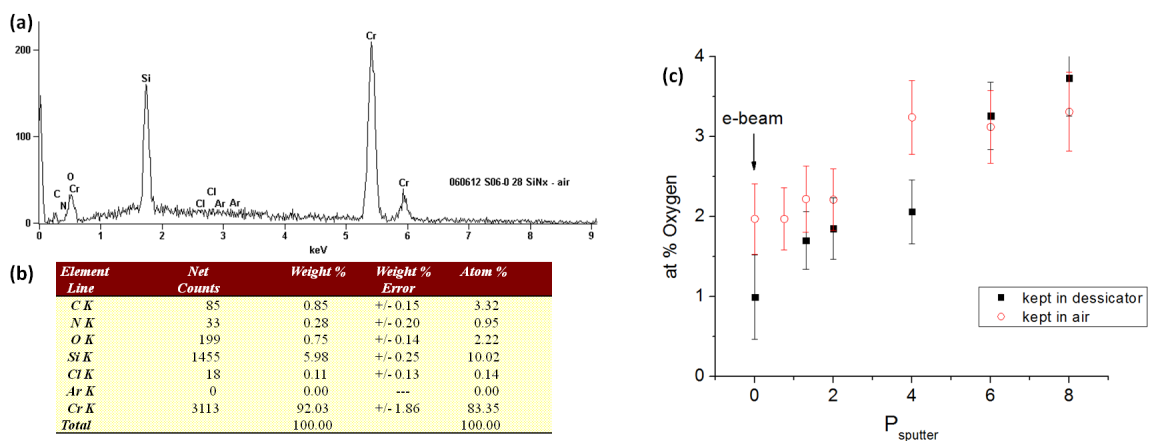
Figure 2.18: (a) EDX spectrum for an example Cr sample grown on an SiN_x/Si substrate (S06-028: sputtered 1.3 mTorr, kept in air). (b) Elemental analysis from the spectrum shown in (a). (c) At. % Oxygen vs. sputtering pressure, for sputtered Cr samples kept in either air or a vaccum dessicator.

by Cr[104], and it is known that Cr forms a stable nitride at higher temperatures[117]), and any other source materials from the growth chamber that may have contaminated the sources.

2.3.2.1 Electron dispersive x-ray spectroscopy (EDX)

Electron dispersive x-ray spectroscopy (EDX or EDS) is one method of determining trace sample contaminants. It is not as useful for quantitative analysis of films due to its extreme surface sensitivity. The EDX performed here was done inside the SEM used to image the thin film topography (Section 2.2.1.1.1). The electron beam from the SEM excites electrons in the sample, and when they relax again, they release photons with characteristic energies. The EDX detector scans for incoming photons as a function of energy. The reason for the surface sensitivity is the short (and acceleration-voltage dependent) penetration depth of the probing electrons, which enhances the signal from the surface compared to deeper in the sample. An example EDX scan, from a sputtered Cr film grown on an SiN_x/Si substrate is shown in Figure 2.18(a).

An approximate quantitative assessment of sample composition can be taken from the EDX spectrum, making the assumption that the sample composition is homogeneous (i.e. the surface is the same as the bulk of the sample). Figure 2.18(b) gives the composition derived from the spectrum in (a). The majority of the sample is Cr, as expected. A significant amount of Si is also seen, due to the SiN_x/Si substrate. The relative percentages show the extreme surface sensitivity, due to attenuation of the electron beam as it travels deeper into the sample. A very small amount of N is also observed, only barely outside the error bar. This can also be attributed to the SiN_x substrate.

In order to verify that the N is due to the substrate rather than contamination

of the Cr sample, a film grown on an SiO_2/Si substrate was also measured, and found to contain no N within error. A significant amount of C (about 5 at. %) was found in all measurements, including those of substrates known to be pure. This background level of C is likely due to organic contamination of the vacuum inside the SEM/EDX chamber. No incorporated Ar was found, and no evidence of contamination from other source materials in the chamber was found.

All Cr films showed some O contamination. This is not surprising, as Cr is known to form a surface oxide, and the EDX measurement is particularly surface-sensitive. An analysis of the O at. % found in a range of Cr samples is shown in Figure 2.18(c), showing an increase in O with increasing sputtering pressure. This increase could be explained due to the higher surface area of the rough films grown at high pressure (see Section 2.2.1.1.1), and therefore an increase in the amount of surface oxide. However, it is not possible to confirm this explanation from the EDX measurement.

A comparison was also made between films kept in under vacuum compared to those kept in air, in order to assess whether any oxidation occurred after growth. A slight increase in O at. % is seen for films kept in air, especially those grown at low pressures, although most of the measurements are within error of each other. We decided it was prudent to store Cr and $Cr_{1-x}Al_x$ samples under vacuum when possible.

2.3.2.2   X-ray photoemission spectroscopy (XPS)

Another method of assessing chemical composition was employed during the photoemission measurements shown in Chapter 5: X-ray photoemission spectrosocpy, or XPS. In the opposite process as EDX, a high energy (about 6 keV) synchrotron photon beam hits the samples, and electrons are ejected from the sample. The electrons are collected and counted as a function of their kinetic energy. Due to conservation of energy, the kinetic energy of the ejected electrons is equal to the incident photon energy minus the electron binding energy. Thus, a spectrum of electron binding energies is obtained, as shown in Figure 2.19(a). In the broad spectrum view, as shown in the Figure, characteristic peaks are seen which correspond to core level states for specific elements.

Figure 2.19(a) shows Cr and Al core level peaks from the sample, as well as C and O peaks due to contaminants. XPS is a surface-sensitive measurement, for the same reason as EDX (the short electron mean free path in the sample). Fortunately, a simulation program exists for XPS, called Simulation of Electron Spectra for Surface Analysis (SESSA), which can simulate the chemical composition of a sample taking into account the electron mean free path.[108] This simulation assumes the sample consists of multiple layers and is laterally homogeneous.

Figure 2.19(b-c) shows the simulated layers corresponding to the data in part (a). Both samples are assumed to have a thin layer of CO adsorbed on the sample, which is commonly seen in vacuum environments. Below this layer is a surface oxide, in the case of the Cr sample it is assumed to be Cr_2O_3, and in the case of the $Cr_{0.80}Al_{0.20}$ sample it is assumed to be Al_2O_3, due to the higher oxygen affinity of Al. The formation of a surface oxide rather than oxygen permeating through the sample is reasonable because both Cr and Al are known to form self-limiting surface oxides. The layers of both CO and oxide on both samples are found to be very thin (< 5Å each) from XPS.
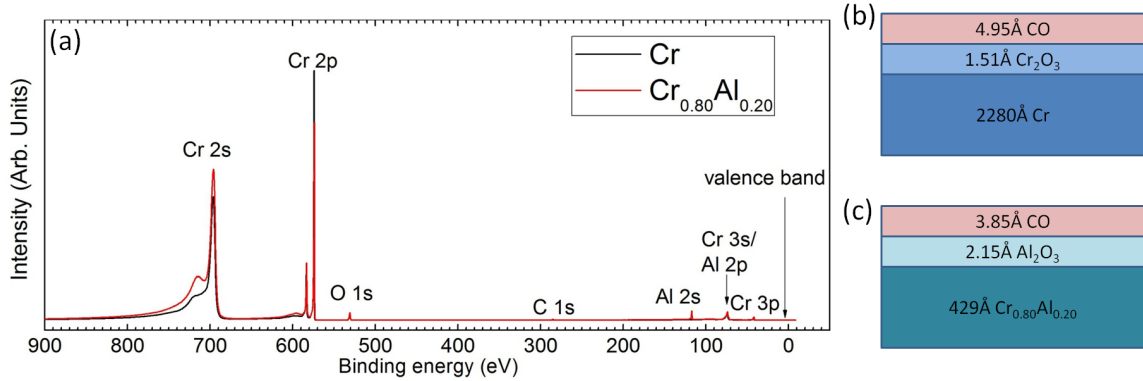
Figure 2.19: (a) Broad spectrum HXPS showing core levels of sample and contaminant C and O peaks. (b) Results of SESSA simulation for Cr reference sample ("bulk-like" Cr polycrystalline sample, sputtered at 0.75 mTorr and 350°C). (c) Results of SESSA simulation for $Cr_{0.80}Al_{0.20}$ sample (epitaxial on MgO(001), grown at 300°C).

2.3.2.3 O-resonant Rutherford backscattering spectroscopy (RBS)

Typically, RBS is good for detecting heavy elements but does not do well at detecting light elements ($Z \lesssim 10$) due to their low scattering cross section. However, the cross section is significantly increased at certain energies, where resonant nuclear scattering occurs. In oxygen-resonant RBS, the energy of the α beam is tuned to a resonance of the oxygen cross section, in our case about 3 MeV. Because the cross section is only increased for a very small range of scattering energies, and because of the energy loss of the α-particles as they travel through the film thickness, the detection of oxygen in a thin film is very depth-sensitive. In order to detect oxygen at a certain depth in the film, the energy of the α beam is tuned.

We used O-resonant RBS to determine if oxygen was present in our films. Figure 2.20 shows an example data set for a Cr film sputtered at 8 mTorr onto a room temperature SiN_x/Si substrate. The film shows about 12 at. % oxygen. We found that Cr sputtered at 8 mTorr contained oxygen even if it was capped with a Si layer in situ.

Table 2.5 shows the measured oxygen concentration in a range of films considered in this thesis. Oxygen concentration seems to be most correlated to the microstructure of the films during growth. The rough, porous Cr films sputtered at 8 mTorr have oxygen incorporated even if they are capped in situ. Most of the films considered here are non-porous and have no detected oxygen, for example Cr films sputtered at 1 mTorr, e-beam deposited films, or even Cr films sputtered at 8 mTorr but at elevated substrate temperature.
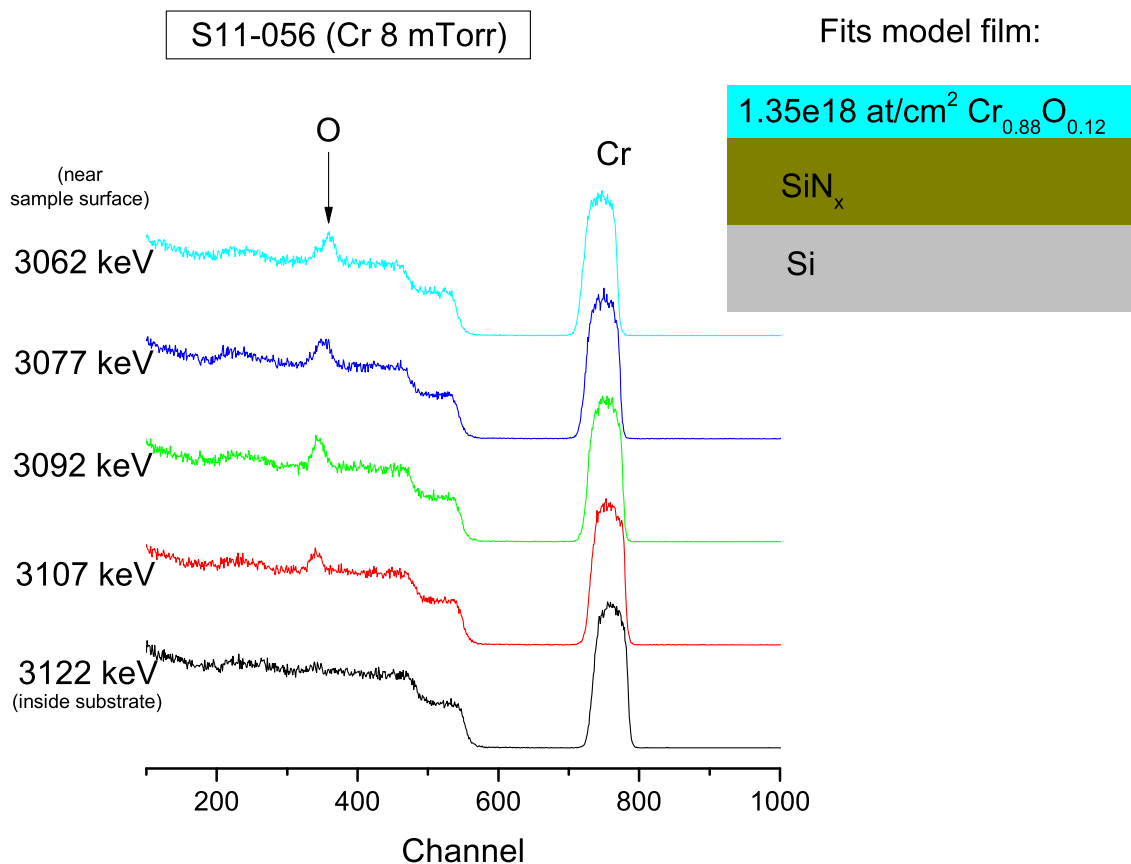
Figure 2.20: O-resonant RBS performed on a Cr thin film sputtered at 8 mTorr.

Sample	O at. % ($\pm$1%)
E-beam deposited $Cr_{0.75}Al_{0.25}$, 300°C substrate	0
Sputtered Cr, 1 mTorr, room temp substrate	0
Sputtered Cr, 4 mTorr, room temp substrate	6
Sputtered Cr, 8 mTorr, room temp substrate (capped or uncapped)	12
Sputtered Cr, 8 mTorr, room temp substrate, annealed ex situ 800°C	12 (23 surface)
Sputtered Cr, 8 mTorr, 350°C substrate	0

Table 2.5: Oxygen concentration of various films by O-resonant RBS

Chapter 3

Spin-density wave in polycrystalline Cr films from infrared reflectivity

3.1   Introduction

Chromium, as a spin density wave (SDW) material, has unique and extremely complex properties, and has been the focus of significant research. Prior to 1988, most research on Cr focused on bulk samples, and produced intricate phase diagrams in experiments that varied temperature, pressure, and binary and ternary alloying. The 1988 discovery of giant magnetoresistance (GMR) in Fe/Cr multilayers inspired further research on the SDW in Cr, and shifted the focus of that research towards films and multilayers, where other variables such as thickness, strain, and disorder are crucial.

The SDW in bulk Cr is incommensurate (ISDW), meaning that the wavelength is not an integer number of lattice constants. The transition to the paramagnetic state occurs at a Neel temperature (T_N) of 311 K. Small perturbations to the structure change the SDW to commensurate (CSDW), where the wavelength is an integer number of lattice constants, or to the paramagnetic state. The classic example of this sensitivity is that adding 0.3-1.0 at. % Mn into bulk Cr introduces a CSDW phase between the low temperature ISDW and high temperature paramagnetic phases; above 1.0 at. % Mn the ISDW phase is entirely replaced by the CSDW. On the other hand, with the addition of V the ISDW remains, but the Neel temperature slowly decreases until 4 at. % V, at which point the resulting material is paramagnetic at all temperatures. The explanation given for this is that the electron concentration is increased with the addition of Mn, while it is decreased with the addition of V (Cr has 6 valence electrons per atom, Mn has 7, and V has 5). The change in electron concentration disrupts the delicate Fermi surface nesting responsible for the ISDW [31].

In experiments involving thin films, the effects of physical confinement have been a main focus. Recent angle resolved photoemission spectroscopy (ARPES) measurements on epitaxial Cr(110) give direct evidence of band structure changing with film thickness in the range 30-120 Å [104]. In this thickness range, the low temperature state is ISDW, with a

phase transition to CSDW at higher temperatures. In addition, studies on exchange-biased epitaxial Fe/Cr(001) layers show that the ISDW wave vector differs from bulk at thicknesses as large as 1100 Å [93]. Below 1100 Å, T_N decreases from the bulk value of 311 K, and the period of the ISDW increases.

While excellent work has been done on epitaxial films, and indeed measurements such as ARPES require epitaxy, many of the Fe/Cr multilayers studied in the literature are polycrystalline. In fact, the degree of disorder in a multilayer is an important variable, as some research has analyzed the effects of surface roughness on GMR [23]. The goal of this project was to understand the SDW in polycrystalline Cr films such as those commonly used in GMR multilayers, where disorder and stress are the important variables.

We expect that stress and disorder will have a strong impact on the SDW character of our films. Stress has been shown empirically to affect SDW behavior of chromium in a similar way as the addition of Mn or V.[31] For example hydrostatic pressure decreases the Neel temperature (like the addition of V) while tensile stress introduces a CSDW (like the addition of Mn). Neutron diffraction experiments done on crushed chromium powder samples (having both stress and disorder) have shown a CSDW phase present above the ISDW phase in temperature (a similar effect as adding about 0.5 at. % Mn), thought to be due to local strains. In addition, the transition between ISDW and CSDW was blurred, with the two phases coexisting between about 200 and 300K [9, 135].

In bulk Cr, the ISDW is caused by nesting of the Fermi surface. A conceptual picture of the electron bands at the nesting site is given in Figure 3.1(a). In the ISDW, there are two gaps, a direct gap with energy 1000 cm^{-1} and an indirect gap with energy 3600 cm^{-1}.[31], labeled here as Δ_1 and Δ_2.

The CSDW occurs when the two empty bands shown in Figure 3.1(a) combine into one band instead of nesting next to each other (see Figure 3.1(b)), for example as a result of increasing the electron concentration. In that case, there is one direct gap, Δ_C. The energy of the commensurate gap has been calculated theoretically by Falicov and Penn [28] to be 2000 cm^{-1}, twice the energy of the incommensurate direct gap, and by Asano and Yamashita [7] to be 3200 cm^{-1}. Experimentally, the typical CSDW Cr dilute alloys Cr-Mn and Cr-Re are seen to have an energy gap between 2900 and 3200 cm^{-1} in the CSDW state [16, 31].

Another alloy, Cr-Al, with greater than 3 at. % Al, also has CSDW structure based on neutron scattering [62], but a gap of only 2400 cm^{-1}.[83] rather than the higher energies seen in Cr-Mn or Cr-Re alloys. Mn and Re, both group 7 transition metals, increase electron concentration when alloyed in Cr, causing the CSDW. In the case of Al, a nontransition metal, it is not clear how many electrons each Al atom contributes. Because of this, Cr-Al is not considered to be a typical CSDW alloy like Cr-Mn or Cr-Re. Experimentally, Cr-Al alloys have a high Neel temperature and high resistivity, which are not seen in other Cr alloys [31]. Cr-Al alloys with between 16 and 28 at. % Al show nonmetallic behavior, with a negative temperature coefficient of resistance. Korringa-Kohn-Rostocker coherent-potential approximation (KKR-CPA) band calculations have shown that Al atoms in substitutional sites behave very similar to vacancies in pure Cr because they do not participate in *d-d* bonding [3]. This causes significant scattering and can help explain the very high resistivities in Cr-Al alloys.
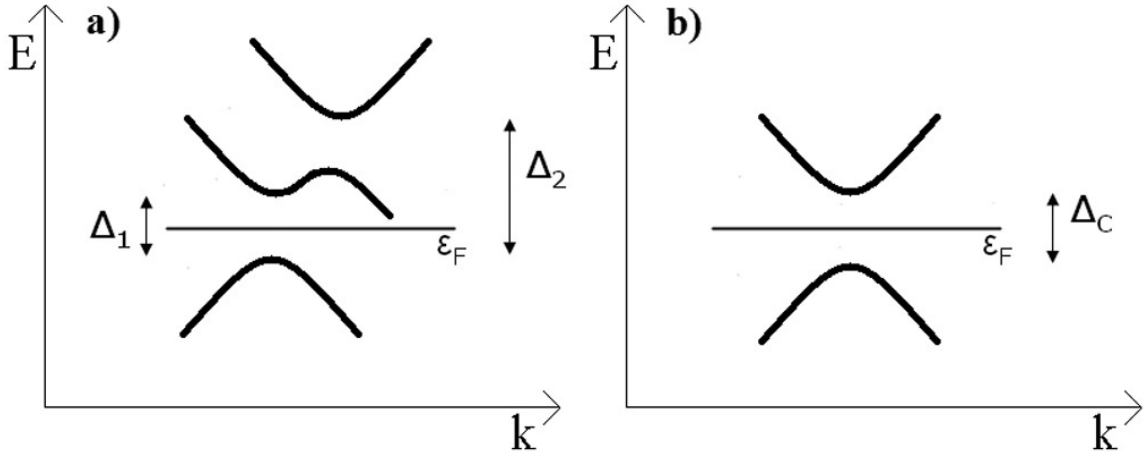
Figure 3.1: (a) Conceptual model of bands in the ISDW state; Δ_1 is the direct gap and Δ_2 is the indirect gap (b) bands in the CSDW state with gap Δ_C.

Infrared reflectivity as a function of frequency and temperature provides an excellent probe of the various SDW states of Cr. In this chapter, we describe the results of reflectivity measurements on polycrystalline films prepared under various deposition conditions. We observed four distinct gaps: 1000, 2400, 3200, and 3600 cm^{-1}, which we compare to the gaps seen in bulk Cr and its alloys. Based on the energy gaps observed, we categorize each sample by its SDW behavior. We observe three basic types of SDW behavior: ISDW, CSDW, and mixed phase. We then explain the results in terms of the stress and amount of disorder present in each film.

3.2 Experiment

We sputtered 200nm thick chromium films using an AJA magnetron sputtering system with a base pressure below 5×10^{-8} Torr. We varied the sputtering pressure between 0.75 mTorr and 8 mTorr. The gun was powered with 150W DC, and the films were deposited at rates of 0.5-1.0 Å/s onto substrates of amorphous SiN$_x$-coated Si held at room temperature. In addition to this series, one sample was sputtered at 0.75 mTorr at 350 °C; this sample had larger grains and exhibited bulk-like behavior; in the rest of the chapter this will be referred to as the "bulk-like" sample. One 150nm sample was also grown by e-beam deposition at a very low base pressure ($< 10^{-10}$ Torr), with the substrate held at room temperature. The samples, deposition conditions, and structural characteristics are summarized in Table 3.1.

Scanning electron microscopy (SEM) and cross-sectional transmission electron microscopy (TEM) imaging showed columnar morphology. SEM shows top-down views of the columnar structure (Figure 3.2(a-c)), allowing us to calculate the lateral grain size. The film grown at 8 mTorr had the largest grains; these are oblong and 25nm by 50nm. The film grown at 0.75 mTorr had slightly smaller grains and more variation in grain size. The

Sample	Growth Technique	Substrate Temp	Sputter Pressure (mTorr)	Grain size from XRD (nm)	Tensile stress (MPa) (± 10 %)	Residual Resistivity ($\mu\Omega$-cm)	Neel Temp (K)
e-beam	e-beam	RT	N/A	19	$900 \pm 30\%$	20	250
bulk-like	Sputter	350°C	0.75	35	580	6	300
0.75 mTorr	Sputter	RT	0.75	22	1310	16	>400
1.3 mTorr	Sputter	RT	1.3	19	1650	23	>400
2 mTorr	Sputter	RT	2	18	1290	32	>400
4 mTorr	Sputter	RT	4	22	580	100	262
6 mTorr	Sputter	RT	6	25	480	194	270
8 mTorr	Sputter	RT	8	28	260	402	221

Table 3.1: Table of samples used in this study: their growth properties, grain size, stress, residual resistivity, and Neel temperatures. Sputtered samples were 200nm thick and the e-beam sample was 150nm.

average grain is also oblong and 25nm by 35nm. The e-beam deposited sample showed very different structure from the sputtered samples, with some small round grains, some oblong grains, and some unusual multi-pronged grains. The average grain size for the e-beam sample was 15nm by 50 nm. The bulk-like sputtered film was imaged with SEM and no surface structure was visible, consistent with a very flat surface.

Transmission electron microscopy (TEM) images (see Figure 3.2(d-e)) showed that the film grown at high argon pressure had a rough, jagged surface, while the film grown at low pressure was very flat. In addition, the films grown at high pressure had small grains at the base of the film (7nm) growing into larger grains in the bulk with an average size of 18nm, with small amounts of amorphous material observed between columns. Because of the difference between material at or near the column boundaries (including some amorphous material) and material far from the column boundaries, as well as the grain growth with thickness, we consider these films to be inhomogeneous. The films grown at low pressure had a less well-defined columnar morphology, with no amorphous material observed and approximately 29nm grains throughout; we consider these films to be homogeneous. The TEM images shown are of 100 and 130nm thick films while the SEM and other experiments were done on 200nm thick films; the smaller lateral grain size observed in the TEM compared to the SEM images of the 8 mTorr sample is due to the grain growth with thickness in this sample.

X-ray diffraction was used to verify the Cr bcc structure, and showed no exotic crystal phases. While SEM gives the grain size in the lateral direction, the x-ray peak width allowed us to calculate the out-of-plane grain size. Grain size was determined from the dominant (110) peak width, and was not strongly dependent on sputtering pressure.[1]

---

[1] The calculations for grain size corrected for instrumental broadening, which was small.

These grain sizes are significantly smaller than the thickness; although the grain growth is columnar, defects break the coherence and lead to the grain sizes shown in Table 3.1.

Energy dispersive x-ray spectroscopy (EDS) done at 10 keV showed no Ar, N, or C contamination of the films, within the margin of error of 0.25 at. % for Ar and N, and 1.0 at. % for C (see [2]). Total Oxygen percentage was 2 at. % in the films grown at low pressure and the e-beam sample, and 4 at. % in the films grown at high pressure. Chromium is known to form a self-limiting oxide and these EDS results are consistent with a surface oxide layer given that the films grown at high pressure were rough and had about twice the surface area to oxidize.

Stress was measured using a Tencor FLX-2320 stress measurement system. The Tencor measures the curvature of a 4-inch Si wafer before and after a film is deposited. The stress in MPa is calculated from the difference in the two wafer curvature profiles, using the material properties of the Si substrate and the thickness of the film deposited. For the e-beam deposited sample, it was not possible to deposit onto a 4-inch wafer, so the stress was obtained indirectly from x-ray peak position measurements.[3] The stress of each film is noted in Table 3.1. Stress in sputtered films can be either compressive or tensile depending on the atomic weights of the sputtered material and sputtering gas, as well as the sputtering pressure and source-substrate distance.[4] [58]; here, we are in the tensile regime for all pressures. E-beam deposition also typically results in tensile stress (in the absence of epitaxy or differential thermal contraction)[115].

Electrical resistivity (ρ) vs. temperature was measured by a 4 point method. We do not show the temperature profiles here; however, the low temperature resistivity is strongly dependent on growth parameters, especially sputtering pressure, ranging from 5 to 400 $\mu\Omega$-cm, consistent with literature [121]. The residual resistivity (ρ_0) values are tabulated in Table 3.1.[5] The Neel temperature can be seen in $\rho(T)$; we locate the Neel temperature by the minimum in $d\rho/dT$ [40]. For our samples, the resistivity anomaly was quite broad due to the effects of strain and polycrystallinity. Three samples (0.75 mTorr, 1.3 mTorr, 2 mTorr) had Neel temperatures higher than we were able to measure (400 K).

Infrared reflectivity was measured using a Bruker FTIR Model 66v-S at beamline 1.4 of the Advanced Light Source (ALS). Each sample, along with a gold mirror, was mounted inside a cryostat with a KBr optical window, which was then placed into the FTIR. The cryostat and the FTIR optics were under rough vacuum. For each measurement, the reflectivity spectrum was measured 64 times and averaged using Opus software; the same was done for the gold mirror to measure the background. Finally, the background was subtracted to give the reflectivity spectrum from the sample. Reflectivity was measured for

---

[2]An additional film was grown on a Si thermal oxide substrate so at. % N could be measured without observing a signal from the SiNx substrate. For at. % C, the EDS chamber had a background 5 ± 1 at. % C signal which obscured the measurement; the margin of error for the at. % C measurement is therefore 1 at. %.

[3]The stress in the e-beam sample was determined using x-ray diffraction, by correlating the measured out-of-plane lattice constant to those of the other samples with known stress. This assumes a similar stress-strain relationship and Poisson's ratio for all the polycrystalline samples.

[4]The source-substrate distance for our samples was about 20cm.

[5]All films show a resistivity minimum below 100K, and we report the residual resistivity as the resistivity at the minimum. The magnitude of the low temperature upturn is small, representing no more than 1% of the total resistivity.
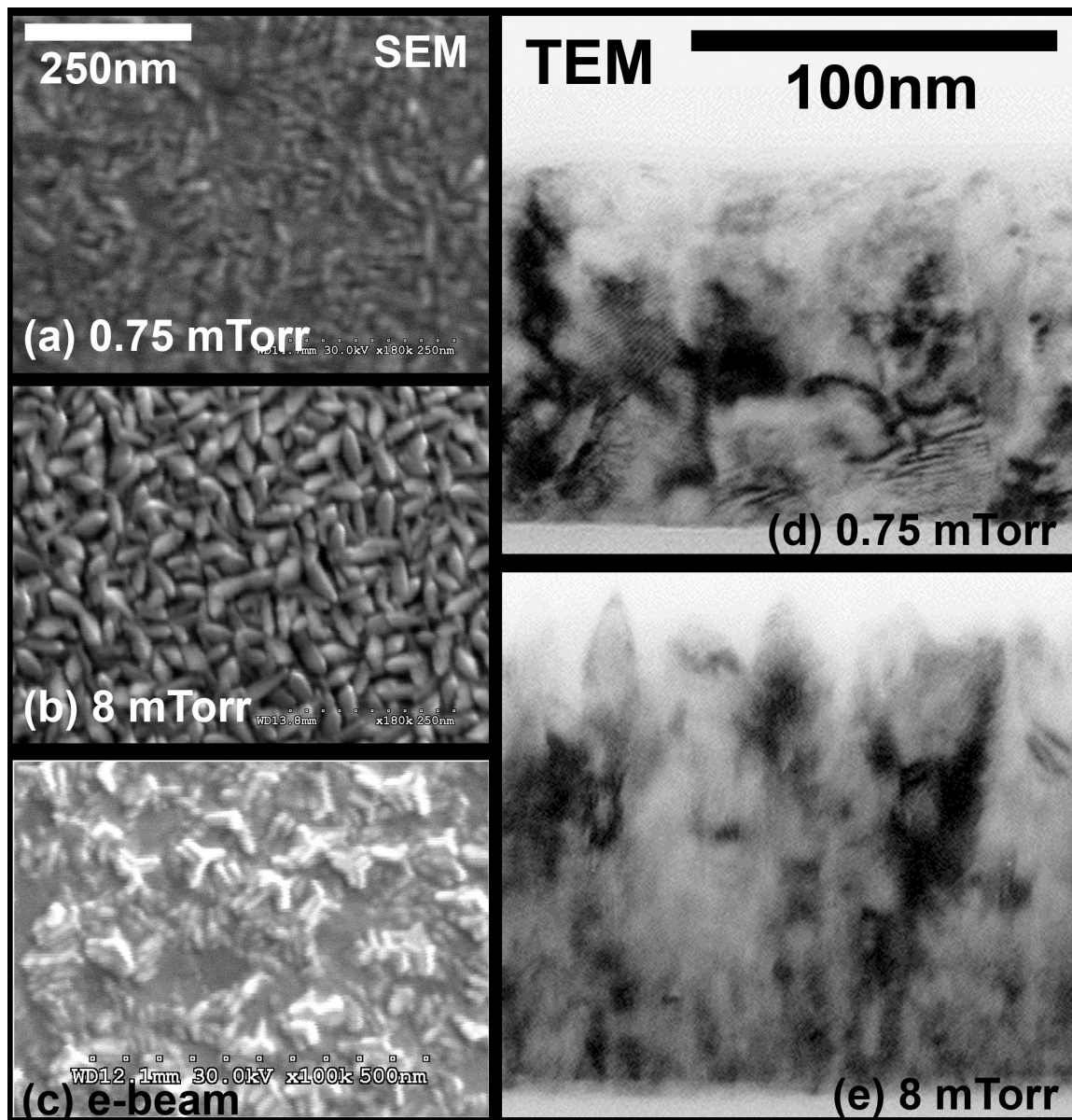
Figure 3.2: (a-c) SEM top-down images of samples: (a) 0.75 mTorr (b) 8 mTorr (c) e-beam. The bulk-like film was also imaged by SEM and no structure was observed. (d-e) Cross-sectional TEM images: (d) 0.75 mTorr (100nm) (e) 8 mTorr (130nm). TEM was done on 100 and 130nm thick films.

each sample at multiple temperatures.

3.3   Results

The mid-IR reflectivity for each sample was measured as a function of temperature, in order to observe the SDW gap features in the spectrum expected to occur between 800-4000 cm^{-1}. We took data between 500-7000 cm^{-1}, and applied an adjacent-averaging smoothing technique with a width of 100 cm^{-1} over most of the data set. Above 4500 cm^{-1} the intensity of the mid-IR lamp was lower, leading to a higher noise level, so in this region we used a smoothing width of 300 cm^{-1}. Example data sets are shown for the bulk-like sample in Figure 3.3(a) and the 1.3 mTorr sample in 3.3(b). In Figure 3.3, we see that the reflectivity of both samples generally decreases with wavenumber for all temperatures. In addition, at low temperature gaps are observed which disappear as the temperature is increased.

In order to clearly determine the SDW energy gaps and compare them to literature, we focus primarily on the low temperature (10K) reflectivity, and the reflectivity ratio (RR), which is the ratio of the low temperature reflectivity to that at high temperature (above the Neel temperature). To plot the RR, we have determined a Neel temperature for each film from a minimum in dρ/dT, shown in Table 3.1. For the low pressure samples the Neel temperature could not be reached in the reflectivity apparatus, so data at the maximum temperature (400 K) was used as an approximation. Figure 3.3(b) shows that in the 1.3 mTorr sample the SDW gap at 3200 cm^{-1} is nearly gone by 400 K; similar data was found for the 0.75 mTorr and 2 mTorr samples (not shown). Thus, the Neel temperature is not significantly higher than 400 K, so using the 400K data for the reflectivity ratio is a good approximation.

The reflectivity at 10 K is plotted for all samples in Figure 3.4(a-c) and the RR in Figure 3.4(d-f). The data show three distinct SDW behaviors at low temperature. Two exhibit the ISDW seen in bulk Cr (the bulk-like and e-beam samples), three exhibit a CSDW as seen in Cr-Mn (the sputtered samples grown at the lowest pressures), and three show gaps corresponding to multiple SDW phases (the sputtered samples grown at the highest pressures). The data in Figure 3.4 is separated into these three distinct SDW behaviors.

The reflectivities of the ISDW samples are shown in Figure 3.4(a), with the reflectivity of bulk Cr plotted for comparison. The reflectivities of both films closely resemble that of bulk, with the gap at Δ_1 apparent; the indirect gap at Δ_2 is not obvious in either sample or in bulk Cr. The reflectivity of the commensurate SDW samples is shown in Figure 3.4(b), with the reflectivity of two typical CSDW alloys, Cr-Mn and Cr-Re, plotted for comparison. We see the commensurate gap Δ_C at wavenumber 3200 cm^{-1}, within the range of observed commensurate gap energies seen in Cr-Mn and Cr-Re. The three samples with mixed SDW are shown in Figure 3.4(c), with bulk Cr plotted for comparison. The reflectivities of these three films are quite different from bulk, with a lower absolute reflectivity overall and no features readily apparent.

We now turn to the reflectivity ratio, plotted for the ISDW samples in Figure 3.4(d), for the CSDW samples in Figure 3.4(e) and for the mixed SDW samples in Figure 3.4(f). For the ISDW samples, plotting the ratio reveals the broad gap at Δ_2 that
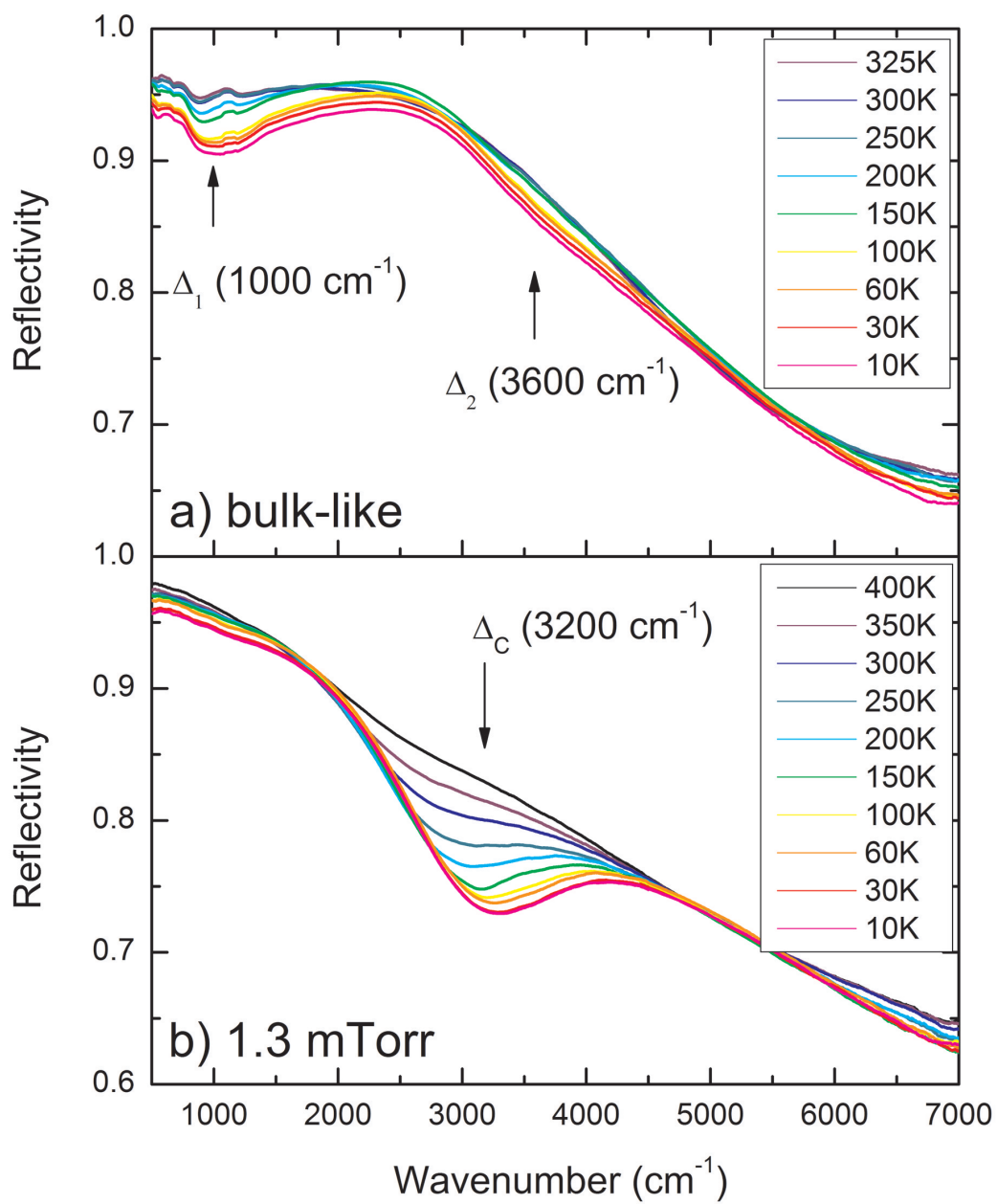
Figure 3.3: Reflectivity of (a) bulk-like and (b) 1.3 mTorr samples at temperatures between 10K and 400K.
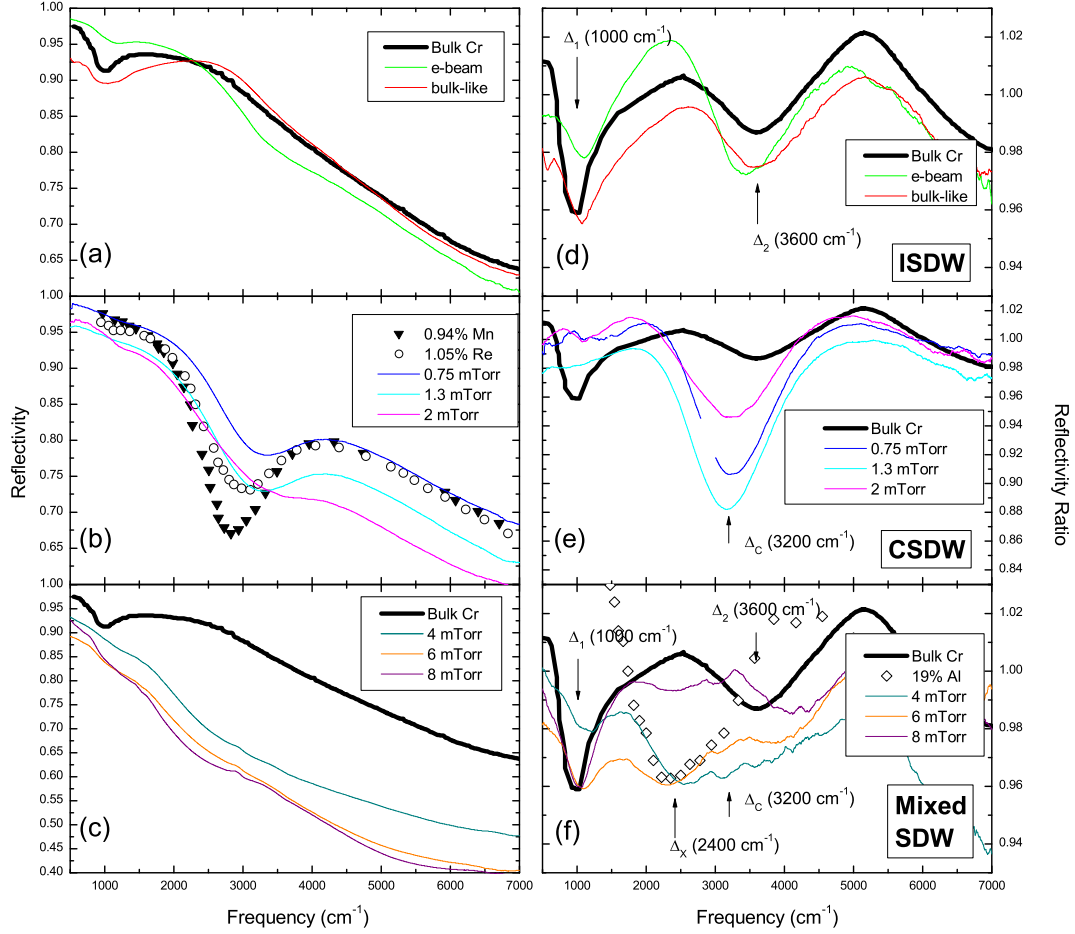
Figure 3.4: Reflectivity at 10 K of: (a) ISDW samples (bulk-like and e-beam) compared to bulk Cr (b) CSDW samples (0.75, 1.3, and 2 mTorr) compared to Cr-Mn and Cr-Re (c) Mixed SDW samples (4, 6, and 8 mTorr) compared to bulk Cr. Reflectivity ratio ($R_{LowTemperature}/R_{Paramagnetic}$) of: (d) ISDW samples - bulk-like (R_{10K}/R_{325K}) and e-beam (R_{10K}/R_{400K}) compared to bulk Cr (e) CSDW samples - 0.75, 1.3, and 2 mTorr (R_{10K}/R_{400K}), compared to bulk Cr; no Cr-Mn or Cr-Re RR data was available for comparison (f) Mixed SDW samples - 4, 6, and 8 mTorr (R_{10K}/R_{400K}, R_{10K}/R_{350K}, and R_{10K}/R_{300K} respectively) compared to bulk Cr and Cr-Al. Bulk Cr reflectivity given at 30K, ratio is R_{30K}/R_{325K} from Lind and Stanford [82], reflectivity at 4K of Cr-Mn and Cr-Re alloys from Bos and Lynch [16]. Reflectivity ratio (R_{30K}/R_{400K}) of Cr-Al alloy from Lind and Stanford [83].

was difficult to notice in the absolute reflectivity. For the CSDW samples an interesting result of plotting the ratio is that, while the dip in the reflectivity looks somewhat different for the three samples, the gap energy Δ_C (3200 cm^{-1}) as seen in the ratio is actually extremely close for all three film samples. Also, the 2 mTorr sputtered sample shows a small but visible dip a Δ_1, which suggests that the sample has small regions of ISDW, although we still classify this film as CSDW. In what we have called the mixed SDW samples, three features are evident. First, the ISDW direct gap, Δ_1 is visible, although broadened somewhat perhaps due to disorder. The indirect gap, Δ_2 is not clear; possibly it is broadened so much that we cannot see it at all. In addition, there is a small dip at Δ_C, showing that parts of the films have CSDW. Finally, we observe an additional gap at 2400 cm^{-1}, labeled as Δ_X. We recognize this gap energy as the same seen in the atypical CSDW Cr-Al alloys [83], also plotted in Figure 3.4(e) for reference. We conclude that the Cr samples grown at 4, 6, and 8 mTorr have multiple coexisting phases: ISDW (as in bulk Cr), and two distinct forms of CSDW (as in Cr-Mn and Cr-Al). Because we know these films are morphologically inhomogeneous, as evidenced from the TEM image of the 8 mTorr film, it is not surprising that ISDW and CSDW coexist; however the fact that we see two distinct CSDW gaps is surprising.

Previous research on Cr and its dilute alloys has often shown CSDW occurring as a high temperature phase, with ISDW as a low temperature phase (rarely the other way around) [31]. In order to determine the temperature dependence of the SDW in our films, we plot the reflectivity ratios for a range of temperatures, to see how the gaps change with temperature. This data is plotted for a representative sample of each type in Figure 3.5. Figure 3.5(a) shows the bulk-like sample; the closing of the two ISDW gaps is visible up to 300K, consistent with our measured Neel temperature of 300K. In Figure 3.5(b), we show the 1.3 mTorr sample; again the CSDW gap (Δ_C) is seen closing up to 375K, consistent with a Neel temperature slightly above 400K. The 4 mTorr sample is shown in Figure 3.5(c). We see that the gap at 1000 cm^{-1} (Δ_1) and the one at 3200 cm^{-1} (Δ_C) disappear by 200 K. In addition, the second ISDW gap (Δ_2), which could previously not be distinguished, is now visible as a slight depression at 3600 cm^{-1} which also disappears by 200K. The Neel temperature for this sample is 262 K, as measured by a minimum in dρ/dT. Given the broad nature of the resistivity anomaly in these films, these temperatures are fairly consistent. Interestingly, the gap at 2400 cm^{-1} is still present up to at least 350 K. Thus, the measured resistivity anomaly in these films pertains only to the closing of the ISDW and one of the CSDW gaps (3200 cm^{-1}), while the other CSDW gap (2400 cm^{-1}) remains to higher temperatures. This point extends the comparison to Cr-Al alloys, which typically have high Neel temperatures [31]. The other CSDW (0.75, 2 mTorr) and mixed SDW (6, 8 mTorr) samples' behavior do not differ significantly from the representative data sets shown in Figure 3.5(b-c).

The e-beam sample, which appeared from reflectivity and RR data to be ISDW and similar to the bulk-like sample (see Figure 3.4(a and d)), has temperature dependent behavior which differs from the simple ISDW shown by the bulk-like sample in Figure 3.5(a). We show that behavior in Figure 3.6. Figure 3.6(a) shows the reflectivity spectra at multiple temperatures. The two ISDW gaps Δ_1 and Δ_2 disappear by 200K and instead, a single gap opens which looks similar to the CSDW gap observed in reflectivity in Figure 3.4(b).
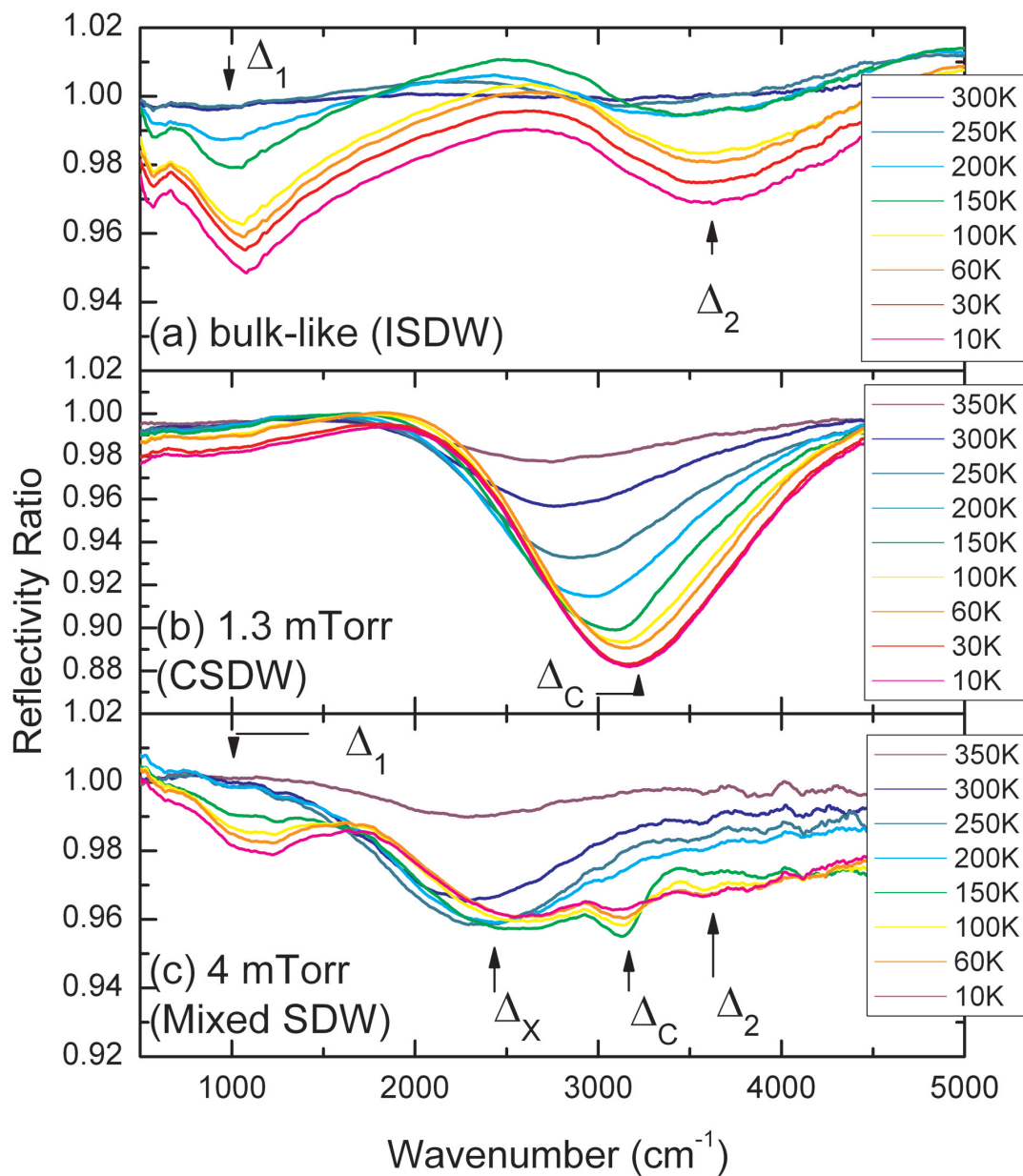
Figure 3.5: Reflectivity ratio (R_L/R_P) for R_L taken at multiple temperatures: (a) bulk-like sample (ISDW) (b) 1.3 mTorr sample (CSDW), (c) 4 mTorr sample (mixed SDW). R_P is taken at 325K for (a) and 400K for (b) and (c).
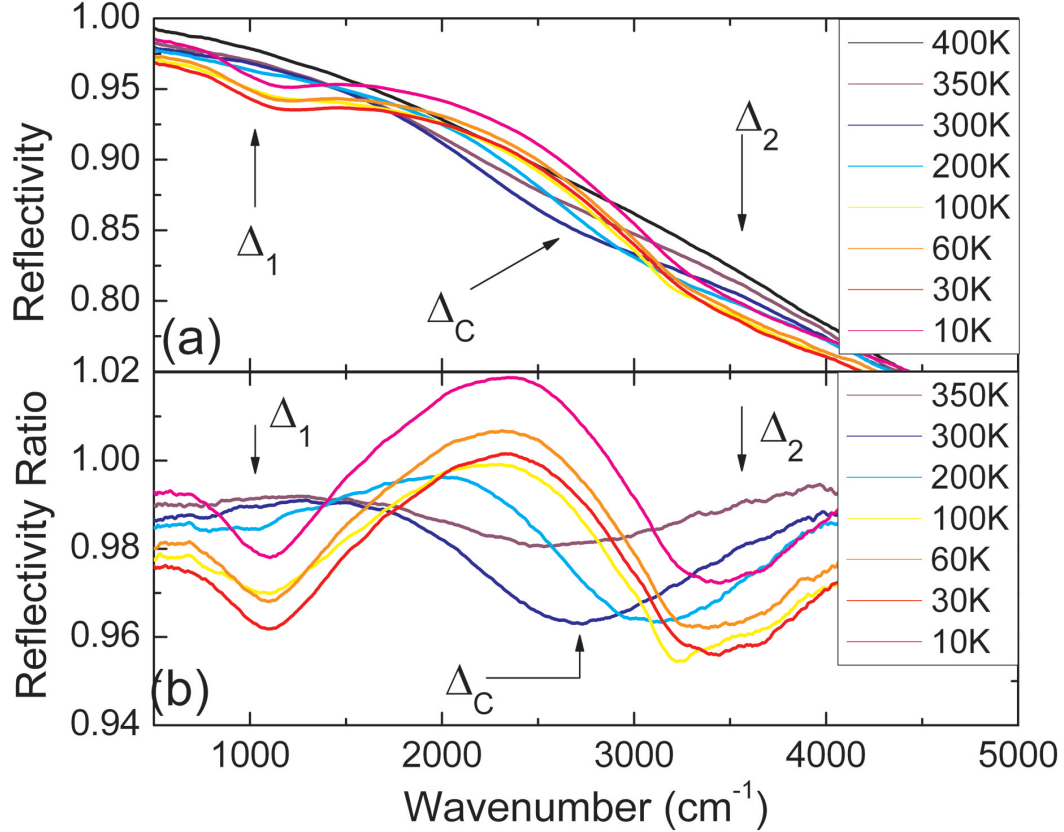
Figure 3.6: (a) Temperature dependent reflectivity and (b) reflectivity ratio (R_L/R_{400K}) of e-beam sample.

This gap disappears again by 400K. Figure 3.6(b) gives the reflectivity ratio, which shows clearly the transition from ISDW to CSDW at around 200K. This is the only sample which shows such a transition. We refrain from stating the gap energy of this commensurate phase because quoted values for gap energy generally refer to the gap at zero temperature. The actual gap energy decreases with increasing temperature.

3.4 Discussion

The two fundamental distinguishing properties in these films are stress and disorder. Grain sizes are similar in all but the bulk-like sample, and yet three distinct reflectivity profiles are observed, so grain size alone is not a determining factor. However, the quality of the grain boundaries and surface roughness vary significantly, and defects within the grains are sources of disorder. We propose a low-temperature phase diagram for chromium as

determined from our experimental results, with stress and disorder along the two axes and show this in Figure 3.7. For the y-axis (stress) we have used the measured stress in the films (MPa) and on the x-axis (disorder) we have used the residual resistivity, ρ_0 ($\mu\Omega$-cm) listed for each sample in Table 3.1. Each sample corresponds to a point on this map, with bulk Cr at the origin. Based on our reflectivity results, we demarcate three regions corresponding to the three SDW behaviors we observe: ISDW occurs in the region with low stress and low disorder, CSDW occurs in the region with high stress and low disorder, and mixed SDW phases occur in the region of low stress and high disorder. None of our samples fall into the region of high stress and high disorder.

This low temperature phase diagram is almost entirely sufficient to describe the SDW behavior of our samples, because all but one transition directly from their low temperature behavior to the paramagnetic state, albeit at different Neel temperatures. Only the e-beam sample has an exclusively high temperature SDW phase, exhibiting a transition ISDW $\rightarrow$ CSDW at around 200K before transitioning to the paramagnetic state at around 400K.

Let us focus on the stress dependence of the SDW by examining the samples with low disorder. The film with the lowest stress (bulk-like) displays ISDW behavior over the whole temperature range, while the films with the most stress (grown at 0.75 mTorr, 1.3 mTorr, 2 mTorr) display CSDW behavior over the whole temperature range. The film with stress between these, the e-beam sample, displays ISDW at low temperature and CSDW at higher temperatures. This dependence of SDW behavior on stress mirrors the dependence on Mn concentration described in the introduction. In fact, it is surprising that so many of our samples showed CSDW *without* a lower temperature ISDW phase; this speaks to the very high stress present in the films.

While the ISDW $\rightarrow$ CSDW transition observed in the e-beam sample is not unusual [31], it is particularly pertinent in this case because it corroborates the results of other studies done on e-beam deposited Cr [104]. Rotenberg et al. have grown epitaxial Cr(110)/W(110) by e-beam evaporation, and used in situ ARPES measurements to study very thin samples (30-120Å). They observed a transition from ISDW $\rightarrow$ CSDW at a temperature that increased with increasing thickness. An extrapolation of their curve predicted that at large thicknesses, their films would still exhibit an ISDW $\rightarrow$ CSDW transition at 187 K, in disagreement with bulk behavior. Our 1500Å film, grown under the same conditions (although not epitaxial or annealed) does in fact show such a transition near 200 K. This result supports Rotenberg's findings, and suggests film stress plays a crucial role in this transition.

Next, let us focus on the mixed SDW samples. Unlike the e-beam sample, which shows different SDW behavior in different temperature ranges, the mixed SDW samples exhibit multiple different SDW behaviors coexisting within the same temperature range. Previous work on crushed powders showed ISDW and CSDW coexisting within one sample; the coexistence disappeared upon annealing [9]. This suggests that coexisting phases are due to an inhomogeneous sample or defects in a sample. This is likely the case for our samples, based on the inhomogeneity observed in the TEM images.

The most surprising result of the mixed SDW samples is that we observe an additional CSDW gap at 2400 cm^{-1}, like that observed in Cr-Al, coexisting with the ISDW and
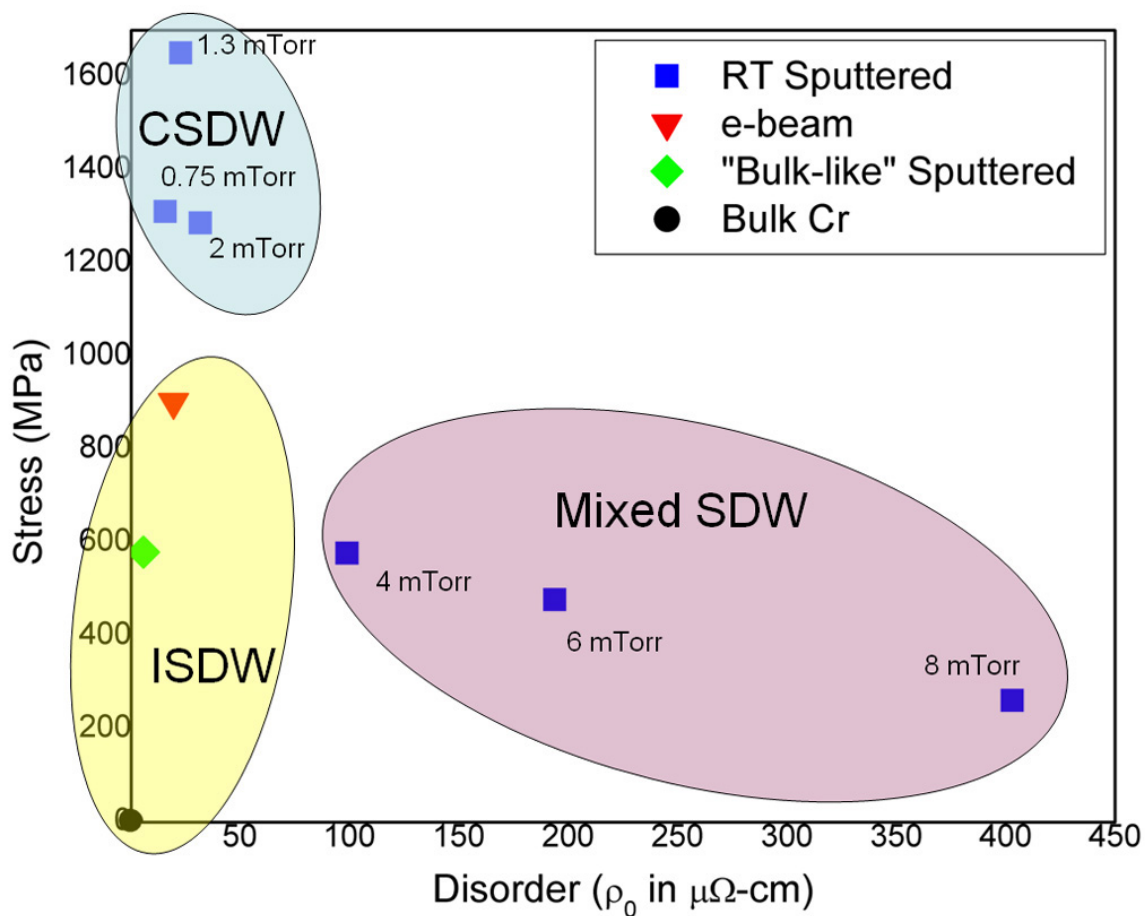
Figure 3.7: Phase diagram for the low temperature magnetic state of Cr films, in the disorder-stress plane. The axes are the residual resistivity ($\mu\Omega$-cm), representing disorder, and tensile stress (MPa). Phases are ISDW, CSDW, and mixed phase. The e-beam sample has a transition from ISDW to CSDW at 200K which is not accounted for in this low temperature phase diagram.

CSDW gaps which we recognize from our other samples. Because we only observe the 2400 cm^{-1} gap in the high resistivity samples, we attribute it to regions with high defect concentrations which are not present in the other films. In particular, we expect that material at or near the grain boundaries contributes to this phase. The high resistivity found in Cr-Al alloys, as well as the theory that substitutional Al atoms act as vacancies in Cr [31, 3], gives support to the analogy we draw between Cr-Al alloys and the most disordered regions of our high resistivity samples. As for the other gaps, the 3200 cm^{-1} CSDW gap, also observed in the 0.75, 1.3, and 2 mTorr films, and the ISDW gaps, also seen in the bulk-like and e-beam samples, we attribute to regions of high crystalline quality, far from the grain boundaries. Either different amounts of tensile stress or the different grain sizes observed throughout the thickness of the film cause the regions to differentiate between CSDW and ISDW.

3.5   Conclusions

In summary, we have used infrared spectroscopy to determine the spin density wave properties of polycrystalline chromium thin films. The behavior of this system is strongly dependent on the deposition conditions, and the diversity of behavior is remarkable, considering that it includes only one element and a single bcc structure. Here, we highlight the main findings of this chapter:

1. We observe three types of spin density wave (SDW) behavior at low temperature for polycrystalline Cr thin film samples:

    (a) Incommensurate SDW, in films with low stress and low disorder.

    (b) Commensurate SDW, in films with high stress and low disorder.

    (c) Mixed SDW, in films with low stress, high disorder, and an inhomogeneous microstructure.

2. The film with the largest grains, lowest residual resistivity, and low stress (the "bulk-like" sample, sputtered at 0.75 mTorr with the substrate at 350 $^\circ$ C) has magnetic structure which closely mimics bulk chromium.

3. The e-beam sample showed ISDW behavior at low temperature, transitioned to CSDW near 200K, and became paramagnetic near 400K. No other sample showed an ISDW $\rightarrow$ CSDW transition.

4. Samples with mixed SDW had gaps corresponding to the ISDW and CSDW phases observed in the other samples, plus an additional gap at 2400 cm^{-1}, which we attribute to CSDW in highly disordered regions of the sample. We compare this gap to the one seen in CSDW Cr-Al alloys.

Chapter 4

Resonant impurity scattering and electron-phonon scattering in the electrical resistivity of Cr thin films

4.1 Introduction

Bulk chromium is an itinerant antiferromagnet with an incommensurate spin density wave (ISDW) and has been widely studied as an archetypal band antiferromagnet. [30] The SDW in bulk Cr is very sensitive to perturbation by dopant atoms, pressure, etc. In particular, the ISDW switches to a commensurate SDW (CSDW) with the addition of a few percent Mn and disappears altogether with the addition of V. A large body of research exists on the effects of various dopants in Cr. [31, 127, 45, 44, 46, 47, 96, 103, 97, 100, 19, 113]

In addition to changing the SDW state, dopant atoms lead to interesting features in the resistivity. These features are described by the theory of resonant impurity scattering, which results from itinerant antiferromagnetism. The theory predicts localized impurity states within the "forbidden" SDW gap. When those states exist near the Fermi energy, resonant scattering occurs. In the prototypical system, $Cr_{1-y-x}Fe_y(Mn,V)_x$, resistivity minima and residual resistivities up to 25 $\mu\Omega$ cm have been observed; the effect is attributed to resonant impurity scattering off of the Fe impurities, with Mn and V (+1 and -1 valency compared to Cr) used to tune the Fermi level through the impurity energy levels.[127, 45, 44, 46, 47] Resistivity minima due to resonant scattering have also been seen in many binary Cr alloys, including Cr-V, Cr-Mo, Cr-Al, Cr-Ge, and Cr-Si.[31] Recently, more detailed resistivity analyses including the effect of resonant impurity scattering have been performed on Cr-Si, Cr-Fe, Cr-Ga-(Mn,V), and Cr-Ru-V.[96, 103, 97, 100]

Theoretically, the type of impurity atom is not very important to formation of a localized state, and even defects in pure Cr should lead to resonant impurity scattering.[127] This has never been observed in bulk samples, presumably because the density of defects is very small. However, polycrystalline Cr films provide many defects in the form of grain

boundaries, point defects, and dislocations. Defects and strain found in polycrystalline Cr films have already been shown to cause changes in the SDW state: in Chapter 3, an infrared reflectivity study of the SDW gaps in Cr films showed that Cr films have incommensurate, commensurate, or mixed SDW states depending on film deposition conditions.[15]

In the literature, Cr thin films have been shown to have very high resistivities[121, 76, 5, 15], but with little to no explanation of the reason. Hoffman and Thornton showed that the room-temperature resistivity of sputtered Cr films increases strongly with increased sputtering gas pressure, up to an extremely high value of 2000 $\mu\Omega$ cm; they attributed the high resistivity to a structure of columnar grains with low density grain boundaries, a structure that is often observed when low-Z materials are sputtered at high sputtering gas pressure.[121] However, such high resistivities are not observed for similar materials such as Fe under the same deposition conditions.[29]

In addition to defect and impurity scattering, electron-phonon scattering is a significant contribution to the resistivity. According to Matthiessen's rule, the addition of defects and impurities should add a temperature-independent term to the resistivity without affecting the temperature-dependent electron-phonon resistivity.[11] We suggest this is an overly simplistic assumption in the case of Cr. Not only do defects and impurities add a temperature-dependent term to the resistivity due to resonant impurity scattering, but electron-phonon scattering, which contributes the linear term to the resistivity, can also be affected by defects. A recent specific heat study of polycrystalline sputtered Cr films found a decrease in the Debye temperature from the bulk value due to a softening of the lattice. There was also an increase in the electronic specific heat coefficient γ for samples grown at high sputtering pressure which is explained by a disorder broadening induced increase in the electron density of states $N(E_F)$ and a resultant increase in the electron-phonon coupling constant λ.[22] Both of these effects would be expected to impact Matthiessen's rule.

In this chapter, we present the temperature-dependent resistivities of epitaxial and polycrystalline Cr thin films. We fit the resistivity curves to a model which includes electron-phonon scattering and resonant impurity scattering in the temperature range below 150 K where the contribution to the resistivity from magnetic fluctuation scattering around the Neel temperature is negligible. The films are presented in three series. First, we present a series of 3 films grown by electron beam (e-beam) evaporation on different substrates with varying degrees of epitaxy to test the effect of epitaxy and grain boundaries on the resistivity. Next, we present a series of polycrystalline sputtered films grown at different sputtering pressures which varies the columnar morphology as described above.[121] Finally, we present a series of annealed films, taking the highest resistivity film and annealing it at a series of temperatures in order to better understand the nature of the defects in these films.

4.2 Experiment

The first series of films was grown by e-beam evaporation at a rate of 0.3 Å/s and a base pressure below 5×10^{-8} Torr. The films in this series were grown at the same time onto three different substrates: MgO (001), Al_2O_3 (0001) (c-plane sapphire), and amorphous SiO_2-coated Si, held at 300 °C during growth. Cr is well known to grow epitaxially, in the

SEM: 250nm

(a) e-beam Cr/Al$_2$O$_3$
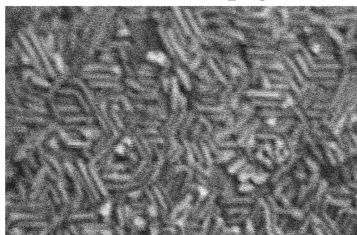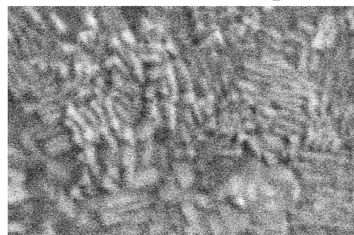
(b) e-beam Cr/a-SiO$_2$/Si

(c) sputtered 0.75 mTorr
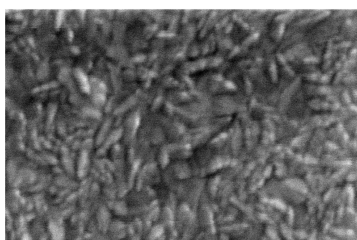
(d) sputtered 8 mTorr

(e) 8 mTorr ann. 800 $^{\circ}$C
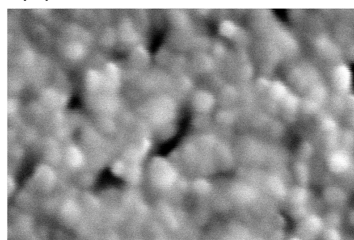
TEM: 100nm

(f) sputtered 0.75 mTorr
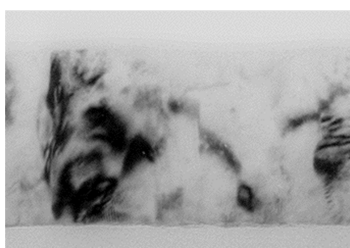
(g) sputtered 8 mTorr
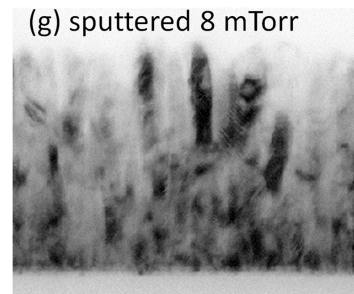
Figure 4.1: (a-e) SEM top-down images of samples: (a) e-beam deposited Cr/Al$_2$O$_3$, (b) e-beam deposited Cr/a-SiO$_2$/Si, (c) sputtered 0.75 mTorr, (d) sputtered 8 mTorr, (e) sputtered 8 mTorr annealed at 800 °C (f-g) Cross-sectional TEM images: (f) sputtered 0.75 mTorr (100nm film), (g) sputtered 8 mTorr (130nm film).

(001) orientation, on MgO (001).[38] The Cr lattice constant is approximately $\sqrt{2}$ smaller than the MgO lattice constant, causing the film to grow 45 ° rotated from the MgO. Cr exhibits (011) textured growth on Al_2O_3 (0001) induced by epitaxy. The epitaxy occurs in nine distinct orientation relationships, leading to a polycrystalline film with grains of the different orientations.[128, 124] Finally, Cr grows polycrystalline, without a specific orientation, on the a-SiO_2/Si.

Reflection high energy electron diffraction (RHEED) of Cr on MgO during growth shows a streaky pattern, consistent with 2D epitaxial growth. X-ray diffraction (XRD) shows a strong Cr (001) peak, with no other orientations, in a θ-2θ scan. In a ϕ scan (azimuthal scan) of the 45° off-axis Cr (011) peak, 4-fold symmetry is observed, confirming epitaxy. For Cr growth on Al_2O_3 (0001), RHEED shows a spotty pattern, which suggests 3D epitaxial growth, and only the Cr (011) peak is seen in an XRD θ-2θ scan. A ϕ scan of the 45° off-axis Cr (002) peak showed 6 broad peaks, consistent with the nine orientation relations described in the literature.[1] The Cr/a-SiO_2/Si sample was grown on an amorphous substrate and therefore has no epitaxy. A θ-2θ scan of the Cr/a-SiO_2/Si sample showed all three allowed bcc diffraction peaks, (002), (011), and (112), suggesting a polycrystalline film with no preferred orientation. The width of the peaks suggests an out-of-plane correlation length of 30 nm.

Top-down scanning electron microscopy (SEM), in Figure 4.1(a-b), shows that both the Cr/Al_2O_3 and the Cr/a-SiO_2/Si samples consist of elongated grains about 17nm by 50nm in size. The epitaxial Cr/MgO sample had no surface structure visible by SEM.

The sputtered series of samples was grown in an AJA magnetron sputtering system with a base pressure below 5×10^{-8} Torr. The gun was powered with 150W DC, and the films were deposited at rates of 0.5-1.0 Å/s onto substrates of amorphous SiN_x/Si held at room temperature. The Ar sputtering gas pressure was varied between 0.75 mTorr and 8 mTorr. In addition to this series, one sample was sputtered at 0.75 mTorr with the substrate held at 350 °C; this sample had larger grains and exhibited bulk-like behavior, including a clear ISDW, as shown in Chapter 3 [15], and this will be referred to as the "bulk-like" sample for the rest of the chapter.

The sputtering gas pressure plays an important role in the growth kinetics of sputtered films - low Ar pressure leads to high energy incident atoms, while high pressure leads to thermalization and lower incident energy. This results in high and low pressure sputtered films having drastically different morphologies. Cross-sectional transmission electron microscopy (TEM), in Figure 4.1(f-g), shows that both high and low pressure films have columnar structure. The low pressure films are flat and exhibit high tensile stress, while the high pressure films are very rough, have low tensile stress, and have wide grain boundaries which include some amorphous material. SEM, in Figure 4.1(c-d), shows that the grains are oblong and about 25nm by 35nm for the 0.75 mTorr film and 25nm by 50nm for the 8

---

[1]A ϕ scan of the 45° off-axis (001) peak in a single crystal (011) oriented film should yield two peaks. In the literature it is suggested that two types of orientation relationships occur in Cr growth on Al_2O_3 (0001): OR I with three orientations in plane (yielding six peaks) and OR II with six orientations in plane (yielding twelve peaks), 5.26° offset from ORI in either direction, for a total of nine orientation relationships and eighteen peaks in the azimuthal scan. However, the broad peaks observed in our diffraction pattern as well as in the literature cannot distinguish between ORI and ORII 5.26° apart so only six peaks are observed. See Section 2.2.2.1.2.

mTorr film. The correlation length from x-ray diffraction for the room temperature sputtered samples ranged from 18 to 28 nm, and was 35 nm for the bulk-like sample. More details of the growth and characterization of these sputtered samples are given in Chapters 2 and 3.[15]

The very high resistivity seen in some of these films is unusual and naturally raises the question of impurities in the film. To study this, we chose the most resistive sample, the 8 mTorr sputtered sample (392 $\mu\Omega$ cm at 5 K), and annealed it at a series of temperatures. A rapid thermal annealer (RTA) was used, with an Ar atmosphere, to anneal the sample at 400, 600, and 800 °C for 2 minutes each. A factor of 10 decrease in the resistivity with annealing at 800 °C suggests that the reason for the high resistivity is in fact crystal defects which can be removed by annealing rather than impurity atoms. SEM done on the annealed samples showed little change in grain structure with annealing to 400 and 600 °C but a significant change after annealing at 800 °C. The grains of the annealed sample are round as opposed to oblong and there are some large voids which may have been formed when smaller voids between grains coalesced during the annealing process (Figure 4.1(e)).

Energy dispersive x-ray spectroscopy (EDS) found no Ar, N, or C contamination in the films, within the margin of error of 0.25 at. % for Ar and N, and 1.0 at. % for C.[2] Total oxygen percentage was 2 at. % in the sputtered films grown at low pressure, and 4 at. % in the films grown at high pressure. Chromium is known to form a self-limiting oxide and these results are consistent with a surface oxide layer given that the films grown at high pressure were rough and had about twice the surface area to oxidize.

All films described here are approximately 200 nm, so that differences between films can be attributed to deposition conditions rather than thickness differences. Actual thickness, used to calculate resistivity, was measured with a KLA-Tencor Alpha-Step IQ profilometer or a KLA-Tencor Nanopics AFM with an uncertainty in thickness of approximately 2 %.

The films were patterned so the geometry was well defined. Resistivity was measured using a DC four-point probe method to avoid contact resistance effects.

4.3   Results

Resistivity as a function of temperature for the three series of samples is presented in Figs. 4.2 - 4.4. Each figure shows the resistivity of all samples in the series on one plot. Individual plots of the low temperature resistivity for each sample are also shown with a least-squares fit to the data described in Section 4.4.

The three main features to note in the resistivity are the residual resistivity (ρ_0), the minimum in the resistivity at low temperatures due to resonant impurity scattering, and the linear slope of the resistivity at moderate temperatures due to electron-phonon scattering. The most commonly studied feature in the resistivity of Cr is the Neel transition which occurs at $T_N = 310$ K in bulk Cr and ranges from 220 K to >400 K in our films.[15]

---

[2]An additional film was grown on a Si thermal oxide substrate so at. % N could be measured without observing a signal from the SiNx substrate. For at. % C, the EDS chamber had a background 5 at. % C signal which obscured the measurement; the margin of error for the at. % C measurement is therefore 1%.
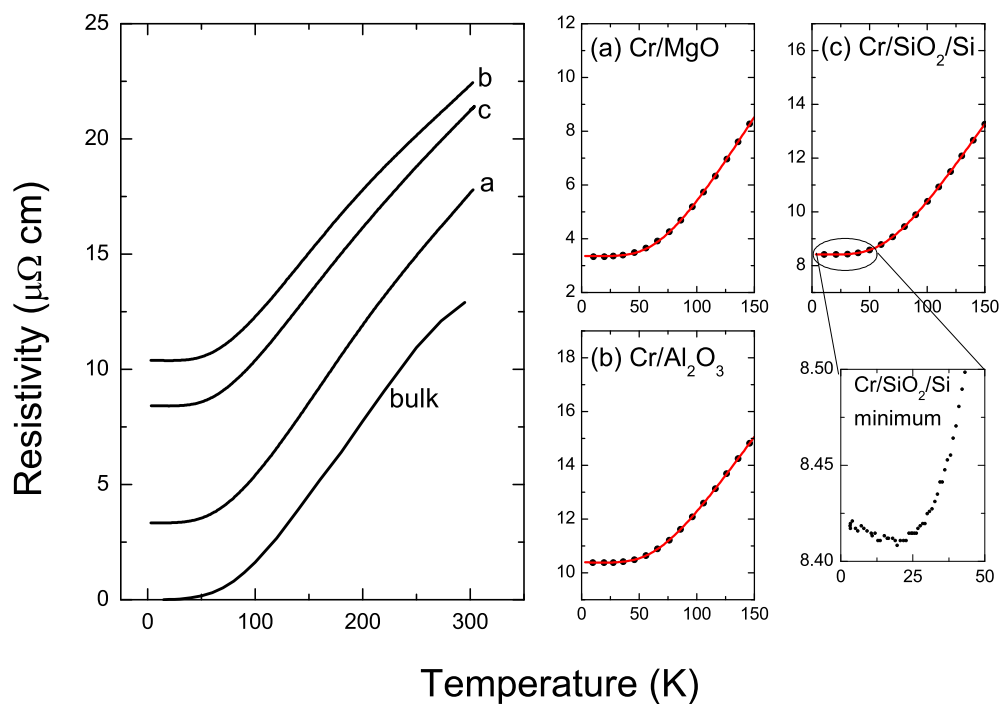
Figure 4.2: Resistivity as a function of temperature for e-beam deposited Cr films grown on 3 substrates with varying degrees of epitaxy: MgO (epitaxial single crystal), Al$_2$O$_3$ (textured polycrystalline), SiO$_2$/Si (untextured polycrystalline). Bulk data is from White and Woods.[130] In the close up panels, selected data points are shown with the least-squares fits to Equation 4.6.
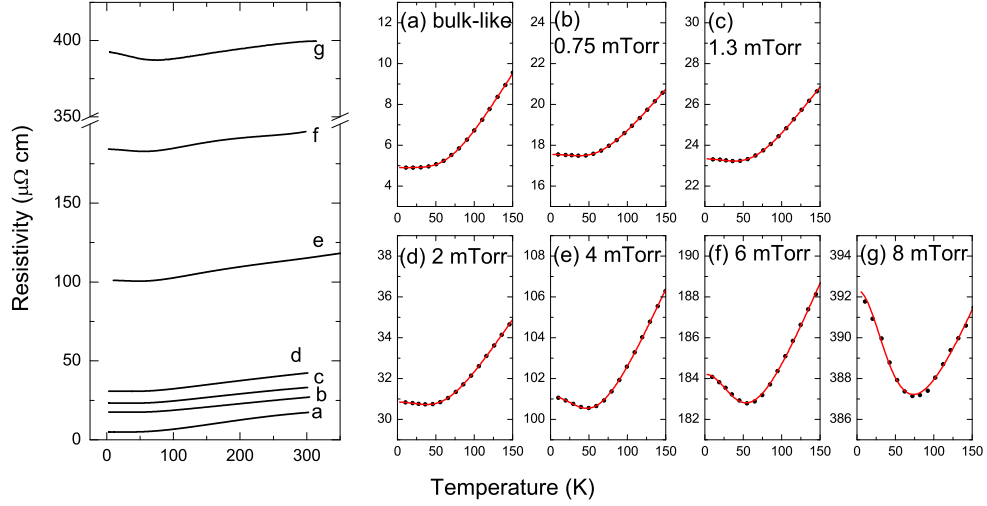
Figure 4.3: Resistivity as a function of temperature for unannealed sputtered films grown at different sputtering pressures. In the close up panels, selected data points are shown with the least-squares fits to Equation 4.6.

We will not discuss the Neel transition here, and instead focus on the resonant impurity scattering and electron-phonon scattering features at low and moderate temperatures.

The resistivity vs. temperature curves for the films in the e-beam deposited series are shown in Figure 4.2. In these films, all three resistivity features vary between samples. The residual resistivity is very low (3.4 $\mu\Omega$ cm) for the epitaxial film on MgO and increases for the polycrystalline samples, both the textured Cr/Al_2O_3 (10.4 $\mu\Omega$ cm) and untextured Cr/a-SiO_2/Si (8.4 $\mu\Omega$ cm). This is expected, as grain boundaries cause scattering. At low temperatures, a minimum in the resistivity is observed for all three samples; it is shown in a close-up of the low temperature data for the Cr/a-SiO_2/Si film in Figure 4.2. This minimum is due to resonant scattering from defects in the film. Finally, the slope of the resistivity at moderate temperatures also varies between samples; it is very close to bulk for the Cr/MgO sample and lower for the Cr/Al_2O_3 and Cr/a-SiO_2/Si samples. Both the resistivity minima and the difference in resistivity slope between samples are deviations from Matthiessen's rule which states that resistivity vs. temperature curves should be parallel for samples of the same material with different amounts of defects.[11]

The resistivity vs. temperature curves are shown in Figure 4.3 for the series of sputtered samples. The range of low temperature resistivities observed in these samples is significantly larger than in the previous series of samples, increasing from 4.9 to 392 $\mu\Omega$ cm with increasing sputtering pressure. The resonant scattering minimum increases drastically with sputtering pressure as well, with the depth of the minimum as large as 5 $\mu\Omega$ cm for the highest resistivity (8 mTorr) sample. One film, the 1.3 mTorr sample, was measured to as low as 0.6 K in order to investigate the low temperature limit of the resistivity minimum.
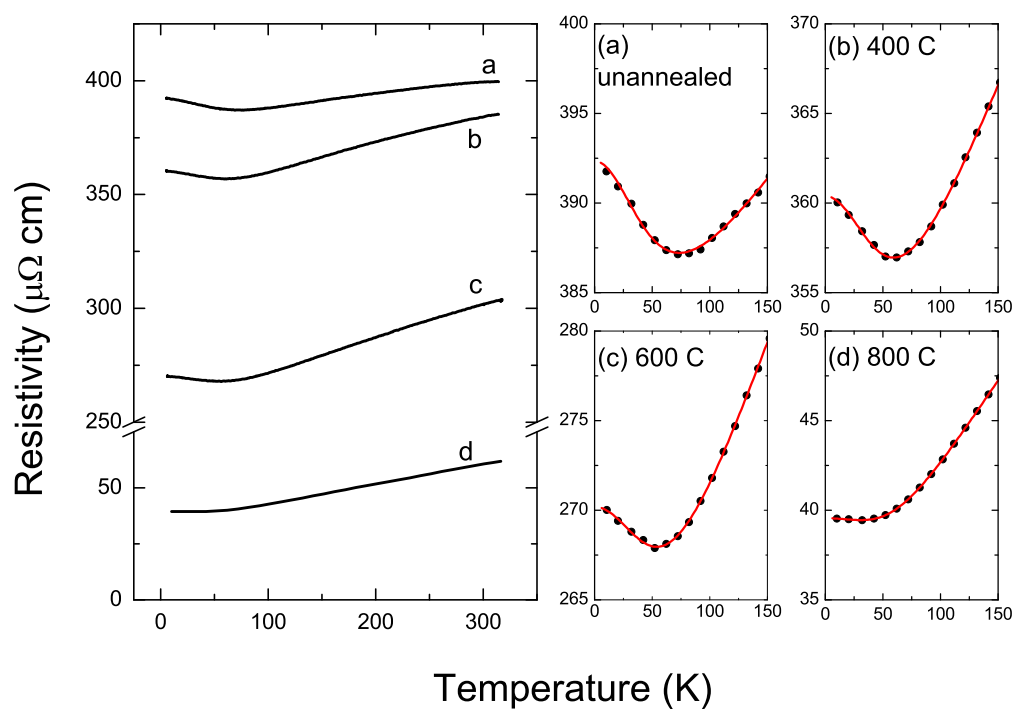
Figure 4.4: Resistivity as a function of temperature for a film sputtered at 8 mTorr and then annealed at a series of temperatures. In the close up panels, selected data points are shown with the least-squares fits to Equation 4.6.

It was found that the the increase in resistivity at low temperatures levels off as $T \to 0$. This excludes the possibility of insulating behavior being responsible for the minimum as that would cause the resistivity to increase infinitely upon approaching 0 K. The slope of the resistivity in these films varies as well, although the variation in slope is much smaller than the variation in the residual resistivity.

The film with resistivity of 392 $\mu\Omega$ cm at 5 K, the 8 mTorr sputtered film, was annealed at a series of temperatures. The resistivity vs. temperature profiles are shown in Figure 4.4. Both the residual resistivity and the magnitude of the resistivity minimum are decreased by annealing. The most dramatic effect is seen for the 800 °C annealed film, in which the low temperature resistivity decreases by a factor of 10, from 392 to 39 $\mu\Omega$ cm. This is a clear indication that both the high residual resistivity and the observed resistivity minima are primarily due to defects in the crystal which are eliminated by annealing. In this series, the slope of the resistivity also varies significantly, increasing in the 400 and 600 °C samples and then decreasing again in the 800 °C sample. The reasons for the nonmonotonic behavior of the slope are not obvious, and are left for the discussion in Section 4.5.

4.4   Model for the Resistivity

The resistivity of Cr can be written as a sum of multiple terms. Following the work of Chiu et al [19], we write:

$$\rho(T) = \rho^{res}(T) + \frac{\rho_0 + \rho_{e-p}(T) + \rho_m(T)}{1 - \alpha\Delta(T)/\Delta(0)}. \tag{4.1}$$

Here, $\rho^{res}(T)$ is the resistivity due to resonant impurity scattering, ρ_0 is the residual resistivity due to normal potential scattering, $\rho_{e-p}(T)$ is the resistivity due to electron-phonon scattering, and $\rho_m(T)$ is the resistivity due to magnetic fluctuations. The term $1 - \alpha\Delta(T)/\Delta(0)$ accounts for the decrease in the number of carriers at the Fermi surface below T_N due to the SDW gap. $\Delta(T)$ is the SDW gap, and α is the fraction of carriers at the Fermi surface that is destroyed by the SDW gap.

The films in this chapter are sufficiently thick (200nm) that they are considered 3-D systems. In addition, the thickness is significantly larger than the mean free path, so we do not take surface scattering into account. Electron-electron scattering is also not significant for our model.[3]

This equation can be simplified considerably by considering only temperatures well below T_N. The function $\Delta(T)$ has the form of a BCS gap; well below T_N, $1 - \alpha\Delta(T)/\Delta(0) \to 1 - \alpha$. The resistivity due to fluctuation scattering, ρ_m, contributes a maximum of 1.5 $\mu\Omega$ cm to the resistivity at T_N, and becomes negligible below about $0.5T_N$. For temperatures below $0.75T_N$, ρ_m is less then 5% of the phonon resistivity.[19] We will apply the fit from

---

[3]A T^2 term in the resistivity due to electron-electron scattering has never been quantified for Cr, however an estimate based on the isoelectronic element W finds the magnitude of the electron-electron scattering resistivity significantly less than the residual in the Bloch-Gruneisen fit at low temperatures (0.0006 $\mu\Omega$ cm at 15 K) and dwarfed by the electron-phonon scattering term at moderate to high temperatures (1% of the electron-phonon resistivity at 150 K).[26]

2-150 K, which is less than $0.5T_N$ for most samples and less than $0.75T_N$ for all samples, so that $\rho_m \to 0$.

Making these simplifications with the assumption that T is well below T_N, we are left with a resistivity that takes the following form:

$$\rho(T) = \rho^{res}(T) + \frac{\rho_0}{1-\alpha} + \frac{\rho_{e-p}(T)}{1-\alpha}. \tag{4.2}$$

α for bulk Cr is 0.3, and varies from 0.3 - 0.55 in Cr alloys.[19, 113] Because the SDW is known to vary between thin film samples grown under different deposition conditions, it is possible that α varies as well. Rather than assuming a numerical value for $1-\alpha$, we redefine ρ_0 and $\rho_{e-p}(T)$ to include the $1-\alpha$ term:

$$\rho(T) = \rho_0 + \rho^{res}(T) + \rho_{e-p}(T). \tag{4.3}$$

The temperature-dependent resonant term, $\rho^{res}(T)$, takes the following form[127]:

$$\rho^{res}(T) = \frac{\rho_0^{res}}{1 + (T/\Theta_{res})^2}, \tag{4.4}$$

where ρ_0^{res} is the magnitude of the resonant scattering minimum and Θ_{res} is a parameter related to the energy width of the localized states leading to resonant scattering and the energy difference between these states and the Fermi energy. The shape of this function is such that the resistivity varies as $-T^2$ at low temperatures, increasing as the temperature is decreased but leveling off as $T \to 0$.

The term $\rho_{e-p}(T)$ can be written as a Bloch-Gruneisen function, which is derived from the Debye model for phonons. This term goes as T^n at low temperatures and as T at moderate to high temperatures; the crossover between the two is related to the Debye temperature of the material.

$$\rho_{e-p}(T) = C_G \frac{T^n}{\Theta_G^{n+1}} \int_0^{\Theta_G/T} \frac{x^n}{(e^x - 1)(1 - e^{-x})} dx \tag{4.5}$$

Here, C_G is a constant and Θ_G is an effective Debye temperature.

For simple metals $n = 5$ due to phonon-mediated s-s intraband transitions. However, in the transition metals it is often seen that $n = 3$ because s-d interband transitions dominate. Generally, the $n = 5$ form of Equation 4.5 is known as the Bloch Gruneisen function, while the lesser known $n = 3$ form is attributed to Wilson.[87] In Cr, both s-s and s-d scattering occurs.

Least-squares fits applied to our data for the epitaxial Cr/MgO film, which has low residual resistivity of 3 $\mu\Omega$ cm and a negligible resistivity minimum (0.003 $\mu\Omega$ cm deep), show that the $n = 5$ form fits significantly better than $n = 3$ based on χ^2. A plot of the ideal resistivity of the epitaxial Cr/MgO sample (with ρ_0 subtracted) is given in Figure 4.5 with both the $n = 5$ and $n = 3$ forms of Equation 4.5. The residuals of both fits are shown as well. Although the fits of Equation 4.5 with $n = 5$ are very good, there is some noticeable systematic deviation at low temperatures. The actual resistivity of Cr/MgO at low temperatures increases more quickly than the fit with $n = 5$, but more slowly than

$n = 3$. The residuals of the two fits oppose each other, which implies that a fit of a linear combination of the two terms would be optimal. To avoid overparameterization, we chose to use only the dominant $n = 5$ (s-s scattering) to fit the remaining data sets. The maximum residual of the $n = 5$ fit is 0.04 $\mu\Omega$ cm, which we take as the minimum error in our fit parameters. The residuals of $n = 5$ and $n = 3$ fits to the bulk data from White and Woods[130] were very similar, suggesting that the epitaxial Cr/MgO sample is a good comparison to bulk.

Aside from the choice of n, there is another assumption made in using the Bloch-Gruneisen function: the Debye model. The Debye model assumes that the phonon dispersion relation $\omega(k)$ is linear, and the maximum phonon energy gives the Debye temperature Θ_D. In reality, $\omega(k)$ is not linear and has structure. This is often described within the Debye model by stating $\Theta_D(T)$ as a variable which depends on temperature.[32, 99] In Cr, the value for $\Theta_D(0)$ is quoted as 585 K[22, 54], while $\Theta_D(\infty)$ is quoted as 478 K.[32] The Bloch-Gruneisen function uses an average value for the Debye temperature; to avoid confusion we call this Θ_G. The effect of using an average value rather than a temperature-dependent $\Theta_D(T)$ should cause the fit resistivity to increase more quickly at low temperature. However, in Figure 4.5 it is clear that the fit increases more slowly than the data. Thus, the effect of using a temperature average of $\Theta_D(T)$ on the electron-phonon resistivity is smaller than the effect of s-d scattering.

With the assumption of dominant s-s scattering, Equation 4.2 can be written:

$$\rho(T) = \rho_0 + \frac{\rho_0^{res}}{1 + (T/\Theta_{res})^2} + C_G \frac{T^5}{\Theta_G^6} \int_0^{\Theta_G/T} \frac{x^5}{(e^x - 1)(1 - e^{-x})} dx. \qquad (4.6)$$

We applied a least-squares fit of Equation 4.6 to the resistivity data from 2-150 K. For the error bars on the fit parameters we used the error in the fit given by Origin 8 added in quadrature to the error in the fit to the Bloch-Gruneisen function due to s-d scattering (0.04 $\mu\Omega$ cm, the maximum residual to the fit shown in Figure 4.5). There is also a 2% overall uncertainty in $\rho(T)$ due to the thickness measurement which is not included in the error in the fit parameters. As might be expected for a 5 parameter fit, the error bars are large in some cases. In particular, for the samples with very slight minima, the parameters describing the minimum, ρ_0^{res} and Θ_{res} have large error bars. Likewise, the samples with very pronounced minima have large errors in the parameter Θ_G because the Bloch-Gruneisen behavior is obscured by the large minimum. However, the resulting fit closely matches the data for every sample, including bulk data.

4.5   Discussion
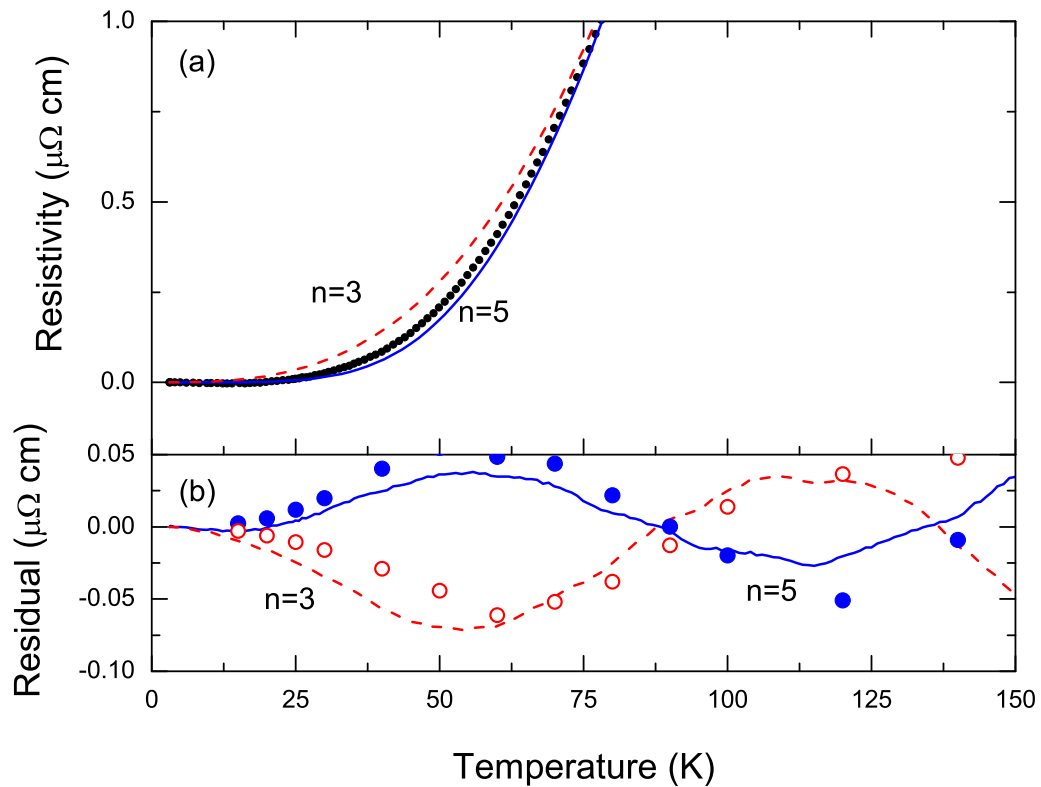
Figure 4.5: (a) The ideal resistivity of the epitaxial Cr/MgO sample (points), fit to the $n = 5$ and $n = 3$ forms Equation 4.5 (solid and dashed lines). The residual resistivity has been subtracted from the data so that only the electron-phonon term in the resistivity is fit resulting in two parameters, C_G and Θ_G. (b) Lines: The residuals of the n=5 (solid) and n=3 (dashed) fit for the Cr/MgO samples. Points: The residuals of the n=5 (solid) and n=3 (empty) fit for ideal bulk Cr resistivity from White and Woods.[130]

Sample	ρ_0 (μΩ cm)		ρ_0^{res} (μΩ cm)		Θ_{res} (K)		Θ_{B-G} (K)		$C_{B-G}/4\Theta_{B-G}^2$ (μΩ cm/K)	
Bulk ideal ρ [130]	-		-		-		519 ± 17		0.054 ± 0.004	
E-beam series	**Vary substrate**									
e-beam dep	3.4 ± 0.04		-		-		464 ± 11		0.055 ± 0.002	
onto 300 °C	10.4 ± 0.05		-		-		450 ± 5		0.0488 ± 0.0003	
substrates	8.4 ± 0.04		-		-		450 ± 3		0.0505 ± 0.0004	
Sputtered series	**Vary pressure**									
bulk-like^a	4.9 ± 0.04		-		-		468 ± 8		0.050 ± 0.001	
polycrystalline	16.9 ± 0.2		0.6 ± 0.2		86 ± 18		432 ± 7		0.037 ± 0.002	
sputtered onto	22.6 ± 0.2		0.7 ± 0.2		75 ± 12		429 ± 8		0.041 ± 0.002	
room temp	30.0 ± 0.2		0.8 ± 0.2		73 ± 12		420 ± 8		0.046 ± 0.003	
a-SiN$_x$	98.6 ± 0.6		2.5 ± 0.6		65 ± 11		407 ± 18		0.071 ± 0.010	
substrates	179.7 ± 1.4		4.5 ± 1.3		60 ± 11		384 ± 37		0.077 ± 0.026	
	381.6 ± 1.3		10.7 ± 1.3		57 ± 5		400 ± 44		0.080 ± 0.031	
Annealed series	**Vary anneal temp**									
8mTorr	381.6 ± 1.3		10.7 ± 1.3		57 ± 5		400 ± 44		0.080 ± 0.031	
sputtered	350.9 ± 1.4		9.5 ± 1.4		60 ± 6		408 ± 27		0.139 ± 0.029	
sample	262.6 ± 1.7		7.6 ± 1.7		64 ± 9		417 ± 25		0.153 ± 0.031	
annealed	39.2 ± 0.1		0.4 ± 0.1		40 ± 6		419 ± 5		0.079 ± 0.001	

^{a}sputtered at 0.75 mTorr onto a 350 °C substrate

Table 4.1: Table of parameters derived from a least-squares fit of each sample's resistivity to Equation 4.6, for the three sample series. ρ_0 - residual resistivity, ρ_0^{res} - magnitude of resonant resistivity minimum, Θ_{res} - resonant scattering energy parameter, Θ_G - Debye temperature, $C_G/4\Theta_G^2$ - linear resistivity slope (high temperature). There is an overall 2% uncertainty in $\rho(T)$ which is not shown in the table due to uncertainty in the thickness measurement.

The fit parameters for all three series of samples are tabulated in Table 4.1. The five fit parameters are: ρ_0, the residual resistivity; ρ_0^{res}, the magnitude of the resonant scattering minimum; Θ_{res}, the resonant scattering energy parameter; Θ_G, the Debye temperature; and $C_G/4\Theta_G^2$, the slope of the linear term in the electron-phonon resistivity. Also shown are the values of Θ_G and $C_G/4\Theta_G^2$ for bulk ideal ($\rho_0 = 0$) resistivity from White and Woods[130], obtained from a fit to only the electron-phonon term in the model.

We have chosen to present the Bloch-Gruneisen prefactor as $C_G/4\Theta_G^2$ because as $T \to \infty$,

$$\rho_{e-p}(T) \to \frac{C_G}{4\Theta_G^2}T. \tag{4.7}$$

Thus, $C_G/4\Theta_G^2 = d\rho/dT$ in the high temperature limit of the Bloch-Gruneisen function. This is a very good approximation for high temperatures ($T \gtrsim 1.5\Theta_G$). For moderate temperatures ($0.2\Theta_G \lesssim T \gtrsim 1.5\Theta_G$), where the resistivity appears linear in temperature, the slope of the Bloch-Gruneisen function actually deviates from $C_G/4\Theta_G^2$ by as much as 20%. Thus, the parameter $C_G/4\Theta_G^2$ obtained from a fit of the Bloch-Gruneisen function at low and moderate temperatures is the best way to compare high temperature resistivity slopes between samples with different Θ_G without necessitating measurement of the resistivity above $1.5\Theta_G$ (about 700 K) which would anneal the samples and alter their properties.

4.5.1 Residual resistivity ρ_0:

The behavior of ρ_0 in these samples is qualitatively logical, increasing with the presence of defects and grain boundaries. ρ_0 increases substantially with sputtering pressure, as seen in Figure 4.6, due to the morphology of wide grain boundaries with many defects observed in films grown at high pressure. There is a significant decrease in ρ_0 for films that are either annealed or grown epitaxially, which decreases the number of defects.

Quantitatively, the magnitude over which ρ_0 varies is anomalously large. Fe films grown under the same sputtering conditions, which have similar microstructure to Cr films due to the similar atomic masses and look similar in SEM images, have also been shown to have increasing ρ_0 with pressure, but the effect is significantly smaller. An 8 mTorr sputtered Fe film has ρ_0 of 42 $\mu\Omega$ cm, almost 10 times smaller than ρ_0 for the 8 mtorr Cr film.[29] The primary cause of the high resistivity in Cr films is resonant scattering from localized states within the SDW gap, a unique result of the itinerant antiferromagnetism.

Typical amorphous transition metal alloys have ρ_0 around 150 $\mu\Omega$ cm because they generally have about one carrier electron per atom and the mean free path is on the order of the interatomic spacing. Generally, the resistivity of alloys with ρ_0 lower than this increases with temperature (positive $d\rho/dT$). As ρ_0 approaches 150 $\mu\Omega$ cm, $d\rho/dT$ decreases, this behavior is called saturation and is thought to be due to the failure of the Boltzmann transport model when the mean free path is on the order of the interatomic spacing. Alloys with ρ_0 higher than this threshold tend to have a negative $d\rho/dT$, due to quantum backscattering.[88] This is not a steadfast rule, but a correlation (often called the Mooij correlation) which is observed in a wide range of alloys.
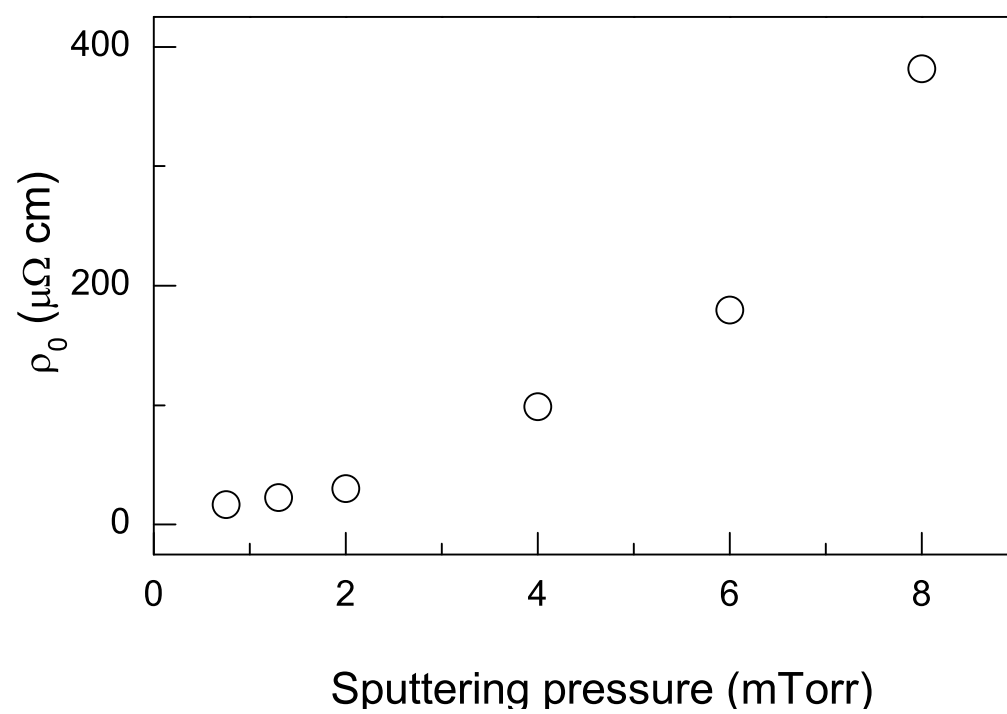
Figure 4.6: ρ_0 as a function of sputtering pressure, for the sputtered samples. Error bars are smaller than the symbol size.

Exceptions to this are "bad metals" which exhibit positive $d\rho/dT$ up to resistivities well beyond 150 $\mu\Omega$ cm, corresponding to mean free paths decreasing continuously through one interatomic spacing and lower, a non-physical result. Examples are the high T_c superconductors, and the colossal magnetoresistance manganates. Although the materials exhibiting bad metal behavior are often exotic, the same transport behavior can be produced in good metals if their geometry is constricted. This effect has been reported in thin silver films in the regime where silver islands begin to coalesce.[6] If only a few of the silver islands in a film are touching, the electrons must take a longer, tortuous path through the film, changing the effective length of the sample. When converting the measured resistance to resistivity, this results in a multiplicative factor (l_{eff}/l) in the resistivity. The signature of such a geometry effect is that $d\rho/dT$ increases proportionally with ρ_0.

The Cr 8 mTorr sample has $\rho_0 = 381.6$ $\mu\Omega$ cm, which assuming 0.25 holes per electron[42, 36], corresponds to a mean free path of about 4.3 Å. This is a very small mean free path for a film with a grain size of 280 Å, but is slightly larger than the lattice constant, so it is not truly a "bad metal". Still, this high resistivity could be partially explained by a geometry effect such as the one observed in the silver films. If some regions of the high pressure samples are not conducting (for example the "valleys" between columnar grains, some of the grain boundaries, or voids within the sample), this would constrict the path of the conduction electrons, introducing a multiplicative factor l_{eff}/l into the resistivity.

For our Cr films, the slope $C_G/4\Theta_G^2$ varies considerably between samples for reasons other than geometry (see Section 4.5.3) and therefore cannot be used as a test for the geometry factor l_{eff}/l in the same way. An Fe film sputtered at 8 mTorr, under the same conditions showed a geometric factor l_{eff}/l of about 3 in the resistivity based on a $3\times$ increased resistivity slope, while a 2 mTorr film showed no geometry enhancement. The factor l_{eff}/l should be similar for these films due to the similar microstructure; therefore we attribute to the Cr 8 mTorr film a factor l_{eff}/l of 3, and an unknown geometry factor between 1 and 3 for the 4 and 6 mTorr samples. This leaves an intrinsic resistivity of 130 $\mu\Omega$ cm and a slope $(C_G/4\Theta_G^2)$ of 0.27 $\mu\Omega$ cm/K for our 8 mTorr Cr film. These are plausible values for ρ_0 within the Mooij correlation and for $C_G/4\Theta_G^2$ within the range of our data on other polycrystalline films, however a ρ_0 of 130 $\mu\Omega$ cm, which corresponds to a 12.9 Å mean free path, is still unusually high.

Resonant scattering, which causes the resistivity minimum, also causes very high residual resistivity. Theoretically, the resistivity due to resonant scattering is entirely accounted for by the expression for $\rho^{res}(T)$ shown in Equation 4.4, while ρ_0 represents non-resonant scattering. Based on our fit for the 8 mTorr sample, for example, the resonant scattering term accounts for about 10 $\mu\Omega$ cm of the total resistivity at 2 K, while the non-resonant part ρ_0 accounts for the other 382 $\mu\Omega$ cm. In practice, the residual resistivity in resonant scattering systems is generally much higher than would be expected based on the form of $\rho^{res}(T)$. For the prototypical incommensurate resonant scattering system, $Cr_{0.985-x}Fe_{0.015}V_x$, ρ_0 is about 12 $\mu\Omega$ cm. The magnitude of the resistivity minima due to resonant scattering varies between samples, but a typical value is about 0.3 $\mu\Omega$ cm. Assuming that ρ_0 and the depth of the resonant scattering minimum scale linearly with the number of resonant scatterers, an approximately 10 $\mu\Omega$ cm resistivity minimum such as is seen in the 8 mTorr sample would correspond to a residual resistivity of about 400 $\mu\Omega$ cm,
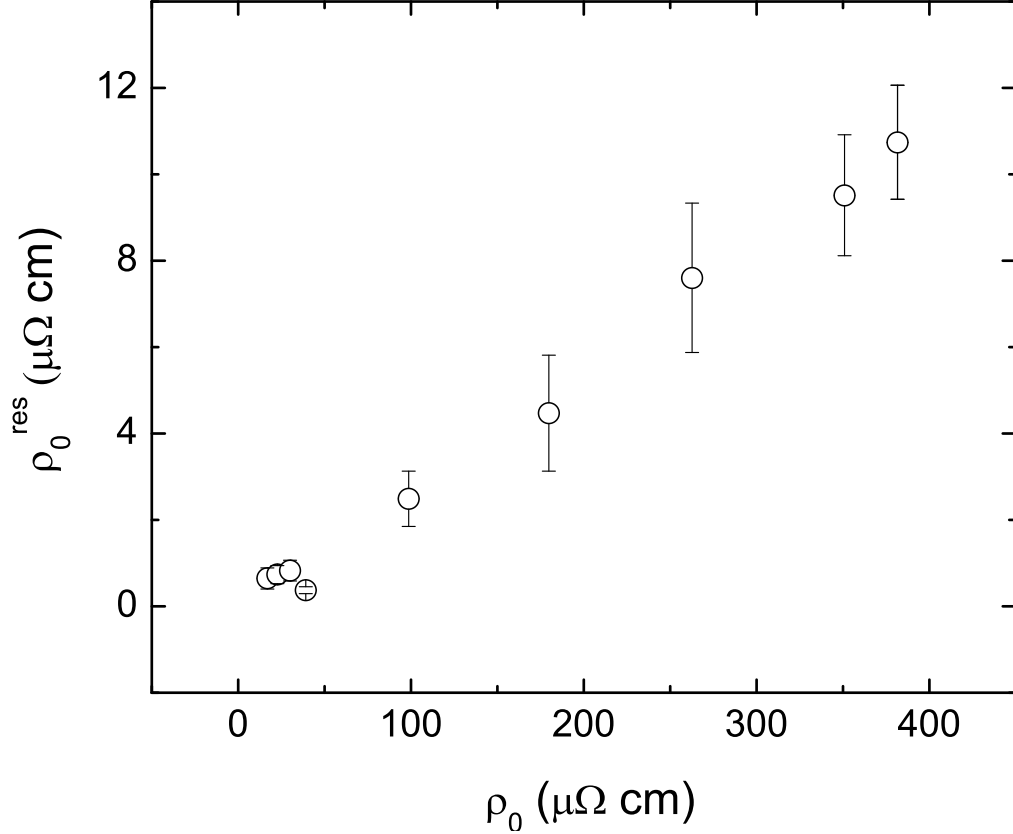
Figure 4.7: Linear correlation between the magnitude of the resonant scattering resistivity minimum ρ_0^{res} and the residual resistivity ρ_0.

approximately what we observe. Thus, the very high residual resistivity seen in our samples is consistent with resonant scattering.

A linear correlation between the magnitude of the resonant scattering minimum ρ_0^{res} and ρ_0 in our samples is shown in Figure 4.7. Such a correlation is not surprising, but the range over which it persists is. In the literature resonant scattering is typically studied by keeping the number of scatterers constant (ex. Fe 1.5 at. % for incommensurate or 2.7 at. % for commensurate) while varying the Fermi level (x at. % Mn or V). As such, little data exists on the concentration dependence of the resonant scattering minimum. Our results show a linear correlation between ρ_0^{res} and ρ_0 which is maintained over two orders of magnitude.

4.5.2 Resonant impurity scattering minimum (ρ_0^{res} and Θ_{res}):

Two samples, the e-beam deposited epitaxial Cr/MgO and sputtered "bulk-like" Cr, had negligible low temperature minima (less than 0.005 $\mu\Omega$ cm) and the resonant scattering term in the 5-parameter fit did not converge, so the parameters listed in Table 4.1 are those for a 3-parameter fit of ρ_0 plus electron-phonon scattering. Two samples, the e-beam deposited textured polycrystalline Cr/Al$_2$O$_3$ sample and untextured polycrystalline Cr/a-SiO$_2$/Si, have minima which were fit to the 5-parameter model but the size of the minima given by the parameter ρ_0^{res} are within the error of the fit. Therefore, for these two samples both fit parameters of the resonant term must be considered statistically insignificant within this model.

In the theory of resonant impurity scattering, the energies of the localized states within the gap depend on the type of impurity as well as the type of SDW in the Cr matrix. In the case of a commensurate SDW, a small concentration of an impurity ion is expected to lead to two localized states within the SDW, symmetric about the middle of the gap. In the case of an incommensurate SDW there is expected to be a continuum of localized energy levels within the gap with some structure to it which causes the resonance.[47] In samples known to be commensurate, tuning the Fermi energy (through Mn or V doping) leads to a peak in the residual resistivity when the Fermi energy falls at the energy of one of the localized states. In addition, commensurate samples not only show the expected resistivity minimum at low temperatures, but sometimes also exhibit a resistivity maximum at even lower temperatures. This maximum is due to the fact that the energies of the localized states within the gap also have a temperature dependence.[46] Incommensurate samples do not show such a maximum; because the energy levels are spread out within the gap, a small temperature dependence of the energy levels does not have a significant effect.

The resistivity behavior in our Cr thin films suggests localized states that are spread out within the gap. Although our samples are known from Chapter 3 to have varied SDW states (commensurate, incommensurate, and mixed)[15], no maxima are observed in the low temperature resistivity. In addition, the variation of both ρ_0^{res} and ρ_0 within each series of films is monotonic. If the states occurred at only two energies within the gap, varying a parameter such as sputtering pressure (which varies the strain within the sample, which in turn varies the Fermi energy) should lead to a peak in ρ_0^{res} and ρ_0 when the Fermi energy is tuned to the localized state. However, it is possible that such a peak would not be observable amidst the very strong dependence of ρ_0^{res} and ρ_0 on the number of defects in the films. One way to explain the states being spread out inside the gap is that the defects leading to localized states can take many forms. For example, single vacancies, interstitials, vacancy clusters, dislocations, and multiple types of grain boundaries. Along a single grain boundary, even, each atom experiences a different potential due to its position. This distribution of defects and potentials would lead to multiple different sets of energy levels, resulting in a distribution of localized states within the SDW gap even for samples with a commensurate SDW.

Resonant scattering states should be observable in the specific heat as an increase in the density of states at the Fermi energy $N(E_F)$. Specific heat measurements of sputtered Cr films showed that $N(E_F)$ increases for the high sputtering pressure samples.[22, 102] This can be explained by disorder broadening, because the Fermi energy of Cr lies at a

minimum in the density of states. If the broadened states fall inside the SDW gap, they will become localized, according to theory.[127] The observed $N(E_F)$ for high sputtering pressure samples is higher than not only bulk antiferromagnetic Cr, but also paramagnetic Cr, which has about 50% higher $N(E_F)$ than antiferromagnetic Cr due to the disappearance of the SDW gap. If the increase in $N(E_F)$ for the sputtered samples were due to simple band broadening due to disorder, this would obliterate the SDW gap and cause the films to be paramagnetic. However, infrared reflectivity measurements have shown that the SDW still exists in these films. This suggests that rather than simple band broadening which would completely erase the SDW gap, the band broadening is more complicated: states are shifted to the SDW gap from above and below and are localized, while the SDW is maintained.

Besides resonant scattering, other possible explanations for a minimum in the resistivity are insulating grain boundaries or the Kondo effect. Insulating grain boundaries would lead to an exponential temperature dependence of the resistivity at low temperatures, which we do not observe. The Kondo effect, however, leads to a $-T^2$ temperature dependence of the resistivity at low temperatures, the same as for resonant scattering. In antiferromagnetic Cr with impurities, low temperature minima have been explained by resonant impurity scattering, and are not believed to be due to the Kondo effect for multiple reasons. First, resistivity minima have been seen in systems for which the impurity atom is known to be non-magnetic in Cr, and second, the SDW should suppress the spin-flip scattering of conduction electrons which is responsible for the Kondo effect. In paramagnetic Cr samples (> 3 at. % V) with magnetic impurities, resistivity minima have been observed and are thought to be due to the Kondo effect.[46] Our resistivity analysis cannot distinguish between resonant scattering and the Kondo effect, however based on the known antiferromagnetism in our films[15] and the large density of states at the Fermi energy observed in the specific heat study[22], resonant impurity scattering is the most likely explanation.

The parameter Θ_{res} is related to both the energy width of the localized state within the SDW gap which causes resonant scattering and the difference in energy between these states and the Fermi level. We find Θ_{res} to be similar for all films with a slight decreasing trend with ρ_0. The similar values for all films implies similar scattering centers in these films. The differences between films are primarily due to the *number* of scatterers rather than the type. Furthermore, the linear relation between ρ_0^{res} and ρ_0, discussed in Section 4.5.1 and shown in Figure 4.7, also supports the idea that the observed differences in resonant scattering between films are primarily due to the number of scatterers and not the type.

The 8 mTorr, 800 °C annealed sample has a significantly lower value for Θ_{res} than the others. This signifies a difference in the type of defects contributing to scattering in the 800 °C sample. The residual resistivity of this film is still somewhat high and must be due to defects which are not removed by annealing at 800 °C or, possibly, impurities incorporated during the annealing process. Thus, the localized scattering state within the SDW gap should be different as well, leading to a different Θ_{res}.
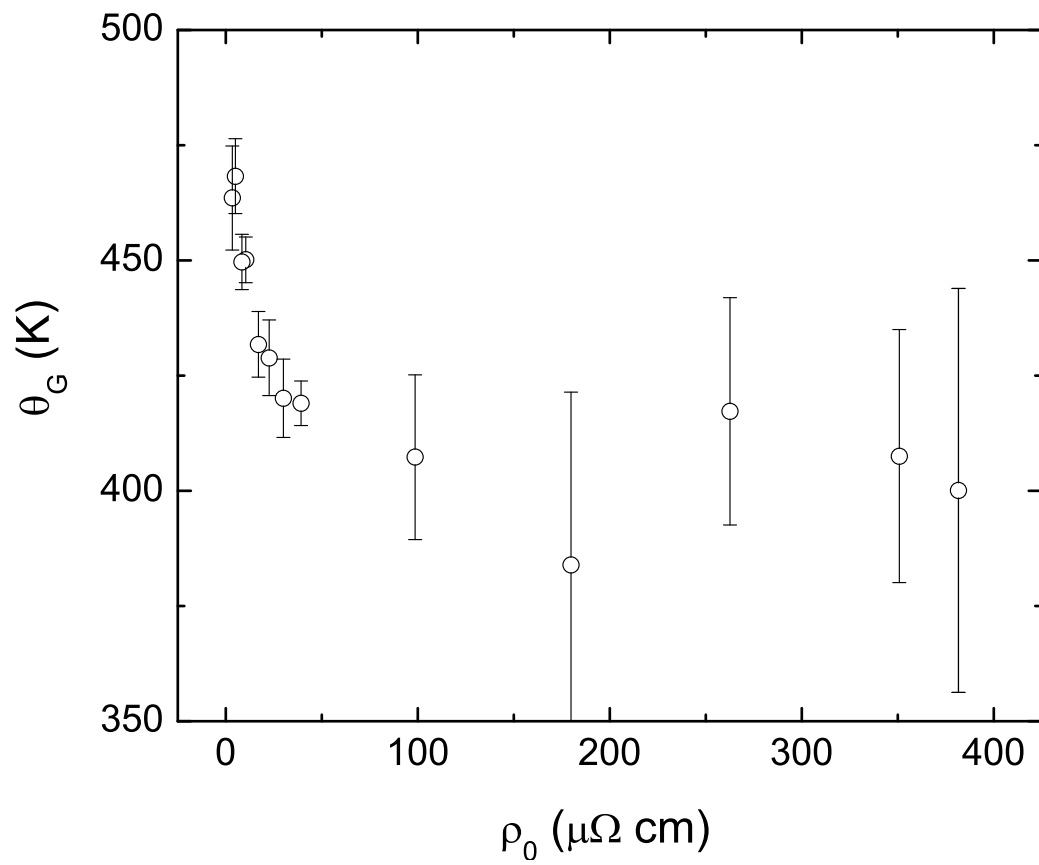
Figure 4.8: Correlation between the effective Debye temperature Θ_G and the residual resistivity ρ_0.

4.5.3 Electron phonon scattering (Θ_G and $C_G/4\Theta_G^2$):

The fit parameters of the Bloch-Gruneisen function can elucidate the nature of electron-phonon interaction in the Cr films. The effective Debye temperature, Θ_G, for bulk Cr, obtained from the Bloch-Gruneisen model, is 519 K, while the values observed in the films vary between 384 and 468 K. This is a significant decrease from bulk, which can be explained by "phonon softening" - a change in the phonon density of states which effectively decreases the average phonon energy at each temperature. Phonon softening in sputtered Cr thin films has also been observed in specific heat measurements.[22, 102] The value of Θ_G in these Cr films correlates well to ρ_0, suggesting that the phonon softening can be attributed to disorder. In Figure 4.8, we present a plot of Θ_G vs. ρ_0. Θ_G rapidly decreases upon initially adding defects. As more defects are added to the system, the effect of each defect on Θ_G declines, suggesting that the majority of phonon softening occurs at a relatively low threshold for disorder.

$C_G/4\Theta_G^2$ is equivalent to the high temperature slope $d\rho/dT$ of the Bloch-Gruneisen function, which by Matthiessen's rule is expected to remain constant between different samples of the same material with different concentrations of impurities and defects. In reality, many factors contribute to $d\rho/dT$ and can vary between samples. Table 4.1 shows $C_G/4\Theta_G^2$ for all samples varying between 0.037 and 0.153 $\mu\Omega$ cm/K, with no clear correlation to ρ_0 or any other variable.

The slope $d\rho/dT$ can be directly related to the transport electron-phonon coupling constant λ_{tr}:

$$d\rho/dT = \frac{2\pi m k_B}{ne^2\hbar}\lambda_{tr}. \tag{4.8}$$

The transport electron-phonon coupling constant differs from the specific heat electron-phonon coupling constant λ by an angular factor (the integral of 1-cosθ) which is close to 1. Thus, $d\rho/dT$ is often used as a measure of the electron-phonon coupling constant.[50]

Specific heat studies of the sputtered Cr films showed an increase in both $N(E_F)$ and λ for high pressure sputtered samples (4 and 8 mTorr). An increase in λ should show up in the resistivity as an increase in $d\rho/dT$. However, an increase in $N(E_F)$ could compensate for an increase in λ if the additional states are charge carriers contributing to n. As discussed previously, additional states that occur at k values inside the SDW gap become localized and cause resonant scattering. Additional states outside the SDW gap are not localized, and therefore can contribute to conduction. Assuming that all the additional states outside the SDW gap contribute to conduction, and assuming α, the fraction of the Fermi surface destroyed by the SDW, is 0.3, then using the values for λ calculated from the specific heat experiments[22] for the 8 mTorr sample $d\rho/dT$ would increase by a factor of 1.25 and for the 4 mTorr sample $d\rho/dT$ would increase by a factor of 1.10.

These values for the increase in $d\rho/dT$ due to the increased λ are lower limits. First, α may vary from the bulk value of 0.3; for Cr alloys it ranges from about 0.3-0.55. A larger α would increase the number of additional states in $N(E_F)$ which are localized and therefore do not contribute to conduction, decreasing the amount by which $N(E_F)$ contributes to an increase to n, compensating for the increase in λ. Or, if some of the additional states outside the SDW gap do not contribute very much to conduction, for example if they are more d-like than s-like, this would also decrease the amount by which

$N(E_F)$ contributes to an increase in n. In either case, the increase in $d\rho/dT$ would be larger than the estimates above.

Besides λ and $N(E_F)$, we will show that there are other factors which affect the resistivity slope, and therefore $d\rho/dT$ cannot be used as an independent measure of λ_{tr} for these samples.

First, Equation 4.8 for $d\rho/dT$ refers to the intrinsic resistivity. For the high pressure sputtered films, the geometry effect discussed in Section 4.5.1 increases the measured (extrinsic) resistivity by a factor of l_{eff}/l from the intrinsic resistivity. For the 8 mTorr sample, l_{eff}/l is taken to be 3 based on results for Fe films. For the 4 and 6 mTorr films, l_{eff}/l is expected to be somewhere between 1 and 3.

Secondly, we experimentally observe an effect which decreases $d\rho/dT$ for samples containing grain boundaries. The e-beam deposited series of samples can elucidate the role of grain boundaries in $C_G/4\Theta_G^2$. The epitaxial Cr/MgO sample has very good single crystal epitaxy by RHEED and XRD, and this is the sample which has $C_G/4\Theta_G^2$ closest to that of bulk Cr. As grain boundaries are introduced, in the Cr/Al$_2$O$_3$ and Cr/a-SiO$_2$/Si films, the slope is decreased somewhat, suggesting that grain boundaries cause a decrease in $C_G/4\Theta_G^2$ from the bulk value.

In the sputtered series of samples, $C_G/4\Theta_G^2$ for the low pressure films is also below the bulk value. The "bulk-like" sample, which has larger grains due to the elevated growth temperature, has the value closest to bulk. $C_G/4\Theta_G^2$ is only higher than bulk for the high pressure 4, 6, and 8 mTorr films which are known or suspected to have a geometry factor l_{eff}/l enhancing the measured $d\rho/dT$ above its intrinsic value. For the 8 mTorr film, taking l_{eff}/l into account, the intrinsic $d\rho/dT$ is 0.028 $\mu\Omega$ cm/K, even lower than that of the low pressure films. The physical mechanism for this decrease in slope with grain boundaries is not understood at this time.

For the annealed films, $C_G/4\Theta_G^2$ behaves nonmonotonically with annealing temperature. In the as-grown state, this sample, prepared at high pressure (8 mTorr) has a slope above bulk. Annealing to 400 and 600 °C increases the slope significantly, by about a factor of 2. Upon annealing to 800 °C, however, the residual resistivity is significantly decreased, and the slope is reduced. This nonmonotonic behavior is likely due to competition between various effects on the slope. As the film is annealed, the geometry factor l_{eff}/l likely decreases due to grain growth and healing of defects, effectively reducing the measured $d\rho/dT$. At the same time, grain growth should reduce the effect of the grain boundary effect discussed above, which should increase $d\rho/dT$.

The magnitudes of the various effects on $d\rho/dT$ can only be estimated after making serious assumptions about the nature of the additional states in $N(E_F)$, the fraction of the Fermi surface destroyed by the spin density wave (α), and the geometry factor l_{eff}/l. Because the physical mechanism behind the decrease in $d\rho/dT$ due to grain boundaries is not understood, its magnitude cannot be accounted for. The multiple competing effects make it impossible to extract the individual components of $d\rho/dT$ and calculate λ_{tr}.

4.6 Conclusion

We have shown the temperature-dependent resistivities of epitaxial and polycrystalline Cr thin films and fit the data to a model which includes electron-phonon scattering and resonant impurity scattering. The resistivity of Cr thin films is decidedly more complex than the parallel curves expected from Matthiessen's rule, which assumes that defects simply add a temperature-independent term to the resistivity. We observe multiple temperature-dependent effects due to defects in our films.

Localized defect states within the SDW gap lead to resonant scattering in Cr films, causing a very large residual resistivity in some samples and a resistivity minimum at low temperatures. The magnitude of the minimum, ρ_0^{res}, is proportional to ρ_0 over two orders of magnitude, suggesting that most of the contribution to ρ_0 is due to resonant scattering. In addition, the resonant scattering energy parameter Θ_{res} is similar for films grown under varying conditions, suggesting that the type of localized state formed by defects is similar for all films. This is the first experimental evidence of resonant impurity scattering due to defects in pure Cr rather than dopant atoms.

Defects also lead to changes in the electron-phonon resistivity, causing the effective Debye temperature Θ_G to decrease due to phonon softening. The slope of the resistivity in the linear regime varies between samples due a combination of extrinsic geometry, grain boundaries, and changes in the electron-phonon coupling and number of electrons at the Fermi energy.

4.7 Addendum

This chapter concluded that resonant scattering was observed in the resistivity of Cr thin films due to defects in pure Cr rather than dopant or contaminant atoms. However, later results found that some oxygen contamination (6-12 at. %) in fact occurred for the most resistive films (Cr sputtered at Ar pressures of 4-8 mTorr), as shown in Table 2.5. The majority of the films considered in this chapter had no detectable oxygen. The results of the annealing study, which showed a significant ($10\times$) decrease in the resistivity of the Cr 8 mTorr sample with annealing, are still valid, as the oxygen remained in the film after annealing.

It is most likely that the observed phenomena for the most resistive films is actually due to a combination of scattering from defects, as described in the chapter, and contaminant (oxygen) atoms. The resistivity decrease achieved by annealing the 8 mTorr film (from $382 \rightarrow 39$ $\mu\Omega$-cm) is quite significant, however a residual resistivity of 39 $\mu\Omega$-cm is still relatively high and is likely due to the O contamination. This is reasonable when compared with the results of older studies, which showed the effect of contamination on the resistivity of Cr films (Cr films containing up to 50 at. % impurity atoms had resistivity around 70 $\mu\Omega$-cm).[49]

The uncertainty surrounding the relative role of defects and oxygen contamination in this chapter should motivate further experiments using other, more controlled, methods to introduce defects into Cr, such as ion bombardment.

Chapter 5

Band gap and electronic structure of an epitaxial, semiconducting $Cr_{0.80}Al_{0.20}$ thin film

5.1 Introduction

Intermetallic compounds containing transition metals and *sp* elements often form a gap at the Fermi energy (E_F) due to hybridization. This gap can be exploited for applications, making these compounds the subject of intense study. For example, intermetallic semiconductors are attractive for thermoelectric devices due to their typically small gaps and large Seebeck coefficients (e.g. ZrNiSn).[125] In magnetic compounds, the gap is asymmetric with spin; if a gap occurs at E_F for one spin but not the other, the result is a half metal (e.g. Co_2MnAl).[75] Half-metals are important for spintronics circuits such as spin transistors and non-volatile logic.

Compounds of the form A_2BD or A_3D, where A and B are transition metals and D is an *sp* element, typically crystallize in the ternary ($L2_1$) or binary ($D0_3$) full-Heusler structures. These compounds are usually ferro- or ferrimagnetic, with the magnetic moment well predicted by a Slater-Pauling counting scheme: $M = Z - 24$, where Z is the total number of valence electrons in the unit cell.[43] For $Z = 24$, there is no net magnetization and a gap in both the majority and minority spin density of states (DOS), resulting in a semiconducting gap (e.g. pseudogap in Fe_2VAl).[90] This tunability and predictability of parameters with Z makes Heusler compounds an attractive class of materials to work with.

Cr_3Al ($Cr_{1-x}Al_x$ with $x \approx 0.25$) is an exception to this scheme. According to the Slater-Pauling counting scheme $Z = 21$ so it should be a metal with $M = -3$. Instead, $Cr_{1-x}Al_x$ is found to be antiferromagnetic for $x = 0$ - 0.50. Cr is an antiferromagnet with a spin-density wave (SDW) incommensurate with the lattice. The addition of Al causes the SDW to become commensurate, i.e. a simple antiferromagnetic structure, for $x \geq 0.03$. For $x = 0.15 - 0.26$, the Cr magnetic moment reaches $1\mu_B$ with a high Néel temperature of about 800 K.[31]

In the same range of x, $Cr_{1-x}Al_x$ displays semiconducting behavior not yet adequately explained by theory.[3] The gap has been estimated to be between 6 and 60 meV,
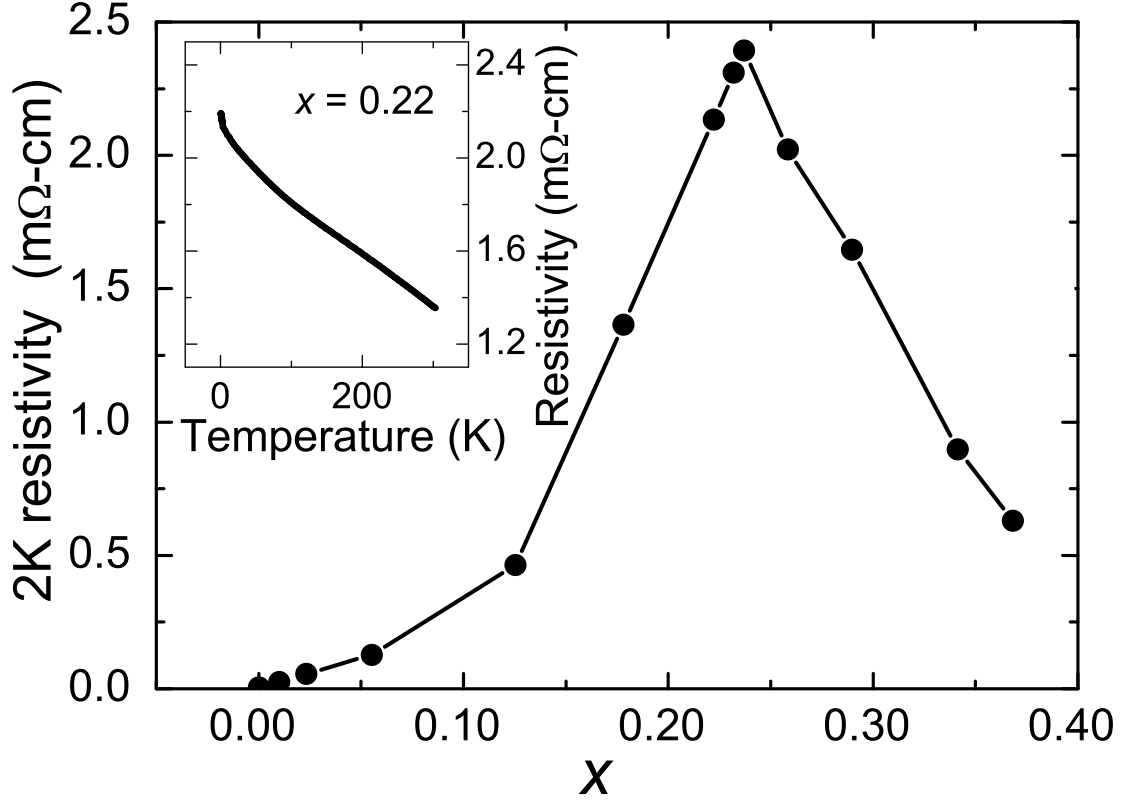
Figure 5.1: ρ vs x for $Cr_{1-x}Al_x$ thin films at 2K. Inset: $\rho(T)$ for $Cr_{0.78}Al_{0.22}$. Error bars smaller than symbols.

making $Cr_{1-x}Al_x$ a narrow-gap semiconductor.[83, 18, 91]

In this chapter, we probe the electronic structure of $Cr_{0.80}Al_{0.20}$ through hard x-ray photoemission spectroscopy (HXPS) and density functional theory (DFT). Hard x-rays are advantageous over soft x-rays due to enhanced bulk-sensitivity and relatively enhanced photoionization cross section of s electrons.[69, 68]

5.2 Methods

HXPS was done on an epitaxial $Cr_{0.80}Al_{0.20}$ thin film and a pure Cr reference film. The concentration $x = 0.20$ was chosen due to its high resistivity (ρ). $\rho(2K)$ vs. x is shown in Fig. 5.1 for a series of approximately 400Å $Cr_{1-x}Al_x(001)/MgO(001)$ films. The inset shows $\rho(T)$ for a $Cr_{0.78}Al_{0.22}(001)/MgO(001)$ thin film, grown in the same batch as the sample used for HXPS.

The $Cr_{0.80}Al_{0.20}(001)$ sample was a 429Å film, grown epitaxially on a 300°C MgO(001) substrate by co-deposition of Cr from an e-beam source and Al from an effusion cell at a rate of 0.4 Å/s and a base pressure of 5×10^{-9} Torr. Epitaxy was verified

in-situ by reflection high energy electron diffraction (RHEED) which showed a streaky pattern and ex-situ by x-ray diffraction (XRD) which showed only the bcc (001) orientation in a $\theta - 2\theta$ scan and four-fold symmetry of the (011) peak in an azimuthal scan at $45°$ from normal. The Cr sample was a sputtered, polycrystalline 2280Å film grown on SiO_2-coated Si at $350°$C with an Ar sputtering gas pressure of 0.75 mTorr. The SDW in Cr thin films is very sensitive to deposition conditions and these conditions yield bulk-like behavior in both the resistivity and SDW state.[15]

$Cr_{1-x}Al_x$ crystallizes on a bcc sublattice like the Heusler alloys, but D0$_3$ ordering has never been observed.[89] XRD suggests a random substitution of Al on the Cr lattice sites for $Cr_{1-x}Al_x$ in the range $x = 0 - 0.26$ ($x = 0 - 0.35$ for thin films) but a previous TEM study suggested that some non-D0$_3$ chemical ordering may occur for $Cr_{0.75}Al_{0.25}$, which should be studied further.[24]

DFT calculations were done for Cr and a $Cr_{0.80}Al_{0.20}$ alloy using the AkaiKKR code, a full-potential DFT Green's function approach based on the Korringa-Kohn-Rostoker multiple-scattering technique.[2, 71, 70] The scalar relativistic approximation was used and disorder in the alloy was treated using the coherent potential approximation (CPA).[112, 1] The number of irreducible k points used for Brillouin zone integration was 3276. The generalized gradient approximation (GGA) was used to approximate the exchange-correlation energy[94], which results in equilibrium lattice constants very close to experiment (Cr: 2.882Å calculated, 2.885Å experiment; $Cr_{0.80}Al_{0.20}$: 2.935Å calculated, 2.938Å experiment[18]). The commensurate SDW was used for both $Cr_{0.80}Al_{0.20}$ and Cr. The incommensurate SDW in Cr not only requires a computationally difficult large unit cell but is, as of yet, not found to be the minimum energy state in current DFT calculations.[53]

HXPS measurements were done at the undulator beamline BL15XU of SPring-8 with a fixed photon energy of 5956.4 eV. A VG Scienta R4000 hemispherical analyzer measured the kinetic energy of photoemitted electrons (PE electrons). Total energy resolution was 0.235 eV. A survey spectrum over an 800 eV binding energy range is shown in Fig. 5.2(a).

Hard x-rays create high energy PE electrons which have relatively long mean free paths (MFPs). The inelastic MFP is calculated from the TPP-2M formula[120]: 72Å (Cr) and 78Å ($Cr_{0.80}Al_{0.20}$) for valence band (VB) PE electrons with 5956.4 eV kinetic energy. Cr and Al both form self-limiting surface oxides making bulk sensitivity expecially important. The thickness of the surface oxide and residual adsorbent layers was modeled using the SESSA simulation package[108] and the relative intensities of the contaminant and sample core level peaks. Assuming an adsorbent CO layer and an oxide layer (Cr_2O_3 on Cr and Al_2O_3 on $Cr_{0.80}Al_{0.20}$) the simulation gives CO thicknesses of 4.95Å and 3.85Å and oxide thicknesses of 1.51Å and 2.15Å respectively. The thickness of the surface layers is small compared to the PE electron inelastic MFPs, showing that the measurement probes the bulk electronic structure of the samples.

5.3   Results

Figure 5.2(b) and (c) show the Cr 3s spectral region which displays multiplet splitting due to different binding energies of photoelectrons which are parallel and anti-
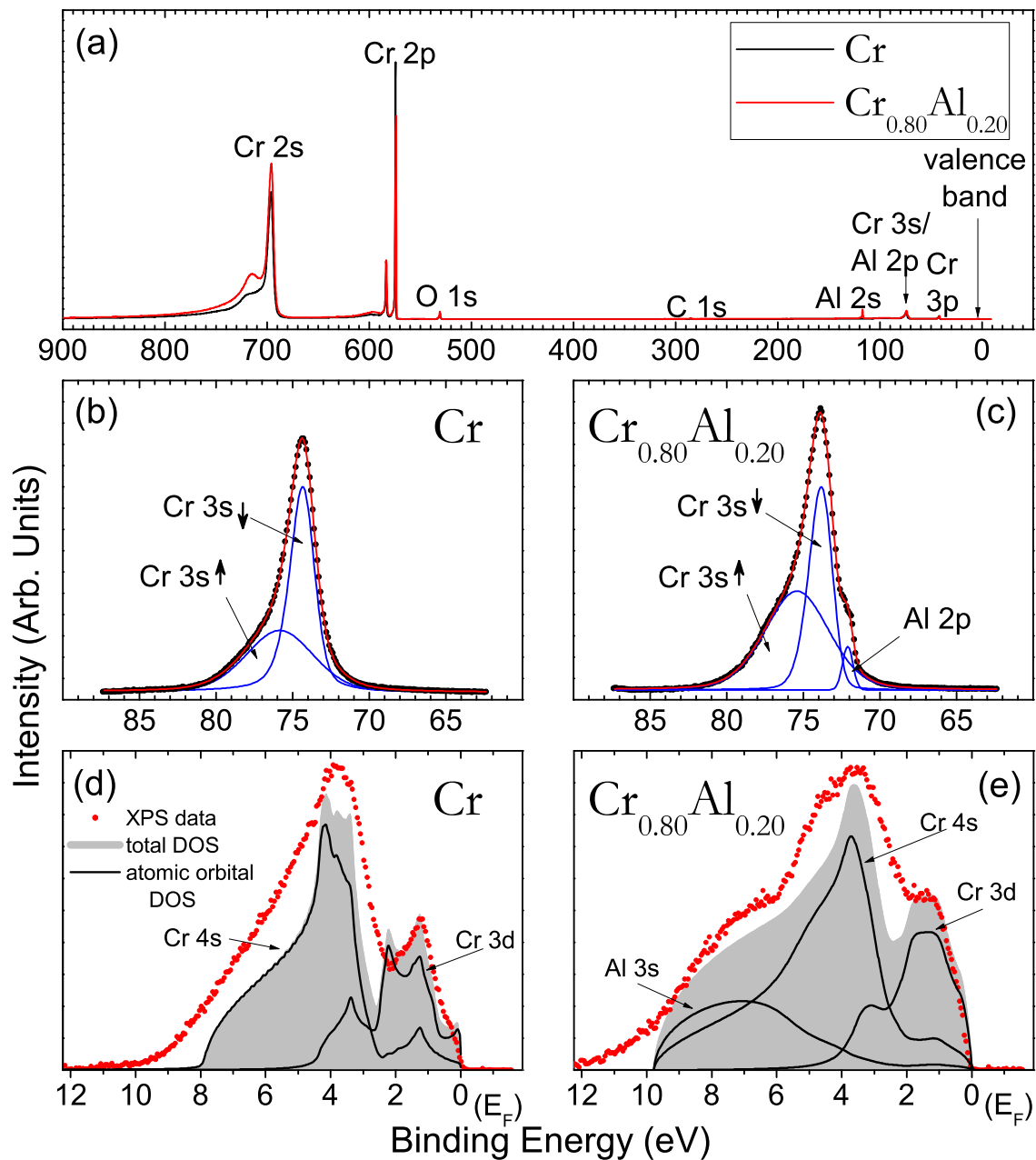
Figure 5.2: (a) Broad spectrum HXPS survey; (b-c) Cr 3s peak; (d-e) Experimental and theoretical weighted VB.

parallel to their atom's moment.[66] It is fit to a sum of two pseudo-Voigt peaks. For the $Cr_{0.80}Al_{0.20}$ sample the Al $2p$ peak falls nearby so it is shown as a sum of three pseudo-Voigt peaks. The integrated intensity of the broader multiplet peak is 1.82 times larger in $Cr_{0.80}Al_{0.20}$ than Cr, consistent with a larger Cr moment in $Cr_{0.80}Al_{0.20}$ (experimentally, 1.07 μ_B[31] vs. 0.43 μ_B rms moment).[1] DFT results in Cr moments of 1.6 μ_B in $Cr_{0.80}Al_{0.20}$ and 1.1 μ_B in Cr. The large calculated Cr moment is consistent with calculations in the literature and is due to overestimation of the moment by the GGA approximation.[53] The energy splitting between the multiplet peaks should also depend on moment; the splitting is 1.48 eV in Cr and 1.56 eV in $Cr_{0.80}Al_{0.20}$. This points to a larger moment in $Cr_{0.80}Al_{0.20}$ but the difference is not as large as expected. This may be due to our assumption of only two multiplet peaks.

Figure 5.2(d) and (e) depict the Shirley-background-subtracted VB spectra of Cr and $Cr_{0.80}Al_{0.20}$ along with the weighted DOS from the DFT calculations (the sum of the DOS of each atomic orbital weighted by its photoionization cross section). The neutral atom cross-sections from Scofield[106] were used, corrected for the experimental geometry and non-dipole effects[122, 123].

The DOS in the VB spectra is dominated by Cr 3d, Cr 4s and Al 3s contributions at 1.5 eV, 4 eV and 7 eV, respectively. The energies of the features associated with each subshell from theory agree well with the experimental spectra. In the Cr spectra, the two large peaks associated with the Cr 3d and 4s orbitals are very sharp. In addition, the small shoulder near E_F and the small bump at 2 eV can be attributed to peaks in the Cr 3d DOS, broadened by instrumental broadening. In $Cr_{0.80}Al_{0.20}$, the large Cr 3d and 4s peaks are significantly wider due to disorder broadening of the DOS. The tail extending to 10 eV is clearly attributed to the Al 3s orbital.

Figure 5.3(a) compares the experimental VBs of Cr and $Cr_{0.80}Al_{0.20}$ from Fig. 5.2 (d) and (e) on the same scale. Figure 5.3(b) shows the VB edges in the region very close to E_F with a Au reference. The VB edges of Cr and $Cr_{0.80}Al_{0.20}$ appear shifted to lower energy than the Au VB edge. This is due to two effects: the recoil effect[119] and the semiconducting gap in $Cr_{0.80}Al_{0.20}$.

Au has an essentially constant DOS in the region of E_F so that the shape of the curve at E_F is simply the Fermi-Dirac distribution function at room temperature convoluted with a 0.235 eV Gaussian from instrumental broadening. Thus, Au is used to calibrate E_F. The Cr and Au spectra are normalized such that the slopes of the Gaussian dropoffs are equal; this is the case because they are both subject to the same broadening mechanisms. The $Cr_{0.80}Al_{0.20}$ spectrum is normalized relative to Cr such that the total electron occupation times cross section weighted, integrated intensities are equivalent.

The VB edge of Cr is shifted 35 $\pm$ 14 meV below that of Au. Cr has a metallic Fermi edge, so this shift is due to recoil. The expected recoil shift between Cr and Au is 46 meV, consistent with our measurement.[2]

The $Cr_{0.80}Al_{0.20}$ VB edge is shifted 95 $\pm$ 14 meV below that of Cr. The recoil shift between Cr and $Cr_{0.80}Al_{0.20}$ is 7 meV, assuming an average atomic mass of 47 amu for $Cr_{0.80}Al_{0.20}$, within error of the gap measurement. Actually, the recoil shift should be less

---

[1]The SDW has 0.43 μ_B rms and 0.62 μ_B peak moment.[31]

[2]$\Delta E_{Cr-Au}^{recoil} = \left(\frac{m_e}{M_{Cr}} - \frac{m_e}{M_{Au}} \right) E_{kinetic}$
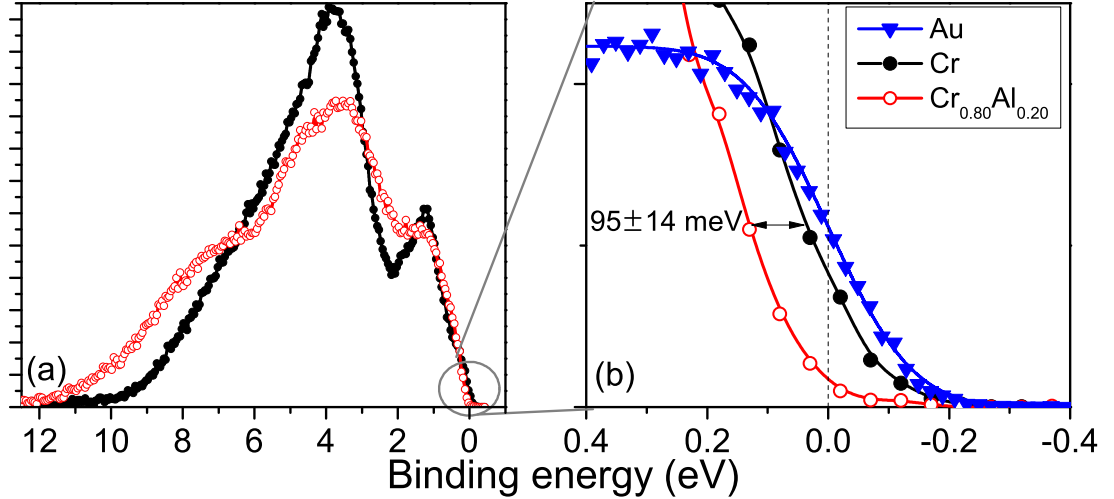
Figure 5.3: (a) HXPS VB; (b) HXPS VB near EF . Intensity scale is blown up 10x from (a).

than 7 meV because the electrons near the VB edge of $Cr_{0.80}Al_{0.20}$ are primarily Cr-like (see Fig. 5.2). Thus, the 95 ± 14 meV shift is due to the semiconducting gap in $Cr_{0.80}Al_{0.20}$ causing a sharp dropoff in the DOS below E_F. This suggests that the VB edge is 95 ± 14 meV below E_F, putting a lower limit on the size of the semiconducting gap.

5.4 Discussion

The observed gap in the $Cr_{0.80}Al_{0.20}$ VB spectrum is more striking when the weighting of atomic orbitals is considered because the s-orbital cross section is $16\times$ larger than the d at 5956.4 eV. In previous discussions of the semiconducting behavior in $Cr_{1-x}Al_x$, a qualitative explanation has been given in terms of the two $3d$ sub-bands in Cr, one below and one above E_F, narrowing with addition of Al and creating a gap in the d band.[18] The problem with this explanation is that it does not consider the s electrons, which dominate electrical conduction, and therefore does not explain the semiconducting behavior. There are significantly more Cr $3d$ than Cr $4s$ electrons at E_F; thus an enhanced $4s$ cross-section is required for the photoemission measurement of the gap to measure both d and s electronic states at E_F. The theoretical weighted contributions are shown in Fig. 5.2(d) and (e). Previous XPS of $Cr_{1-x}Al_x$ used soft x-rays (1500 eV) at which energy the s and d orbital cross sections are comparable; the previous work thus could not detect a gap in the s electrons.[79] Additionally, the soft x-ray study was susceptible to measuring surface states which could exist inside the bulk band gap.

The lower limit on the gap from the present measurement, 95 ± 14 meV, is comparable to but larger than previous estimates. Infrared reflectivity found a 40 meV gap in bulk $Cr_{0.81}Al_{0.19}$ and $Cr_{0.73}Al_{0.27}$; the difference could be due to different sample preparation or because infrared reflectivity can underestimate the gap due to exciton formation

below the band edge.[83] Resistivity analyses estimated gaps of 6-60 meV for $Cr_{1-x}Al_x$, $x = 0.14 - 0.28$, with the maximum gap occurring for 24 at. % Al.[18] These values are only approximate because the resistivity is not exponential in temperature.

DFT was used to generate the band structure of Cr and the Bloch spectral function (BSF) of $Cr_{0.80}Al_{0.20}$, shown in Fig. 5.4. In an alloy, disorder broadens the states into regions rather than bands, leading to the gray areas shown. The BSF is the k-projected DOS, $\mathcal{A}(E, \mathbf{k})$, which for a pure compound reduces to single valued dispersion relations $E_n(\mathbf{k})$ (the band structure).

The band structure of Cr in Fig. 5.4(a) shows states crossing E_F around M (holes) and X (electrons). Conduction in Cr occurs primarily by the holes around M.[18] The SDW opens a pseudogap in the regions $\Gamma - M$ and $R - \Gamma$,[30] which can be seen in the DOS in Fig. 5.4(c).

The BSF of $Cr_{0.80}Al_{0.20}$ in Fig. 5.4(b) shows $\Gamma - M$ and $R - \Gamma$ are still gapped due to the SDW. In addition, the hole band around M is shifted almost entirely below E_F, which should decrease conductivity due to a high effective mass and higher likelihood of localization as well as a lower $DOS(E_F)$. This explains previous Hall effect data showing conduction switching from holes in pure Cr to electrons for $x \geq 0.15$[18].

The DOS of Cr and $Cr_{0.80}Al_{0.20}$ are shown in Fig. 5.4(c) and (d), with (e) comparing the DOS near E_F. In $Cr_{0.80}Al_{0.20}$, the shift of the holes at M leads to a sharp dropoff in states just below E_F, as suggested by Fig. 5.3. The $DOS(E_F)$ is much smaller than that of Cr, but still nonzero. It is possible that the gap leading to the semiconducting transport behavior and photoemission results is not a complete gap and a few states remain at E_F; Fig. 5.3 is compatible with this possibility since a small but finite intensity is observed at zero binding energy. Previous results are also consistent with an incomplete gap, such as resistivity which is not exponential in temperature[18, 91], an infrared "gap" showing finite reflectivity in the DC limit[83], and a nonzero electronic contribution to the specific heat.[95]

DFT is thus largely consistent with the experimental data. However, some details remain to be explained: the calculated $DOS(E_F)$ for $Cr_{0.80}Al_{0.20}$, while decreased compared to Cr, is larger than expected from the previously measured electronic contribution to the specific heat.[95] In addition, the $Cr_{0.80}Al_{0.20}$ DOS in the region near E_F, when convoluted to simulate experimental broadening, does not reproduce the observed 95 meV VB edge shift but falls much closer to the Cr DOS. DFT is known to underestimate the band gap of materials[84], thus it is possible that in the real $Cr_{0.80}Al_{0.20}$ material the holes at M are completely shifted below E_F, widening the gap and sharpening the DOS dropoff. In addition, if an ordered Cr_3Al structure exists, as has been speculated[24], it would have a different band structure which could have sharp features near E_F.

5.5 Conclusion

In summary, a gap is observed in $Cr_{0.80}Al_{0.20}$ by HXPS, with the VB edge 95 $\pm$ 14 meV below E_F. HXPS provided advantages over soft x-ray photoemission such as decreased sensitivity to surface states and a relatively increased photoionization cross section for s states, so the measurement truly reflects a gap in the bulk conducting s states and
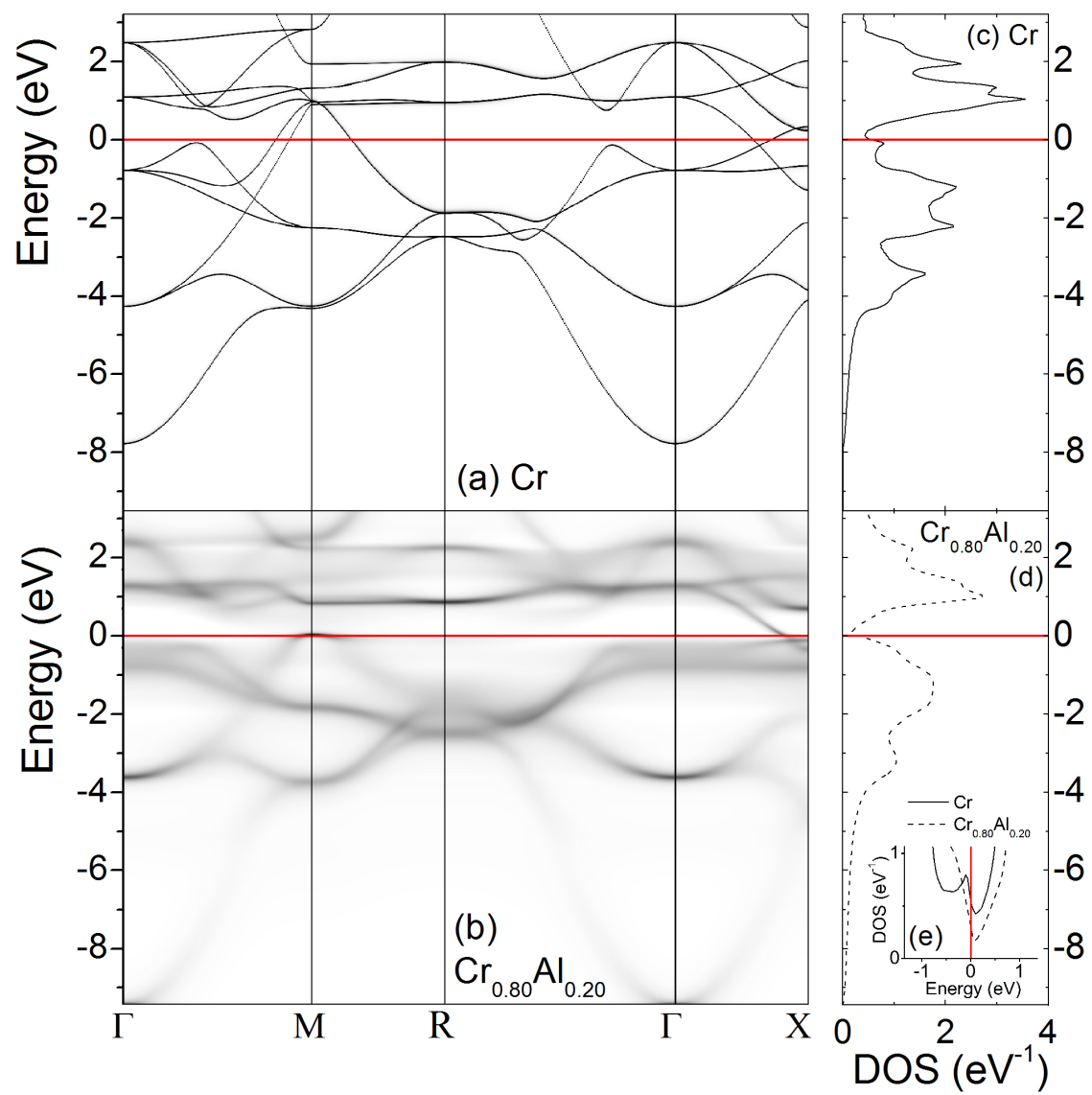
Figure 5.4: (a) Cr band structure; (b) Cr0:80Al0:20 BSF; (c-d) DOS; (e) DOS near EF .

not simply a splitting of two d sub-bands.

DFT agrees well with the HXPS VB spectra. It shows that the primary carriers in Cr, the holes around M, are shifted almost entirely below E_F in $Cr_{0.80}Al_{0.20}$. It shows an incomplete gap in $Cr_{0.80}Al_{0.20}$, with a small number of states at E_F; this is consistent with the photoemission and resistivity results. Future work will investigate the possibility of an ordered structure.

Chapter 6

Chemical ordering in Cr$_3$Al and relation to semiconducting behavior

6.1 Introduction

Alloys and compounds made of metallic elements are generally expected to be metallic, and indeed most are. However, some such compounds are semiconducting or semimetallic, such as RuAl$_2$ and Fe$_2$VAl.[129] In theory, any compound with an even number of valence electrons in the primitive unit cell can be semiconducting because the electrons can completely fill the valence band. Transition metals usually have several overlapping bands at the Fermi energy (E_F) so even in compounds with an even number of electrons typically several bands are partially filled. For an intermetallic compound to be semiconducting, hybridization must shift the bands in a fortuitous way, leaving a gap at E_F.

When intermetallic compounds do have a gap at E_F, they are the subject of significant study. The gap can be exploited for applications, for example, intermetallic semiconductors are attractive for thermoelectric devices due to their typically small gaps and large Seebeck coefficients (ex. ZrNiSn).[125] In ferro- or ferrimagnetic compounds, the gap is generally asymmetric with spin; if a gap occurs at E_F for one spin but not the other, the result is a half metal (ex. Co$_2$MnAl).[75] Half-metals are important for spintronics applications such as spin transistors and non-volatile logic.

Cr$_{1-x}$Al$_x$, with $x = 0.15 - 0.26$, shows semiconductor-like electronic behavior that has not been explained until now. Our photoemission study in Chapter 5 showed a narrow gap or pseudogap at E_F in a Cr$_{0.80}$Al$_{0.20}$ thin film.[13] A maximum resistivity of 3600 $\mu\Omega$-cm occurs, with a negative temperature coefficient of resistivity.[18, 91] In addition, a large Hall coefficient and a small electronic specific heat is observed[18, 95], all hallmarks of semiconducting behavior. Cr$_{1-x}$Al$_x$ is also antiferromagnetic for $x = 0 - 0.50$.[31, 72, 62] The maximum resistivity and Hall coefficient and minimum electronic specific heat all occur around $x = 0.25$, with a plateau in the magnetic susceptibility at the same x,[72] suggesting an ordered Cr$_3$Al compound is responsible for the behavior.

The structural Cr-Al phase diagram is not entirely clear, and is discussed in further

detail in Section 6.2. The original phase diagram showed Al soluble in Cr up to 26 at. % Al, with no ordered Cr_3Al phase.[72] An ordered Cr_3Al compound was later proposed from electron diffraction, but has not been confirmed by other researchers. The proposed structure is a rhombohedral superlattice based on the bcc structure.[24]

Another structure to consider is the Heusler structure. The Heusler structure is commonly seen for compounds with a ratio of transition metal:main group element of 3:1, like Cr_3Al. The Heusler compounds have a standard electronic band structure which, upon substitution with different elements, is simply tuned by the total number of valence electrons in a unit cell. A band gap exists between the twelfth and thirteenth bands, so that compounds with a total number of valence electrons $Z = 24$ are semiconducting or semimetallic (e.g. Fe_2VAl). Several compounds with more or less electrons are half metallic, with a total magnetization related to the valence electrons by a simple, linear Slater-Pauling scheme: $M = Z - 24$.[43] This relation makes the electronic and magnetic properties of the Heusler compounds predictable and tunable, and thus very attractive for materials design.

The Cr_3Al formula unit contains $Z = 21$ valence electrons (an odd number). How can any Cr_3Al structure have a gap at E_F if the total number of electrons is odd? This question is one reason the nonmetallic transport behavior in Cr_3Al has remained unexplained.

In this chapter, we use experimental thin film growth techniques as well as theoretical density-functional theory (DFT) calculations to explore the connection between chemical ordering in Cr_3Al and the observed semiconductor-like transport behavior. We find a strong dependence of the transport behavior on growth temperature, such that Cr_3Al films can be made either metallic or semiconductor-like depending on the growth conditions and resulting chemical ordering. Additionally, our theoretical results show that the proposed X-phase structure could explain the observed transport due to a semimetallic band structure.

6.2   Background

Based on x-ray diffraction (XRD), Koster et al[72] created a phase diagram of $Cr_{1-x}Al_x$ in 1963. Koster's phase diagram, reproduced in Figure 6.1(a), shows a bcc solid solution (α) as the stable phase from $x = 0 - 0.26$. The $C11_b$ Cr_2Al (β) phase is shown for $x = 0.29$ - 0.34 and a two phase region is shown between $x = 0.26$ - 0.29. Koster et al. suggested that a Cr_3Al ordered compound may exist due to the nonlinear dependence of magnetic susceptibility on x, but found no evidence for it in XRD and did not include it on the phase diagram.

In 1981, den Broeder et al saw evidence in transmission electron microscopy (TEM) diffraction patterns for an ordered Cr_3Al structure at temperatures below 400°C.[24] They observed additional diffraction spots which could be interpreted as superlattice spots. They proposed an ordered phase, called the X-phase, for $x = 0.19$ - 0.26, with a low 400°C phase boundary. The updated phase diagram, taken from Murray's 1998 phase diagram evaluation, is shown in Figure 6.1(b).[89]

According to dark field imaging, the X-phase ordering occurs in small, 1-3nm domains, even within a large bcc crystallite. The roughly 400°C phase boundary was
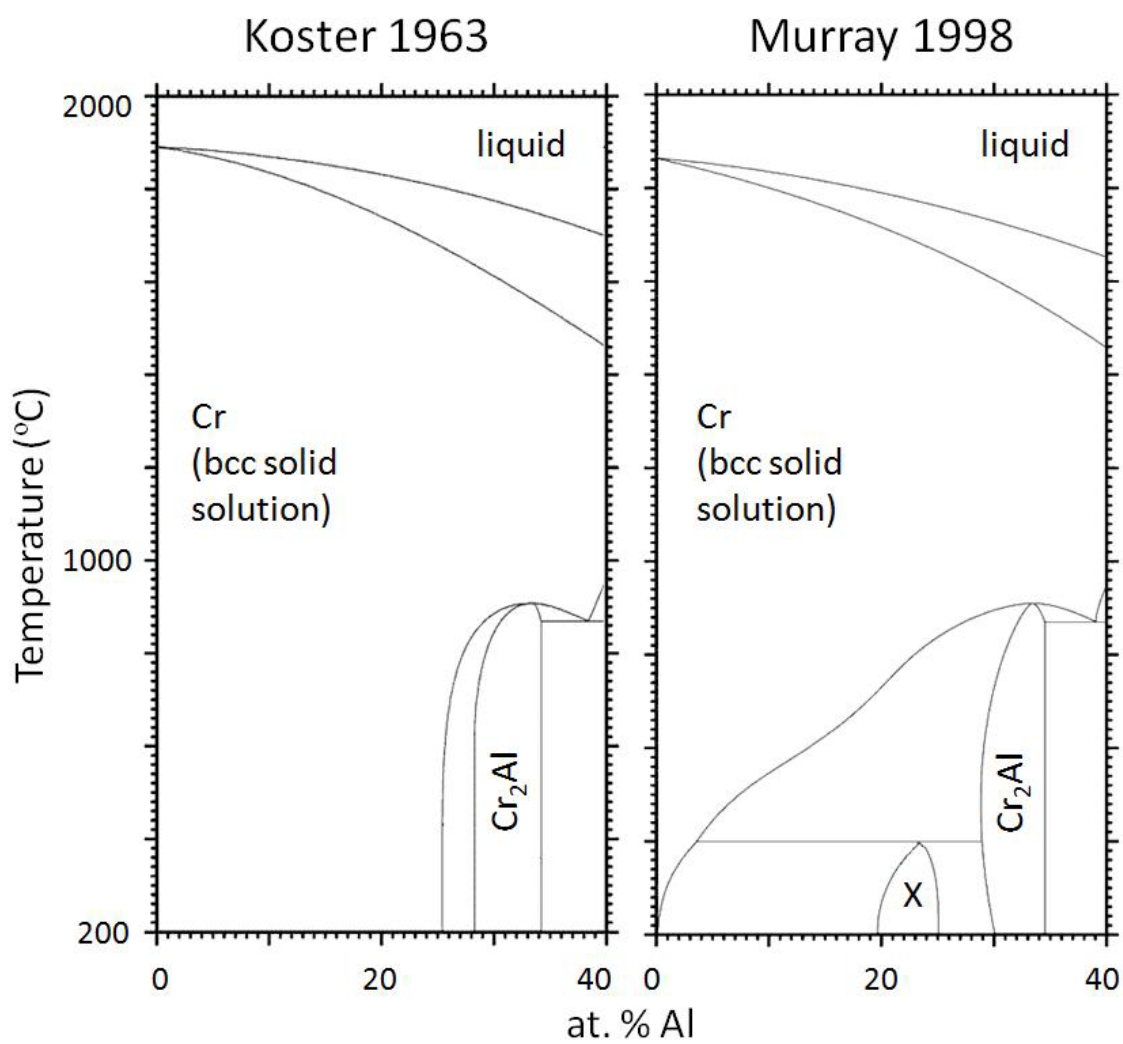
Figure 6.1: Binary phase diagrams of the $Cr_{1-x}Al_x$ system, as shown by Koster et al[72] and Murray[89].

suggested because annealing at temperatures 400°C or above did not improve the size of the crystallites.[24] Such a low phase boundary temperature can impede long range order because the low atomic mobility requires extremely long annealing times to achieve ordering. Thus, the X-phase observed by den Broeder et al is best described as short- to medium-range order.

Based on first order diffraction spots, the authors suggested that the X-phase was a rhombohedral structure with 8 atoms in the unit cell. Because no higher order diffraction spots were observed, they could not be conclusively attributed to a specific structure and thus Cr_3Al and Cr_5Al_3 were both suggested as candidates for the X-phase. For the purposes of this work, we consider the Cr_3Al structure. The X-phase is still considered speculative because it has only been observed once.

The proposed phase diagram in Figure 6.1(b) shows, for the Cr_3Al composition, three solid phases occurring in different temperature ranges. The X-phase is stable below 400°C, the $C11_b$ Cr_2Al + bcc Cr two phase system is stable from 400°C to 800°C, and the bcc solid solution is stable above 800°C until melting.

We will explore here the three structures shown on the proposed phase diagram: bcc solid solution, $C11_b$ Cr_2Al + bcc Cr two-phase system, and X-phase Cr_3Al structure, as well as the off-stoichiometric $C11_b$ Cr_3Al structure, which we see experimentally, and the $D0_3$ structure for completeness.

6.2.1   bcc Cr

Cr occurs in the bcc structure, shown in Figure 6.2(a), and all the Cr_3Al structures discussed here have a bcc-like atomic environment, albeit with different types of chemical ordering and in some cases slight distortion.

The bcc structure has with one atom per primitive unit cell. However, when simple antiferromagnetism is considered, there are two atoms per unit cell (one up - cube edge, one down - body center).

6.2.2   bcc solid solution $Cr_{0.75}Al_{0.25}$

This structure occurs when Al is added to the bcc Cr system and the Al atoms are placed randomly on the lattice sites. The lattice constant is increased slightly because the atomic radius of Al is larger than that of Cr.[18] This structure is shown in Figure 6.2(b).

6.2.3 $C11_b$ Cr_2Al

The $C11_b$ Cr_2Al structure is layered along the bcc (001) planes, so that there are alternating layers (Cr, Cr, Al, Cr, Cr, Al...). Thus the unit cell consists of essentially three bcc unit cells, with six atoms per Cr_2Al unit cell. The layering creates a 4% tetragonal distortion.[72] The $C11_b$ Cr_2Al structure is shown in Figure 6.2(c).

The proposed phase diagram only shows single phase $C11_b$ Cr_2Al for about $x = 0.29 - 0.34$, so for the Cr_3Al stoichiometry, the two phase $C11_b$ Cr_2Al + bcc Cr structure is considered. $C11_b$ Cr_2Al also displays simple antiferromagnetism.[8]

(a) bcc Cr

(c) Cr$_2$Al

(e) D0$_3$ (binary Heusler)

Legend:

Cr

Al

random Cr or Al

(b) bcc solid solution (Cr$_{0.75}$Al$_{0.25}$)

(d) C11$_b$ Cr$_3$Al [i.e. Cr$_2$(Al$_{1\text{-}\delta}$Cr$_\delta$)]

(f) X-phase
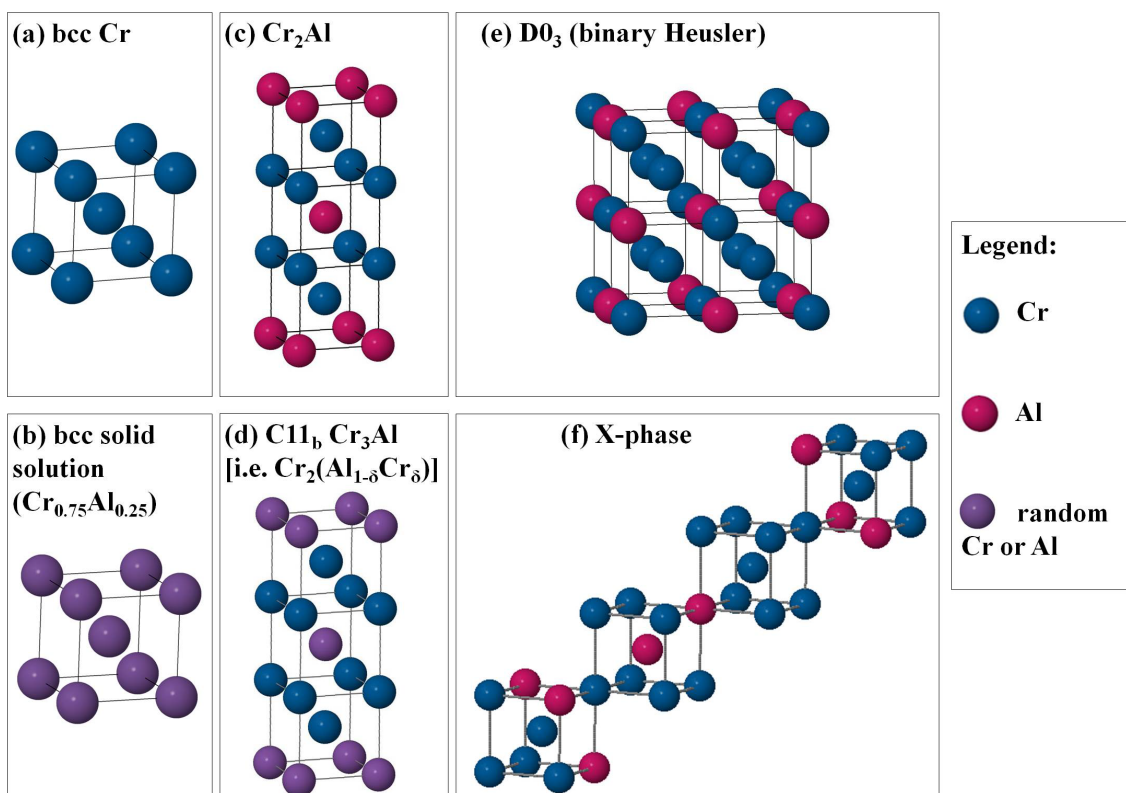
Figure 6.2: Structures considered in Sections 6.5 and 6.6. For (b), the atoms are randomly Cr or Al in the ratio Cr$_{0.75}$Al$_{0.25}$. For (d), the atoms on the Al sites are randomly Cr or Al in the ratio Cr$_{0.25}$Al$_{0.75}$, for a total stoichiometry of Cr$_2$(Al$_{0.75}$Cr$_{0.25}$), or Cr$_3$Al.

6.2.4   C11$_b$ Cr$_3$Al

Although single-phase C11$_b$ does not appear for the Cr$_3$Al stoichiometry on the phase diagram, we observe it experimentally. In this case, the C11$_b$ Cr$_2$Al structure has the additional Cr atoms substituted randomly onto Al sites (i.e. Cr$_2$(Al$_{1-\delta}$Cr$_\delta$), where $\delta =$ 0.25 for the Cr$_3$Al stoichiometry). The C11$_b$ Cr$_3$Al structure is shown in Figure 6.2(d).

6.2.5   D0$_3$ Cr$_3$Al

We include the binary Heusler structure (D0$_3$), although it does not appear on the phase diagram, because so many other bcc transition metal-Al alloys take this form. The full Heuslers have a A$_2$BD structure, where A and B are transition metals and D is an *sp* element. The atoms occupy the sites of a bcc lattice with an L2$_1$ ordering. For binary Heuslers (A$_3$D), atom A occupies two distinct sites and can be thought of as A(I)$_2$A(II)D (e.g. Fe$_3$Si).

The D0$_3$ ordering can be seen as 4 interpenetrating fcc lattices, thus the primitive unit cell contains 4 atoms. In Figure 6.2(e), Cr(I) occupy the body centers of the cube, while Cr(II) and Al occupy alternating cube edges. Cr$_3$Al in the D0$_3$ structure has been considered theoretically before, and has been calculated to be ferrimagnetic due to antiferromagnetic coupling between the Cr(I) and Cr(II) sites with different magnitudes of moment.[81]

6.2.6   X-phase Cr$_3$Al

The proposed X-phase is a chemically ordered, rhombohedrally distorted phase based on the bcc structure.[24] The primitive unit cell is a rhomboid containing 8 atoms along the bcc [111] direction: 6 Cr atoms followed by 2 Al atoms. The primitive lattice vectors are [211], [121], and [112] in the bcc coordinates. The rhombohedral unit cell appears in Figure 6.2(f).

6.3   Experimental Methods

Most previous studies of Cr-Al alloys have used bulk samples, although a few studies have focused on the potential applications of Cr-Al thin films as the antiferromagnetic layers in exchange-biased multilayer systems[67, 138, 80] and as thin film resistors.[92] In contrast to bulk sample growth, thin film growth often stabilizes nonequilibrium crystal structures, for example through quenching of films grown at high temperatures, restriction of lattice parameters due to the substrate, and surface energy effects. We have used thin film growth techniques in order to study the effect of structure on the transport properties of Cr-Al.

Thin films of Cr$_{1-x}$Al$_x$, with thickness $\sim$400Å, were grown epitaxially on MgO(001) and a-SiO$_2$/Si substrates[1] by co-deposition of Cr from an e-beam source and Al from an effusion cell at a rate of 0.4 Å/s and a base pressure of 5×10^{-9} Torr. One series was grown at a substrate temperature of 300°C, with the Al concentration (x) varied. Another series

---

[1]The a-SiO$_2$ layer provides an amorphous surface to achieve polycrystalline, rather than epitaxial, film growth. In addition, it acts as a diffusion barrier to prevent silicide formation at the interface.

of films was grown at a fixed Al concentration ($x = 0.24$) but varied substrate temperature from 200-600°C. We did not attempt growth above 600°C due to the potential loss of Al above its melting temperature (660°C).

Cr(001) is known to grow epitaxially on MgO(001).[38, 40] The MgO lattice constant is 4.211Å, or about $\sqrt{2}$ larger than that of Cr. The Cr lattice grows 45° rotated compared to the substrate ([001]Cr $\parallel$ [110]MgO). For pure Cr, the lattice mismatch for this epitaxial relation is 3.9%, while the addition of Al increases the lattice constant and improves the mismatch to 0.9% at the Cr_3Al stoichiometry. Epitaxy was verified in-situ by reflection high energy electron diffraction (RHEED) which showed a streaky pattern and ex-situ by x-ray diffraction (XRD) which showed four-fold symmetry of the (011) peak in an azimuthal scan at 45° from normal. In addition, only the bcc (001) orientation is seen in a $\theta - 2\theta$ scan (see Figure 6.3). The films grown on a-SiO$_2$/Si are polycrystalline.

The films have been confirmed to be antiferromagnetic by neutron diffraction in Chapter 7.

The films were patterned lithographically to form a defined geometry for the resistivity measurements. The resistivity was measured from 2-300K by a four-probe technique, averaging forward and reverse currents to avoid thermal voltages. In addition, the I-V curve was confirmed to be linear for each sample.

6.4   Experimental Results

The 2K resistivity is shown as a function of Al concentration in Figure 6.4. It shows a clear peak at 25 at. % Al, similar to the results on bulk samples.[18, 91] In addition, the temperature dependence of the resistivity is shown in the inset for 23 at. % Al for both an epitaxial and polycrystalline film. The negative temperature dependence is decidedly nonmetallic, and also similar to what has been seen in bulk.

However, there are significant differences between the thin films and bulk. In the bulk, the metallic Cr_2Al phase begins to precipitate at 26 at. % Al, leading to a steep drop in resistivity above 25 at. %. Thus, it could not be determined previously whether the peak ρ(2K) at 25 at. % Al was related to formation of a distinct Cr_3Al phase, or whether a peak in ρ(2K) occurred at 25 at. % Al simply due to an accidental confluence of factors: slowly increasing resistivity with x combined with a sudden drop at 26 at. % Al due to precipitation of metallic Cr_2Al.

In contrast to bulk, none of our films shown in Figure 6.4 (grown at 300°C) show evidence of the Cr_2Al phase in XRD, even up to 37 at. % Al. This is evidence of nonequilibrium structure formed by the thin film growth process. The resistivity in our films still peaks at 25 at. % Al, but the decrease above 25 at. % is much more gradual in the films than in bulk, still displaying nonmetallic behavior up to about 37 at. % Al. This suggests that the peak in ρ(2K) at 25 at. % Al is in fact related to an ordered Cr_3Al structure rather than precipitation of the Cr_2Al phase.

The magnitude of the peak resistivity reaches about 2300 $\mu\Omega$-cm in the films, but as high as 3600 $\mu\Omega$-cm in the bulk.[18, 91] This difference is as of yet unexplained, but could be due to a different quality of Cr_3Al formation in the samples, or due to strain in the films, either from thermal expansion or substrate mismatch effects.
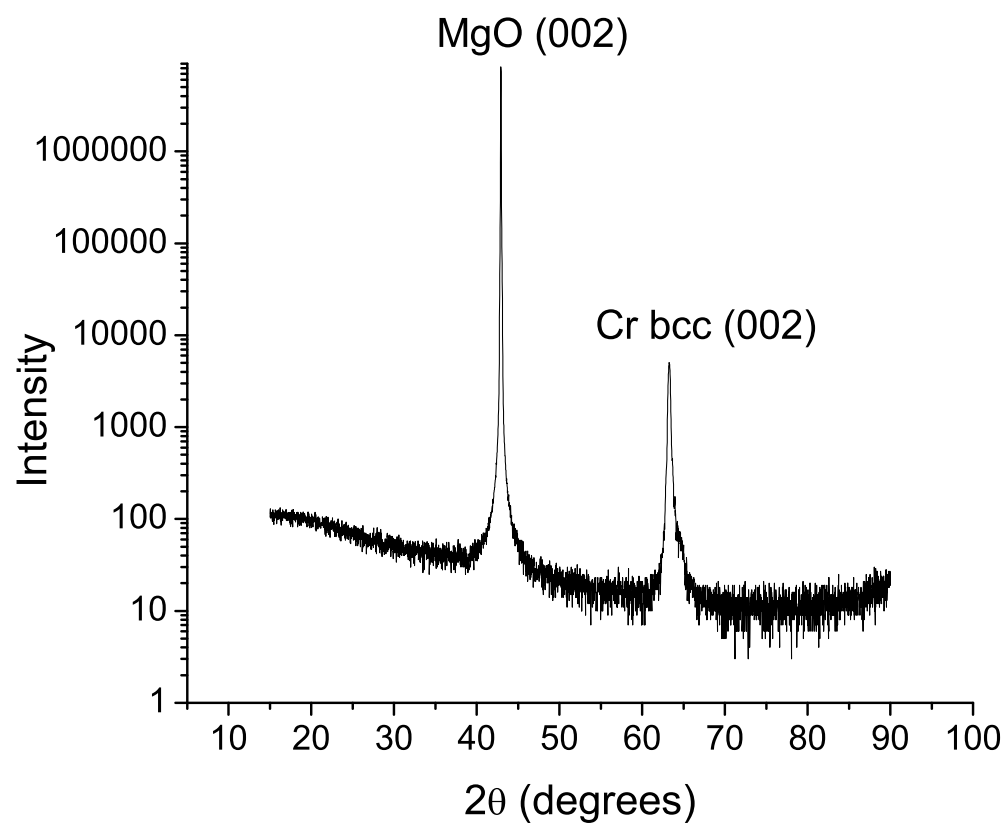
Figure 6.3: X-ray diffraction (XRD) of a 400Å Cr$_3$Al thin film grown at 300°C
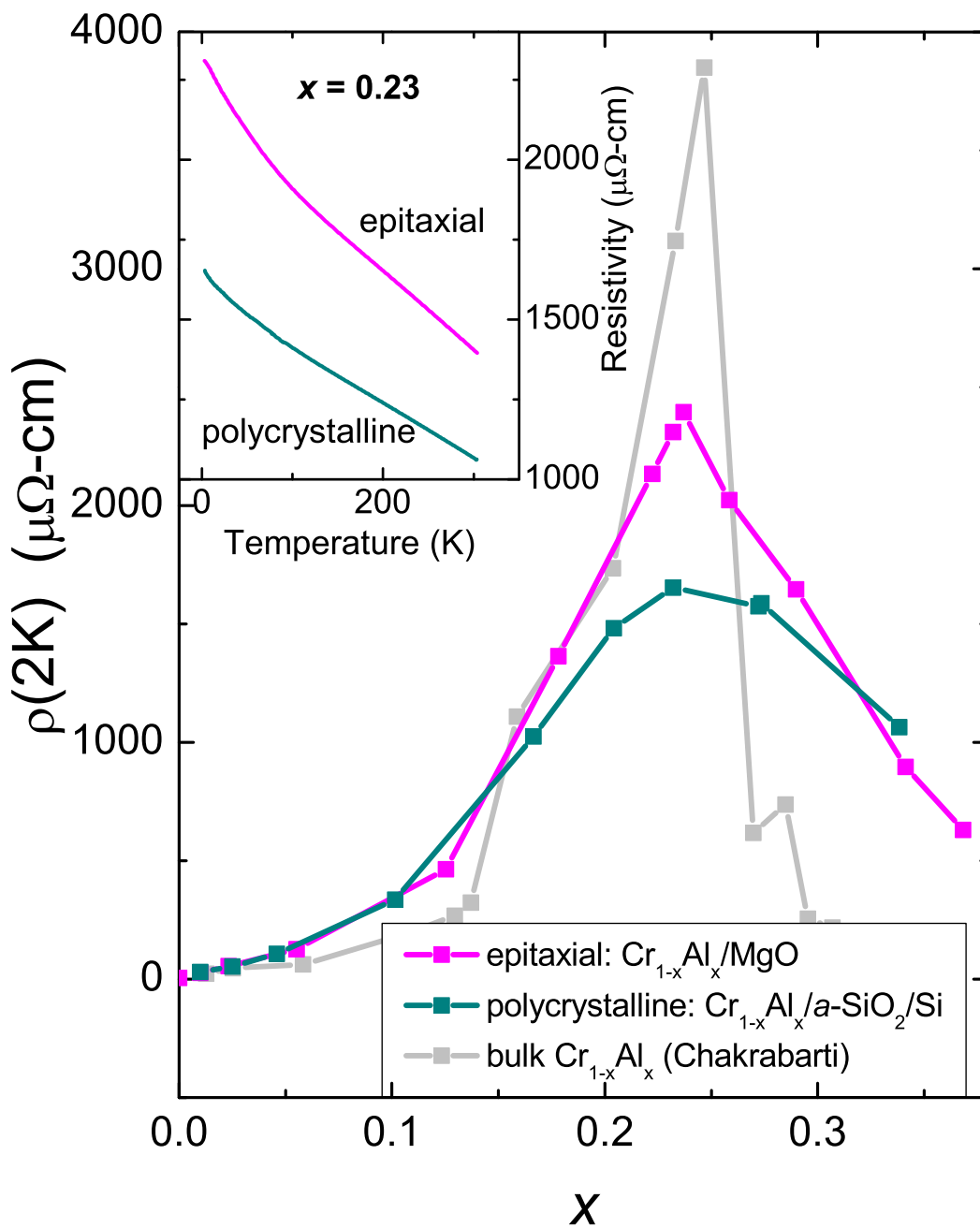
Figure 6.4: Resistivity of $Cr_{1-x}Al_x$ thin films vs. x at 2 K. All films shown here were grown at 300°C. Bulk data from Ref. [18]. Error bars are smaller than the symbol size. Inset: Resistivity of $Cr_{0.77}Al_{0.23}$ vs. temperature
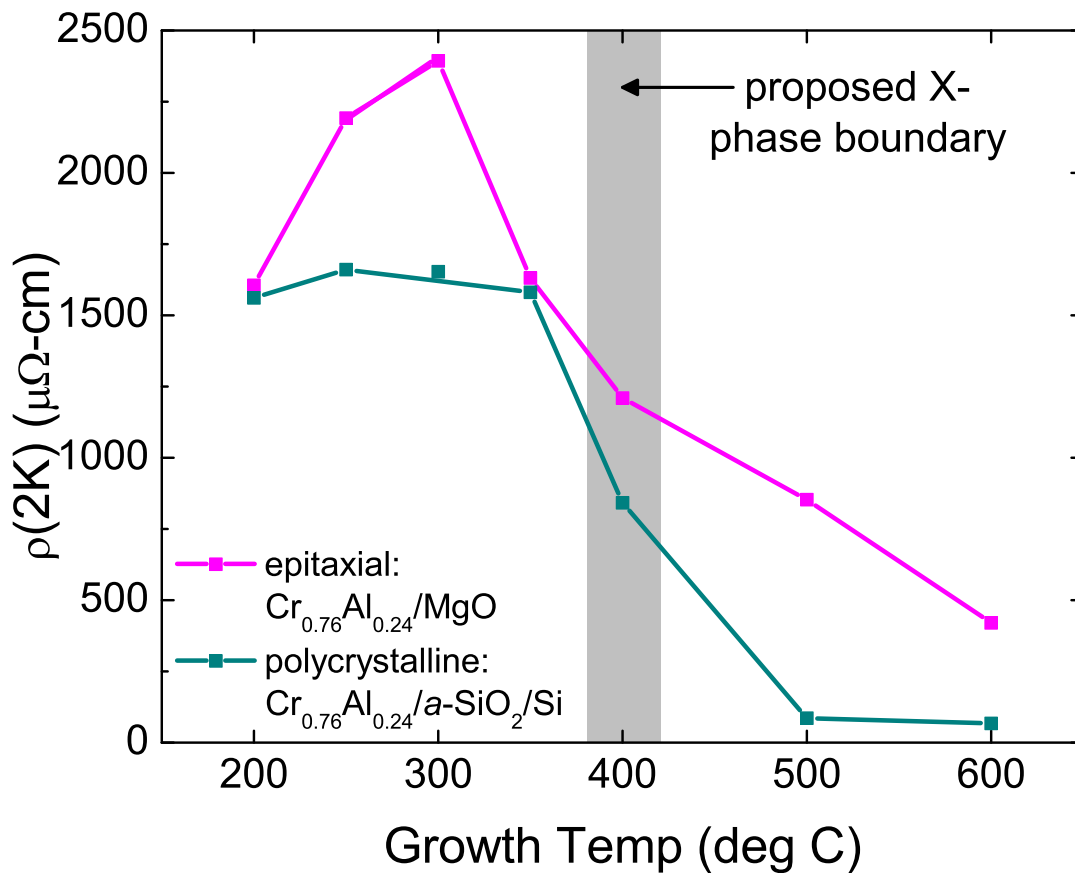
Figure 6.5: Resistivity of $Cr_{0.76}Al_{0.24}$ thin films vs. growth temperature at 2 K. Error bars are smaller than the symbol size.

Figure 6.4 also shows a noticeable effect of the substrate. The polycrystalline films, grown on a-SiO_2/Si, have a significantly lower resistivity than their epitaxial counterparts. This can be seen clearly in the Figure 6.4 inset comparing two films grown at the same time on different substrates. The polycrystalline films not only have lower 2K resistivity, but a weaker temperature dependence of resistivity.

This result is surprising at the outset, given that the primary quantities leading to the resistivity are the scattering time τ and the number of carriers n. The addition of grain boundaries adds scattering centers and should decrease τ, leading to higher resistivity. The lower resistivity of the polycrystalline samples implies an opposing, and larger, effect on n, further suggesting that the anomalous transport behavior in this material is due to a band structure effect. Specifically, this implies that that structure is important to decreasing n, as adding disorder in the form of grain boundaries causes n to increase.

In order to further explore the effect of structure on the transport properties, we grew a series of samples, with 24 at. % Al, at a range of growth temperatures from
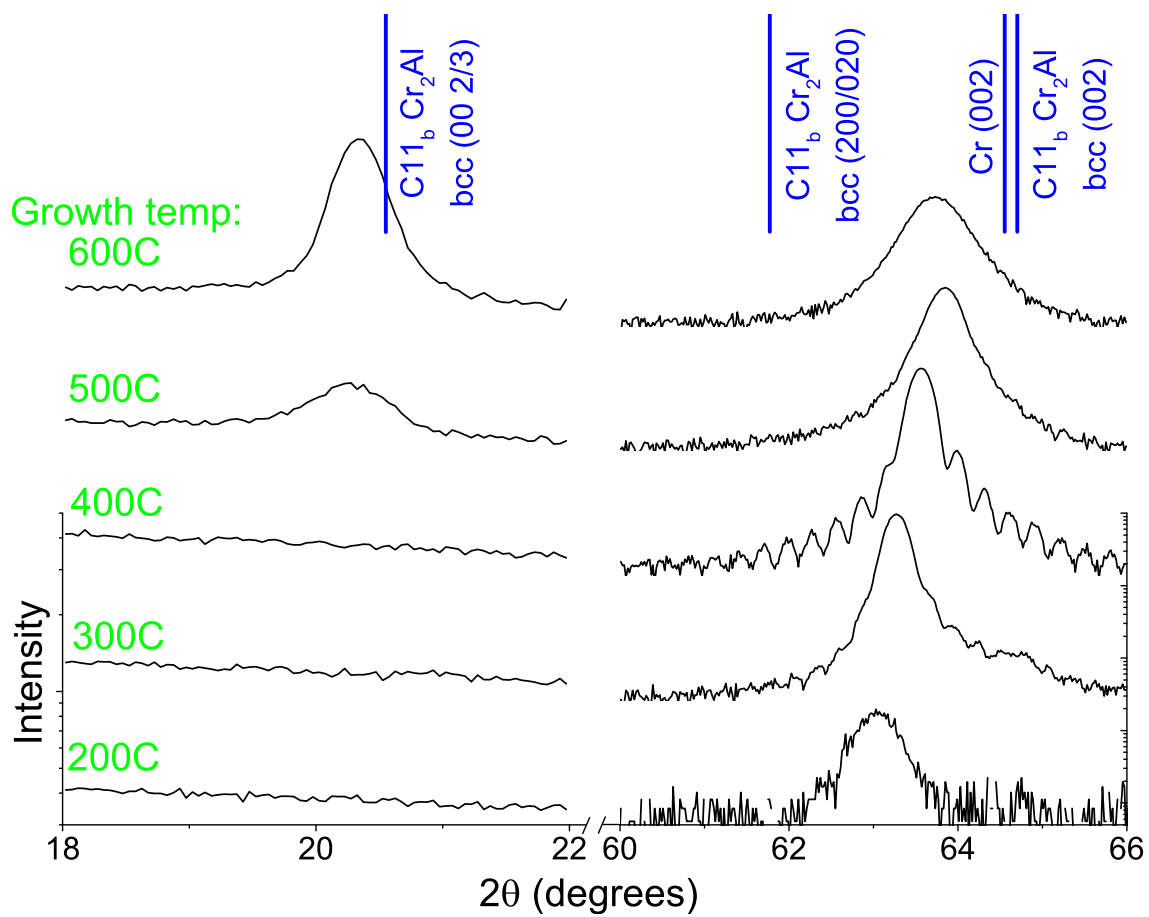
Figure 6.6: XRD of epitaxial $Cr_{0.76}Al_{0.24}$ thin films vs. growth temperature.

200-600°C. This range of growth temperatures straddles the proposed X-phase transition temperature of 400°C. The 2K resistivity is shown as a function of growth temperature in Figure 6.5.

The results show a marked difference in resistivity with growth temperature, with a transition from clearly nonmetallic behavior at lower growth temperature to more metallic behavior at the highest growth temperatures. This trend aligns with the proposed phase boundary at 400°C from X-phase Cr_3Al to metallic $C11_b$ Cr_2Al + Cr. Indeed, the epitaxial films grown at 500 and 600°C show $C11_b$ superlattice peaks at the bcc $(0\ 0\ \frac{2}{3})$ position, while the films grown at low temperature do not, as shown in Figure 6.6.

The peak resistivity in the epitaxial films occurs at 300°C, just below the proposed X-phase transition temperature. This implies that films grown at 300°C have the highest quality X-phase ordering (compared to films grown at lower temperatures), while films grown at higher temperatures have begun the transition to $C11_b$ ordering.

The transition from nonmetallic to metallic behavior is much sharper in the polycrystalline films than the epitaxial films. In addition, the high temperature grown polycrystalline films are much more metallic than the epitaxial ones. The difference in behavior between the epitaxial and polycrystalline films is not exactly clear, but one possibility is due to different formation of the $C11_b$ phase in these films.

Further details of the structural transition with growth temperature can be seen in the XRD data. XRD of the epitaxial films with varying growth temperatures is shown in Figure 6.6. All of the films show a single, unsplit bcc (002) peak. The position of the (002) peak shifts to the right with increasing growth temperature, implying a tetragonal distortion. In addition, some of the (002) peaks have sufficient intensity to show thickness oscillations, corresponding to the approximately 400Å thickness of the films.

Clear $(0\ 0\ \frac{2}{3})$ superlattice peaks are seen in the films grown at 500 and 600°C, implying $C11_b$ ordering.[73] Interestingly, it appears that we observe single phase $C11_b$ ordering in these $Cr_{0.76}Al_{0.24}$ films, despite the bulk $C11_b$ Cr_2Al phase solubility extending only down to 29 at. % Al. If two phase $C11_b$ Cr_2Al + Cr were formed, as suggested for 24 at. % Al by the phase diagram (Figure 6.1(b)), the (002) peak should be split into a Cr and Cr_2Al peak. However, we see no Cr (002) peak, implying single phase $C11_b$ ordering in these films. This off-stoichiometric $C11_b$ Cr_3Al structure can be thought of as $Cr_2(Al_{1-\delta}Cr_\delta)$, with the additional Cr atoms substituting onto Al sites. The structure is shown in Figure 6.2(d).

In addition, we see that c, the axis along which ordering occurs, points preferentially in the out of plane direction. Due to the tetragonal distortion of the $C11_b$ structure, the different a and c lattice constants would lead to a split diffraction peak. However our films show clearly unsplit bcc (002) peaks in Figure 6.6.

A comparison of in- and out- of plane XRD peaks shows that the tetragonal distortion in our 600°C film is less than that of bulk Cr_2Al (in our film, $a = 2.95$Å, $c = 8.75$Å, or 1% distortion; in bulk Cr_2Al, $a = 3.001$Å, $c = 8.637$Å, or 4% distortion[72]) The lattice distortion is due to the layered structure (Cr, Cr, Al, Cr, Cr, Al...), with Al atoms having a larger radius than the Cr atoms. This causes not only a tetragonal distortion, but relaxation of the layers within the cell. The smaller distortion in our films can be explained by the Cr_3Al (i.e. $Cr_2(Al_{1-\delta}Cr_\delta)$) stoichiometry, such that the layers (Cr, Cr, $Al_{1-\delta}Cr_\delta$, Cr, Cr,

$Al_{1-\delta}Cr_\delta$...) are more similar in size than in the Cr_2Al stoichiometry.

The formation of single-phase $C11_b$ Cr_3Al in our films, although it does not occur in the phase diagram, is not surprising. Samples grown using vapor deposition techniques often show nonequilibrium structures, due to the kinetics of phase nucleation. In addition, surface energy effects during growth can cause ordering to occur preferentially along a certain direction, which can explain the orientation of the $C11_b$ c axis in the out of plane direction. Finally, epitaxy may cause one phase to be preferred over another due to a better lattice constant match with the substrate, or preferential orientation due to a constraint on the lattice constant in the in-plane direction.

6.5   Theoretical Methods

DFT calculations were done using the AkaiKKR code, a full-potential DFT Green's function approach based on the Korringa-Kohn-Rostoker multiple-scattering technique.[2, 71, 70] The scalar relativistic approximation was used and disorder in the bcc solid solution was treated using the coherent potential approximation (CPA).[112, 1] The number of irreducible k points used for Brillouin zone integration was between 3009 and 3276 for the different structures. The generalized gradient approximation (GGA) was used to approximate the exchange-correlation energy[94].

6.6   Theoretical Results

Because pure Cr is a well studied system, we compare our calculations of Cr to experiment to verify that we have chosen appropriate parameters. The calculated Cr lattice constant is very close to experiment (2.882Å calculated, 2.885Å experimental). In addition, the bulk modulus is extremely close (1.86 Mbar calculated, 1.97 Mbar experimental). Pure Cr has a spin density wave (SDW) incommensurate with the lattice that is computationally difficult. Not only does it require a large unit cell but it is, as of yet, not found to be the minimum energy state in current DFT calculations.[53] For these reasons, we simplify and assume the commensurate SDW (simple antiferromagnetism) for Cr. We obtain a larger magnetic moment than experimentally observed (1.1 μ_B calculated, 0.60 μ_B experiment[31], in the commensurate SDW phase). The large calculated Cr moment is consistent with calculations in the literature and is due to overestimation of the moment by the GGA approximation.[53]

Table 6.1 shows the relevant calculated parameters for the Cr_3Al structures. The first and second columns show the lattice parameters and magnetic state. Both the calculated bcc solid solution and X-phase have similar lattice parameters to experiment. The rhombohedral distortion of the X-phase is small, and if it occurred in many small domains as seen experimentally by den Broeder[24], the distortion would not be seen in XRD. The Cr_2Al phase, on the other hand, has a significant tetragonal distortion, which is seen experimentally.[73] The $D0_3$ phase has cubic symmetry, but a significantly larger lattice constant than the experimental value. In addition, all of the calculated structures show antiferromagnetic order except $D0_3$, which shows ferrimagnetism. This is consistent with

	lattice constants (Å)	Magnetic state	ΔE/atom (eV)	DOS(E$_F$) (1/eV)
Cr:				
Experiment	$a = b = c = 2.885$Å	antiferromag[30]	–	0.444[95]
Calculated	$a = b = c = 2.882$Å	antiferromag	–	0.379
Cr$_3$Al:				
Experiment	$a = b = c = 2.949$Å[18]	antiferromag[62]	–	0.108[95]
Calculated				
• bcc solid solut. Cr$_{0.75}$Al$_{0.25}$	$a = b = c = 2.948$Å	antiferromag	0.042	0.240
• C11$_b$ Cr$_2$Al + bcc Cr	Cr$_2$Al: $a = b = 3.017$Å, $c = 2.899$Å; Cr: $a = 2.882$Å	antiferromag	0.039	0.192
• C11$_b$ Cr$_3$Al	$a = b = 2.979$ Å, $c = 2.915$Å	antiferromag	0.048	0.224
• D0$_3$ Cr$_3$Al	$a = b = c = 2.977$Å	ferrimag	0.075	0.207
• X-phase Cr$_3$Al	$a = b = c = 2.941$Å, 90.35° rhomb. distortion	antiferromag	0.000	0.076

Table 6.1: Calculated parameters for the four Cr$_3$Al structures and Cr, compared to experiment. ΔE/atom is shown relative to the minimum energy structure (X-phase Cr$_3$Al). The DOS(E$_F$) is shown per atom. The DOS/atom for the two-phase C11$_b$ Cr$_2$Al + Cr structure is the weighted average of the DOS/atom of the two structures.

previous calculations[81] and the well-known Heusler Slater-Pauling behavior.[43] Thus, the Cr$_3$Al experimental data are not consistent with the D0$_3$ structure.

The total energy per atom, relative to the minimum energy system, is shown in the third column. The X-phase structure has the lowest energy, suggesting that it is the low temperature stable phase for the Cr$_3$Al stoichiometry, as suggested in the proposed phase diagram (Figure 6.1(b)). The bcc solid solution, C11$_b$ Cr$_2$Al + bcc Cr two phase system, and C11$_b$ Cr$_3$Al structure have the next lowest energies, consistent with their being stable phases at higher temperatures. Finally, the D0$_3$ structure has a significantly higher energy, additional evidence that it does not occur experimentally, at any temperature, for Cr$_3$Al.

The bcc solid solution, C11$_b$ Cr$_3$Al, the C11$_b$ Cr$_2$Al + bcc Cr two phase system have some degree of disorder (in the case of the C11$_b$ Cr$_2$Al + bcc Cr two phase system the disorder comes in the form of a temperature-dependent solubility of Al in Cr and C11$_b$ Cr$_2$Al). This suggests that entropy of mixing drives the transition from the Cr$_3$Al X-phase. The energy difference between the X-phase Cr$_3$Al structure and the bcc solid solution is about 0.042 eV. In a model including only entropy of mixing, the order-disorder transition between these two structures should be about 600°C, within the range of the transition on the proposed phase diagram. The C11$_b$ systems are more difficult to model because of the lattice distortion and, in the case of the two phase system, the solubility of Al in Cr and in C11$_b$ Cr$_2$Al. The D0$_3$ structure has no more disorder than the X-phase structure and therefore should theoretically never occur in this system based on energy or entropy.

The fourth column in Table 6.1 shows the density of states (DOS) at E_F. It should be noted that because Cr and the Cr-Al alloys have a pseudogap at E_F due to the antiferromagnetism, the DOS is sharply varying near E_F and the exact value for DOS(E_F) depends somewhat on the input parameters of the calculation. The DOS curves are shown in Figure 6.7.

To compare the calculated values of DOS(E_F) to experimental values, we adjust experimental values for the Sommerfeld coefficient (γ) from the literature by the factor $(1 + \lambda)$. We used $\lambda = 0.34$, one of the reported values for Cr. This value was calculated based on the Sommerfeld coefficient from specific heat measurements and a previously accepted value for the DOS(E_F).[22, 21, 54, 78, 48] This is a fairly typical value for λ in the transition metals, however, reported values for λ in Cr vary.[86, 17, 4] No values of λ have been reported for Cr$_3$Al.

Our calculated DOS(E_F) for Cr is lower than the experimental value by 15%, showing the approximate level of error in DOS(E_F) calculations. X-phase Cr$_3$Al has the lowest DOS(E_F) by more than a factor of two, consistent with the observed nonmetallic behavior and closest to the experimental value based on the Sommerfeld coefficient for Cr$_3$Al.

An explanation for the decreased DOS(E_F) in X-phase Cr$_3$Al can be seen in the full band structure, shown in Figure 6.8. The band structure is calculated in the rhombohedral Brillouin zone, shown in the inset. For reference, point T occurs along the bcc [111] axis (the long axis of the rhomboid unit cell in real space). The band structure appears semimetallic, with an electron band barely crossing E_F at point F and a hole band barely crossing at point T. The electron band crosses E_F more significantly, explaining the observed negative Hall constant.[18] Although the total DOS(E_F) for the X-phase is only 2-3 times lower
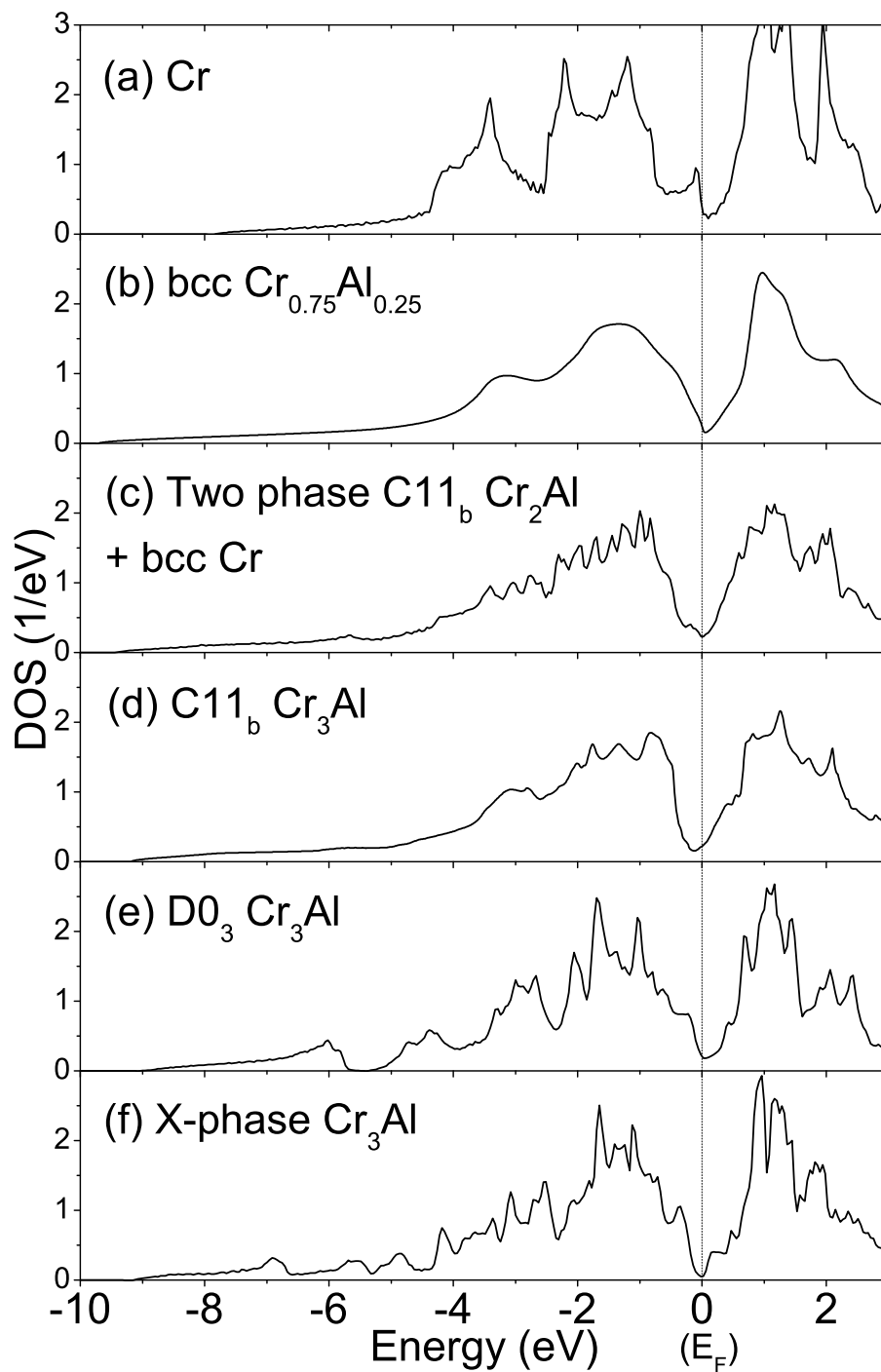
Figure 6.7: Calculated DOS/atom of Cr and the Cr_3Al structures. The DOS/atom for the two-phase $C11_b$ Cr_2Al + Cr structure is the weighted average of the DOS/atom of the two structures.
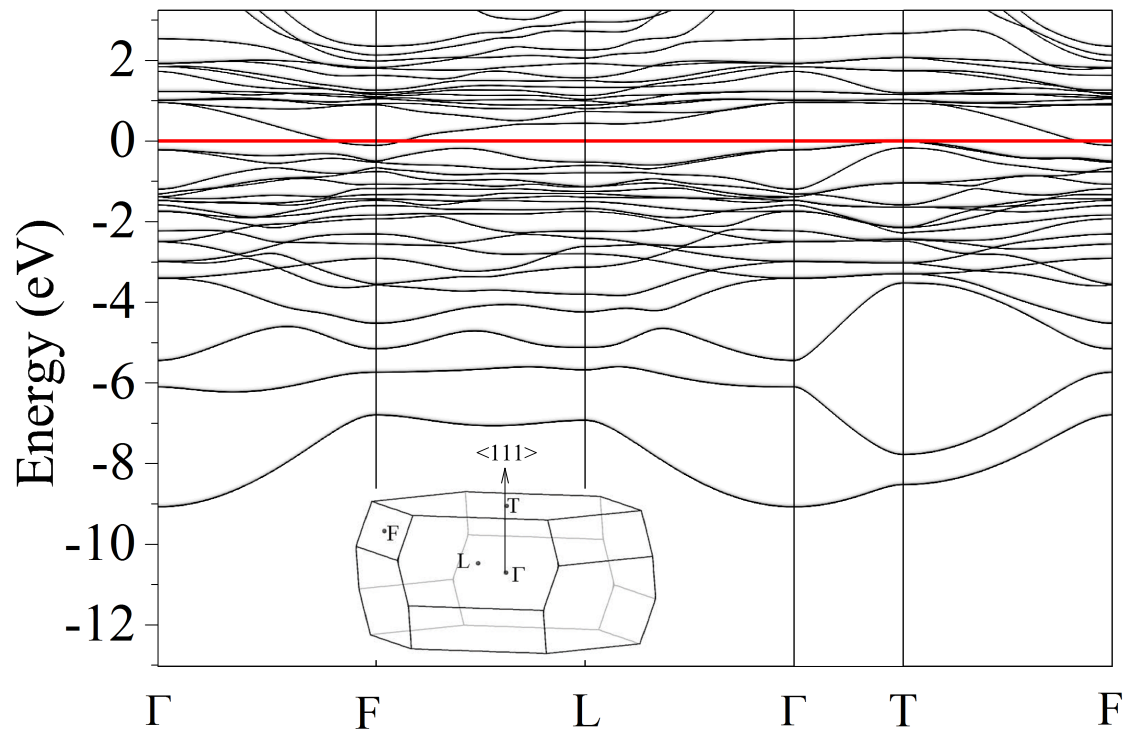
Figure 6.8: Calculated band structure of X-phase Cr$_3$Al, in the rhombohedral Brillouin Zone (inset).

than the competing structures, the semimetallic band structure leads to flat bands which are more likely to localize electrons.

6.7   Discussion

The semimetallic band structure in X-phase Cr_3Al is possible because the primitive unit cell of the X-phase, shown in Figure 6.2(f), contains a total of 8 atoms, or Cr_6Al_2, for a total of 42 (an even number) valence electrons per unit cell. This aspect of the X-phase structure sets it apart from the other structures, which, although they may have a low $DOS(E_F)$, must have bands crossing E_F due to an odd number of valence electrons.

The experimental observations of Cr_3Al are all consistent with a semimetallic band structure: the electronic contribution to the specific heat is nonzero, and the electrical resistivity increases with decreasing temperature as algebraically rather than exponentially. This can be a sign of localization phenomenon with an imcomplete band gap. In addition, the photoemission measurements in Chapter 5 have shown that, while the valence band is shifted about 95 meV below E_F, there is still nonzero photoemission intensity at zero binding energy, which could be due to states at E_F or simple experimental broadening.

It is important to note that DFT calculations often underestimate the band gap in materials, sometimes showing overlapping bands even in materials known to have a full band gap.[84] It is possible that a perfect crystal of X-phase Cr_3Al would be a true semiconductor. However, real samples thus far show the X-phase occurring in very small domains presumably separated by anti-phase boundaries[24], which could smear the band edges. Currently, the electronic properties of the available samples, and the available theory, can be described by a semimetal model. However, it would be interesting to pursue this question further both experimentally and theoretically, by growing samples with longer-range X-phase ordering, and by performing additional calculations, for example using a DFT+GW method or hybrid functional.

6.8   Conclusion

In summary, we used both experimental thin film growth methods and theoretical DFT calculations to show that the semiconductor-like behavior observed in Cr_3Al can be explained by X-phase chemical ordering. Our experimental data correlates a transition from nonmetallic to metallic transport behavior around $400°C$ growth temperature with the previously proposed structural phase transition (X-phase $\rightarrow$ $C11_b$) occurring around the same temperature. Theoretically, the proposed X-phase is found to be the lowest energy structure of those considered, implying it should be the equilibrium structure occurring in nature. It possesses a semimetallic type band structure which explains the observed transport behavior. Further work will probe the role of the antiferromagnetism in the semiconducting behavior of $Cr_{1-x}Al_x$.

Chapter 7

Magnetism in Cr_3Al and relation to semiconducting behavior

7.1 Introduction

$Cr_{1-x}Al_x$ exhibits previously unexplained semiconductor-like electronic transport behavior around the stoichiometry Cr_3Al. Our recent photoemission study (Chapter 5) showed a narrow gap or pseudogap at E_F in a $Cr_{0.80}Al_{0.20}$ thin film. A high resistivity, up to 3600 $\mu\Omega$-cm, and a large negative Hall constant both peak at $x = 0.25$.[18, 91] In addition, the electronic contribution to the specific heat reaches a minimum at $x = 0.25$.[95]

These signatures point towards an ordered Cr_3Al structure causing the anomalous behavior. Chapter 6 highlighted the role of chemical ordering in the semiconducting behavior of Cr_3Al, using both theoretical and experimental methods. Our theoretical calculations showed that an ordered "X-phase" Cr_3Al, a chemically ordered, rhombohedrally distorted Cr_3Al structure, could explain the semiconducting behavior. Experimentally, the X-phase has only been observed by transmission electron microscopy (TEM), with nm-size domains separated by antiphase boundaries causing long-range order to be disrupted.[24] Thus, the X-phase ordering in Cr_3Al is better described as short- or medium-range chemical ordering.

Our experimental results showed that the electronic properties of Cr_3Al thin films are highly dependent on growth conditions. Films grown below 400°C are semiconducting, while films grown above 400°C are metallic. This behavior can be explained by the proposed 400°C boundary in the Cr-Al phase diagram, with the X-phase (semiconducting) structure forming below this boundary and the $C11_b$ (metallic) structure forming above it (see Figure 6.1).[24] The $C11_b$ structure, also known as the $MoSi_2$ structure, is the equilibrium phase for the Cr_2Al stoichiometry, which is known to be metallic. However, in thin films at the Cr_3Al concentration, the $C11_b$ structure can be stabilized as a single-phase, off-stoichiometry compound by growth above 400°C. These results showed the importance of X-phase chemical ordering to the semiconducting behavior.

The role of magnetism in the electronic properties of Cr_3Al is intriguing and still uncertain. Cr is antiferromagnetic, with a spin density wave (SDW) incommensurate with the lattice. The incommensurate SDW is very sensitive to perturbation by small amounts of dopant, pressure, or disorder, as seen in Chapter 3.[30, 31] The addition of 3 at. % Al

or more causes the SDW to become commensurate with the lattice, like a simple antiferro-magnet, shown in Figure 7.1(a).[31] The commensurate antiferromagnetism is maintained up to about 50 at. % Al, including the C11$_b$ Cr$_2$Al stoichiometric compound. The Neel temperature and the magnetic moment on the Cr atom both increase with the addition of Al, to around 900K and above 1 μ_B for $x = 0.20$.[62, 72] However, the magnetic moment of the Cr$_3$Al stoichiometry has never been measured.

Given the clear influence of chemical ordering on the electronic behavior, the influence on magnetic behavior must also be considered. While the electrical resistivity[18, 91], Neel temperature (from susceptibility)[72], and magnetic moment[62] have all been measured for bulk Cr$_{1-x}$Al$_x$ alloys, these measurements were performed by different researchers on different samples which may very well have had different properties. In fact, the authors reporting susceptibility results noted a difference between heating and cooling measurements, suggesting sample annealing occurred during measurement which affected the properties.[72] In this chapter, we present neutron diffraction results on structurally and electrically well-characterized Cr$_3$Al samples in a comprehensive study of the magnetism in Cr$_3$Al.

Previously, the antiferromagnetism has been suggested as an explanation for the semiconducting behavior. In Cr, the antiferromagnetism splits the d band into two d sub-bands, one below and one above the Fermi energy (E_F). This results in the well-known pseudogap at E_F, with a decreased density of states (DOS) in antiferromagnetic compared to paramagnetic Cr. However, enough states remain at E_F for Cr to remain a metal[30] It has been suggested that, with the addition of Al, the d sub-bands are shifted apart, further decreasing the DOS and leading to the semiconducting behavior.[18] However, this model is lacking, because most electrical conduction takes place in the s band, which should be unaffected by shifting d sub-bands.

To determine the role of magnetism in the anomalous transport behavior of Cr$_3$Al, it is desirable to test the statement:

$$\text{``If Cr}_3\text{Al is magnetic, it is semiconducting''}, \tag{7.1}$$

and its inverse,

$$\text{``If Cr}_3\text{Al is not magnetic, it is not semiconducting''}. \tag{7.2}$$

Theoretical calculations can help test these statements. Early calculations of the electronic structure of Cr$_{1-x}$Al$_x$ did not take into account the antiferromagnetism, and thus did not show the split d sub-bands in the DOS.[3] The calculations not only showed a high electronic DOS for Cr, in disagreement with specific heat results, but they showed an increasing DOS with the addition of Al, rather than decreasing as was seen from specific heat,[95] and as would be expected based on the observed semiconductor-like transport behavior.

In contrast, our recent study of chemical ordering in Cr$_3$Al included magnetism in the theoretical calculations and found a pseudogap in the DOS. Clearly, magnetism is an important factor which should not be neglected. The current work further tests these statements by comparing magnetic and nonmagnetic calculations side by side, finding that magnetism is essential to the formation of a pseudogap in Cr$_3$Al.
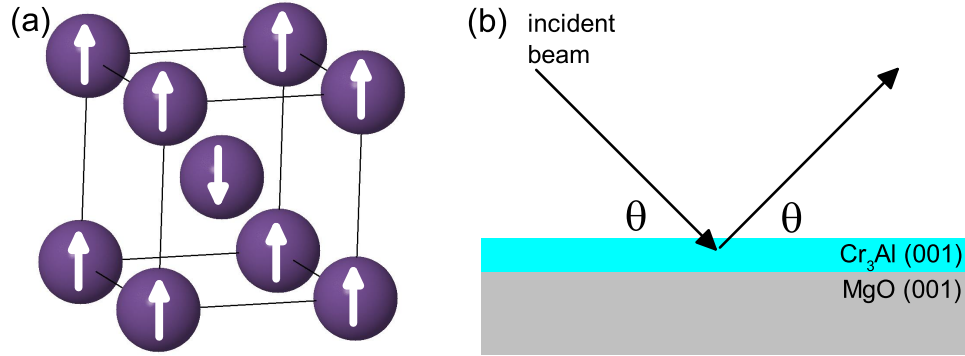
Figure 7.1: (a) Commensurate spin-density wave (simple antiferromagnetism) in the bcc structure. (b) Experimental setup for x-ray and neutron diffraction experiments.

Experimentally, however, statements 7.1 and 7.2 are difficult to test. Two different studies have attempted it by measuring the resistivity below and above the Neel temperature, drawing different conclusions.[18, 105] Because the Neel temperature is so high, and the transport behavior is indicative of a narrow gap semiconductor or semimetal, the behavior is already practically metallic near the Neel temperature. In addition, some feature in the resistivity is expected to occur due to the magnetic transition (as is seen in Cr); this can be hard to separate from a semiconducting-to-metal transition.[30] Thus, the results are open to interpretation.

Our work on Cr_3Al thin films provides another path for experimentally studying the relationship between the magnetism and semiconducting behavior, because we were able to grow both semiconducting and metallic Cr_3Al samples by varying the substrate temperature (see Chapter 6). While experimentally testing statements 7.1 and 7.2 has proven difficult, the converse and contrapositive of statement 7.1 can be tested:

$$\text{“If } Cr_3Al \text{ is semiconducting, it is magnetic”}, \tag{7.3}$$

and

$$\text{“If } Cr_3Al \text{ is not semiconducting, it is not magnetic”}. \tag{7.4}$$

The current work tests statements 7.3 and 7.4 using neutron diffraction on a semiconducting (X-phase Cr_3Al) and a metallic ($C11_b$ Cr_3Al) thin film, and finds that both semiconducting and metallic Cr_3Al are magnetic.

In this chapter, we use a combination of neutron diffraction and density functional theory (DFT) to help elucidate the role of magnetism in the anomalous semiconducting behavior of Cr_3Al.

7.2 Experimental Methods

Two thin films of Cr_3Al were used for the neutron diffraction study: one X-phase Cr_3Al sample (grown at 300°C), and one $C11_b$ Cr_3Al sample (grown at 600°C). These films
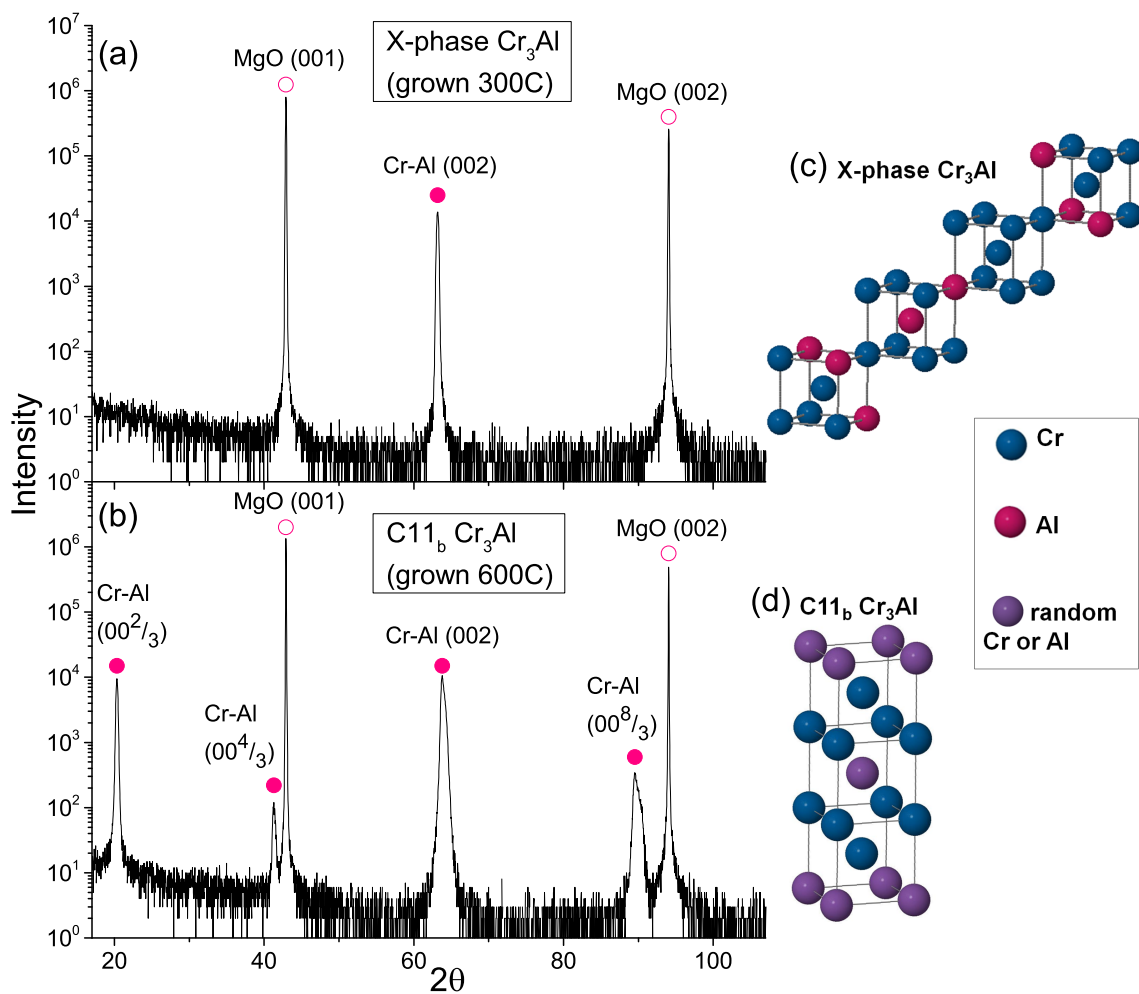
Figure 7.2: X-ray diffraction of two Cr_3Al thin films grown at 300°C and 600°C. Filled circles indicate diffraction peaks from the substrate, while empty circles indicate diffraction peaks from the sample.

have semiconducting and metallic electronic transport behavior, respectively, due to their differing chemical ordering.

The films were grown epitaxially on MgO(001) substrates by co-deposition of Cr from an e-beam source and Al from an effusion cell at a rate of 0.4 Å/s and a base pressure of 7×10^{-9} Torr. The thickness of these films was 0.95μm and 1.00μm, respectively. The large thickness was chosen to increase the neutron diffraction intensity.

Cr(001) is known to grow epitaxially on MgO(001). The MgO lattice constant is 4.211Å, or about $\sqrt{2}$ larger than that of Cr. Thus, the Cr lattice grows $45°$ rotated compared to the substrate (Cr[110] || MgO[010]). For pure Cr, the lattice mismatch for this epitaxial relation is 3.9%, while the addition of Al increases the lattice constant and improves the mismatch to 0.9% at the Cr_3Al stoichiometry. Epitaxy was verified in-situ by reflection high energy electron diffraction (RHEED) which showed a streaky pattern and ex-situ by x-ray diffraction (XRD) which showed four-fold symmetry of the $\{011\}$ peaks in an azimuthal scan at $45°$ from normal. In addition, only the bcc (001) orientation is seen in XRD $\theta - 2\theta$ scans, shown in Figure 7.2(a-b).

The XRD results also show the type of structural ordering in each sample. Cr orders in the bcc structure, and both X-phase Cr_3Al and $C11_b$ Cr_3Al are types of chemical ordering based on the bcc structure. The X-phase has a rhombohedral unit cell with a slight rhombohedral distortion, while the $C11_b$ structure has a tetragonal unit cell with a tetragonal distortion. The two structures are shown in Figure 7.2(c-d). All Cr-Al diffraction peaks discussed here are indexed in the cubic zone based on a 2-atom basis (bcc), as is customary for Cr and its alloys (Figure 7.1(a)).

The film grown at $300°$C displays a single Cr-Al (002) peak, due to the bcc structure. Our previous work strongly suggests that these films have short- to medium-range X-phase chemical ordering, but this is not observable by XRD. The rhombohedral unit cell of the X-phase, shown in Figure 7.2(c), does not lead to superlattice peaks in the (001) plane, so that no additional peaks should be seen in a typical out-of-plane XRD scan. However, the existence of the X-phase in small nanodomains separated by antiphase boundaries would likely completely broaden any in-plane superlattice peaks in any case.

The film grown at $600°$C displays the bcc Cr-Al (002) peak, as well as $(00\frac{2}{3})$, $(00\frac{4}{3})$, and $(00\frac{8}{3})$ superlattice peaks indicating $C11_b$ ordering. As shown in Figure 7.2(d), the $C11_b$ unit cell contains three bcc unit cells, with layers of Cr and Al atoms (Cr-Cr-Al-Cr-Cr-Al...). This structure is the equilibrium phase for the Cr_2Al stoichiometry, with the single phase region for this phase extending across the range $x \sim 0.28 - 0.35$ (see Figure 6.1).

For the Cr_3Al stoichiometry, a two-phase $Cr_2Al + Cr$ region is shown in the phase diagram, at least above $400°$C, as discussed in Chapter 6. However, no evidence of phase separation is seen in the XRD data for our film. Phase separation would lead to a splitting of the Cr-Al (002) bcc peak, as Cr and Cr_2Al have different lattice constants; this is not seen.

In this film, we observe an off-stoichiometry, single-phase $C11_b$ Cr_3Al compound, or $Cr_2(Al_{1-\delta}Cr_\delta)$, with Cr presumably substituting onto the Al sites. This is supported by the decrease in tetragonal distortion in this film compared to $C11_b$ Cr_2Al ($a = 2.95$Å, $c = 8.75$Å in our film, $a = 3.001$Å, $c = 8.637$Å in bulk Cr_2Al[72]). As discussed above, the occurrence of single phase $C11_b$ at the Cr_3Al stoichiometry does not appear on the

	Sample	Crystal structure	Magnetic state	Magnetic moment (μ_B)	Neel temp (K)
Cr	bulk	bcc	incommensurate SDW (Ref. [30])	0.43 (Ref. [30])[a]	311 (Ref. [30])
Cr_3Al	bulk	unknown	simple antiferromag (Ref. [62])	1.07 (Ref. [62])[b]	913 (Ref. [72])
	300°C grown film	X-phase	simple antiferromag (this work)	1.06±0.02 [c] (this work)	>578 (this work)
	600°C grown film	$C11_b$	simple antiferromag (this work)	0.86±0.03 (this work)[d]	>639 (this work)
Cr_2Al	bulk grown film	$C11_b$	simple antiferromag (Ref. [8])	0.92±0.02 (Ref. [8])[e]	598 (Ref. [8])

[a]rms moment of incommensurate SDW, measured at 4.2K

[b]moment of Cr_3Al stoichiometry not measured; value is for closest stoichiometry ($Cr_{0.80}Al_{0.20}$), measured at room temperature

[c]measured at 60K

[d]measured at 100K

[e]measured at 4.2K

Table 7.1: Experimental magnetic state, moment, and Neel temperature for Cr, Cr_3Al, and Cr_2Al, for our films and bulk samples from literature.

equilibrium phase diagram, but nonequilibrium structures are often caused by thin film growth methods.

The neutron diffraction measurements were performed at ANSTO on the TAIPAN beamline, a triple-axis spectrometer. The neutron wavelength was 2.35Å. Measurements were performed at a range of sample temperatures from 60-639K using a cryostat with a closed cycle helium refrigerator and heater.

Alignment was performed on the Cr-Al (002) and (011) peaks. The alignment was checked at each temperature, and realignment was performed if necessary. Diffraction was measured as a function of the wavevector q, in the out of plane direction (see Figure 7.1(b)) around the expected Cr-Al magnetic (001) and structural (002) diffraction peaks.

7.3 Experimental Results

Figure 7.3 shows the magnetic (001) and structural (002) neutron diffraction peaks. The structural (002) peak is also seen in XRD (Figure 7.2), and the lattice constants match well to those found by XRD. The Cr_3Al (002) peak lies near the Al (022) peak, which is seen here due to the Al sample holder used in the neutron experiments. Note that Al (022) is not seen in XRD (Figure 7.2), confirming the Al (022) peak does not come from the sample.

The (001) peak is a disallowed bcc structural peak, and is not seen in XRD. Thus its
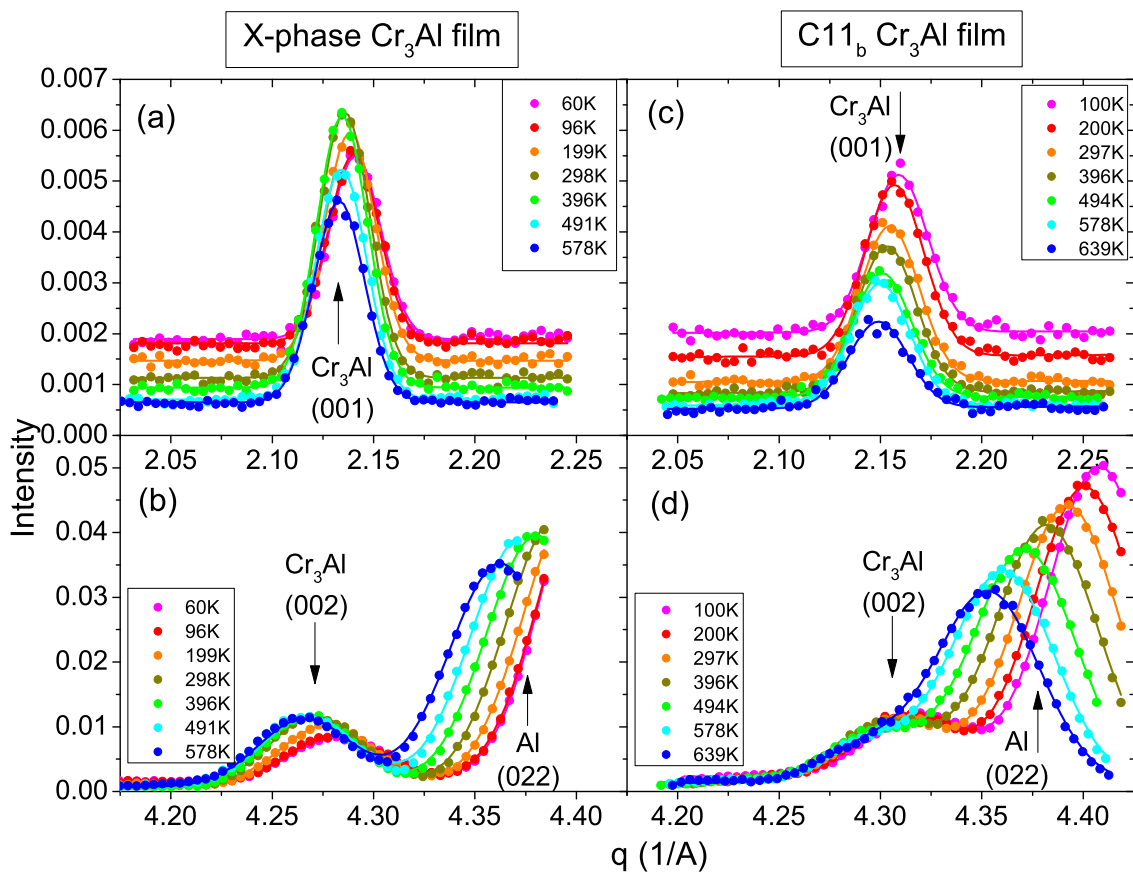
Figure 7.3: Neutron diffraction peaks of two Cr$_3$Al films grown at 300°C and 600°C.
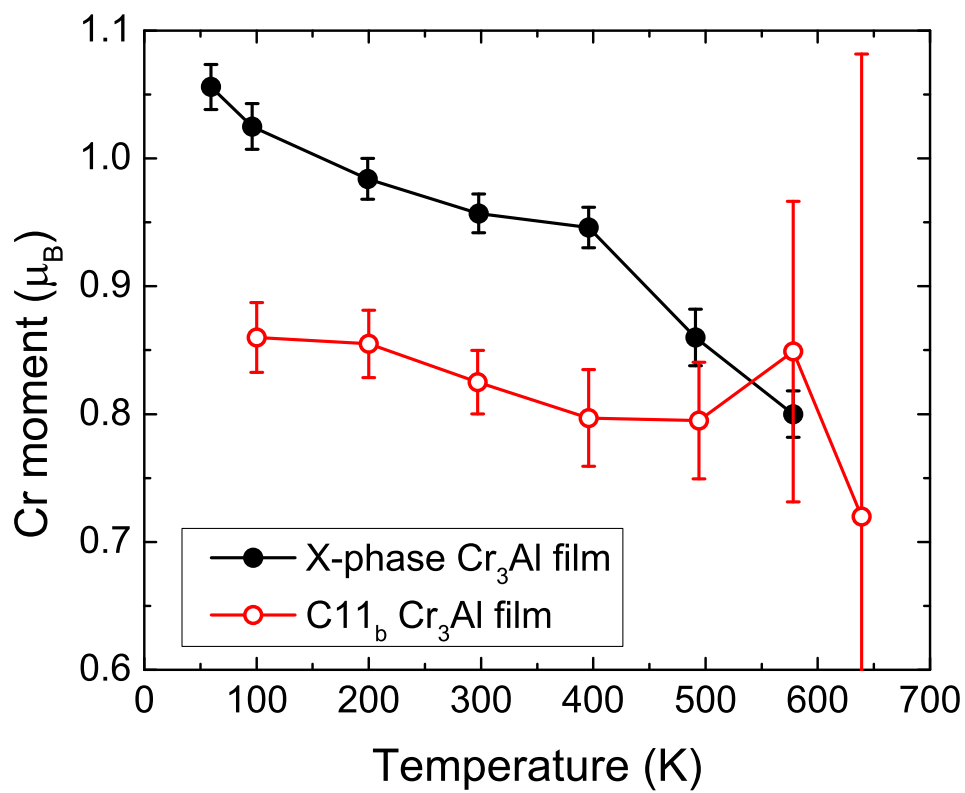
Figure 7.4: Magnetic moment vs. temperature from neutron diffraction of two Cr_3Al thin films grown at 300 and 600°C

existence is confirmation of antiferromagnetic ordering, specifically a commensurate SDW or simple antiferromagnetism, in both samples. In contrast, the incommensurate SDW seen in pure Cr would result in multiple satellite peaks around the (001) peak,[30, 38] which are not seen here.

It is necessary to confirm that the (001) peak is not a result of $\lambda/2$ contamination of the neutron beam. The neutron beam was passed through a graphite filter to remove any contamination. A check was performed of the MgO substrate (002) peak and disallowed (001) peak, and found $\lambda/2$ contamination at the level of 0.2%, negligible compared to our measured (001) peaks which are about 50% of the (002) intensity.

The magnetic moment on the Cr atoms was calculated from the relative intensities of the structural and magnetic peaks. Tracking the intensity of the magnetic peak alone is not accurate enough because total intensity variations may occur due to differing alignment as the temperature changes. Thus the structural peak must be remeasured at each temperature as well. During data analysis, the peak intensities were corrected by a Debye-Waller factor for temperature, a Lorentz factor for angle θ, and a geometrical factor taking into account the thin film geometry and neutron absorption.[12]

Because magnetic scattering only occurs for the component of the moment that is normal to the scattering vector, an assumption must be made about the direction of moment in the samples. In pure Cr, the moment aligns along the cube axes. We assume an isotropic distribution of domains with moments along the three cube axes, so that $\frac{2}{3}$ of the domains contribute to diffraction of the neutron beam. Alternatively, Cr_2Al has been shown to have the Cr moment direction along the bcc <111> axis, which would result in an equivalent factor in the moment calculation. Using either of these assumptions, the resulting Cr moment as a function of temperature is shown in Figure 7.4.

The primary conclusion from this data is that the antiferromagnetism in both Cr_3Al samples is robust, extending to the highest temperatures measured (578K and 639K in the X-phase and $C11_b$ samples, respectively). This is not expected, as we showed in Chapter 3 that thin film growth can have serious consequences on the magnetism of thin films. The temperature dependence of the moment in both samples is slight, suggesting that the Neel temperature is significantly higher than the temperatures measured. The large error in the high temperature data points of the $C11_b$ sample is due to the interference of the Al (022) peak in calculating the intensity of the Cr-Al structural (002) peak (see Figure 7.3).[1]

Table 7.1 tabulates experimental magnetic parameters of Cr and Cr-Al compounds from the literature along with our results. This work is the first measurement of the magnetic moment value in Cr_3Al. The closest comparison is a bulk $Cr_{0.80}Al_{0.20}$ sample which is reported to have a 1.07 μ_B moment on the Cr atom.[62] Our X-phase Cr_3Al film compares well, with a moment of 1.06 ± 0.02 μ_B. However, the $C11_b$ film has a significantly lower moment.

This can be explained by the differing chemical ordering in the two films. Although the published research presenting the magnetic moment for bulk Cr-Al alloys does not

---

[1]The Al peak shifts significantly towards the Cr_3Al peak at higher temperatures due to the large thermal expansion of Al. In addition, the Cr_3Al (002) peak is at a higher q in the 600°C sample than the 300° sample due to the previously discussed tetragonal distortion.

discuss significant structural characterization, other bulk Cr_3Al samples have been shown to be X-phase and semiconducting.[24, 18, 91] The $C11_b$ Cr_3Al film, on the other hand, has a clearly nonequilibrium structure that has not been observed in bulk at the Cr_3Al stoichiometry.

$C11_b$ Cr_3Al may be expected to behave more like $C11_b$ Cr_2Al, which is a known metallic antiferromagnet. Bulk Cr_2Al has a lower magnetic moment[8], 0.92 μ_B, much closer to that of our $C11_b$ Cr_3Al film, at 0.86 μ_B. However, bulk Cr_2Al also has a lower Neel temperature[8], 598K, while our film shows no hint of the Neel transition up to 639K. This nonequilibrium film thus has magnetic behavior between that of bulk Cr_3Al and Cr_3Al.

The conclusions of these experiments are that statement 7.3 is true and 7.4 is false. Magnetism occurs in Cr_3Al regardless of the electronic transport properties.

7.4 Theoretical Methods

DFT calculations were done using the AkaiKKR code, a full-potential DFT Green's function approach based on the Korringa-Kohn-Rostoker multiple-scattering technique.[2, 71, 70] The scalar relativistic approximation was used and disorder in the bcc solid solution was treated using the coherent potential approximation (CPA).[112, 1] The number of irreducible k points used for Brillouin zone integration was between 3009 and 3276 for the different structures. The generalized gradient approximation (GGA) was used to approximate the exchange-correlation energy[94].

Calculations were done for pure Cr, four different possible Cr_3Al structures, and for Cr_2Al in the $C11_b$ structure. The Cr_3Al structures considered were: X-phase Cr_3Al, a chemically ordered, rhombohedrally distorted Cr_3Al structure, with ordering along the <111> direction, proposed by a TEM study[24] and suggested by Chapter 6 to be a contributing factor to the semiconducting behavior, and shown in Figure 7.2(c); a bcc solid solution of $Cr_{0.75}Al_{0.25}$; the off-stoichiometric $C11_b$ Cr_3Al structure observed experimentally in our high temperature grown films; and the well-known $D0_3$ (binary Heusler) structure. $C11_b$ Cr_2Al is a chemically ordered, tetragonally distorted structure, known to be metallic. These structures are all discussed in further detail in Chapter 6. Each structure was treated with a calculation including magnetism (two electron spins), and one not including magnetism (one electron spin).

7.5 Theoretical Results

The magnetic parameters obtained from the calculations are tabulated in Table 7.2. All structures considered are found to be magnetic.

Pure Cr was treated in the basic bcc unit cell, forcing a commensurate SDW (simple antiferromagnetism) rather than the incommensurate SDW seen experimentally. The incommensurate SDW in Cr not only requires a computationally difficult large unit cell but is, as of yet, not found to be the minimum energy state in current DFT calculations.[53]

In Cr_2Al, the Cr atoms are also aligned in a simple antiferromagnetic configuration, with negligible moment on the Al atoms.

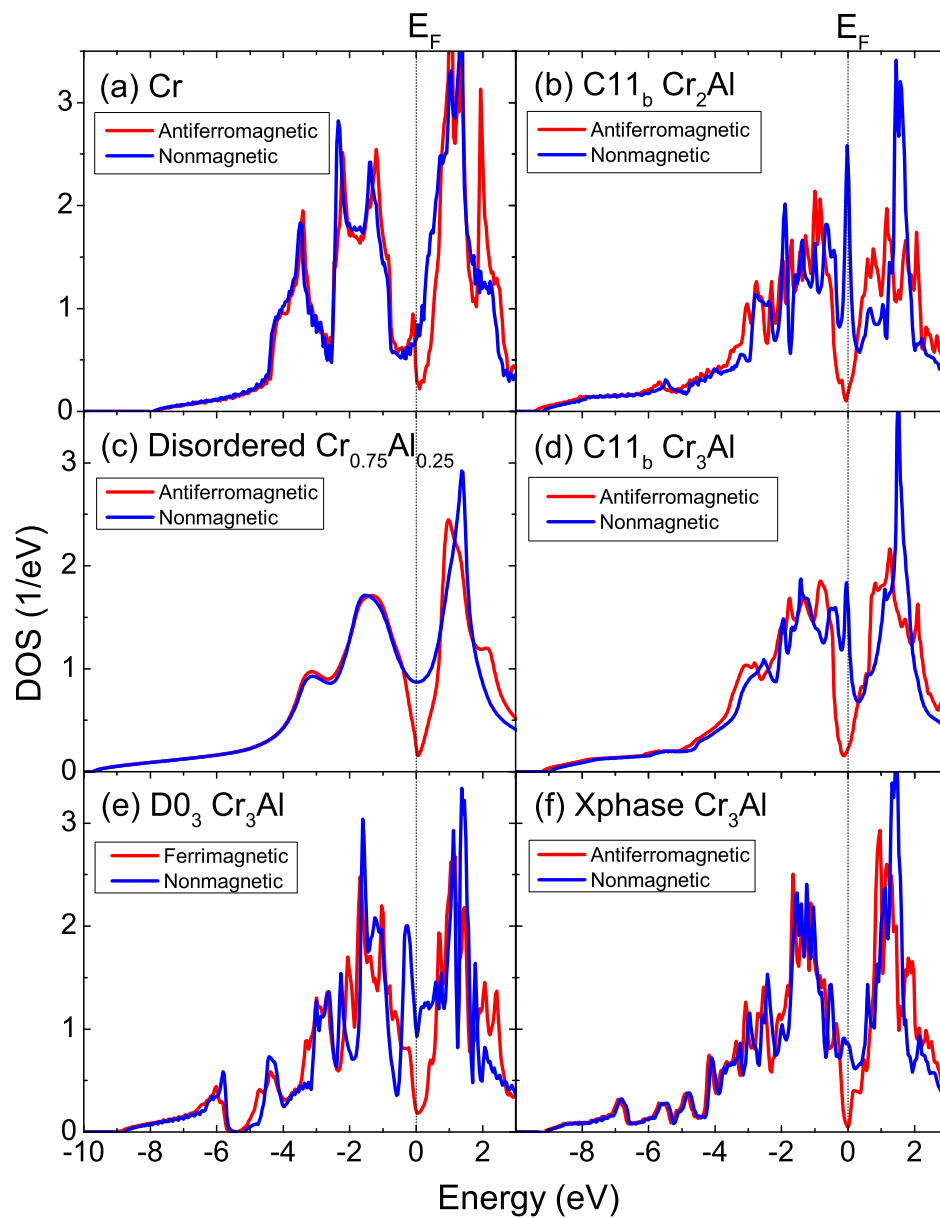The bcc solid solution, $Cr_{0.75}Al_{0.25}$, is also found to have the commensurate SDW.

Figure 7.5: Theoretical density of states of Cr₃Al for four different types of chemical ordering, and Cr for comparison. The calculations compare magnetic and nonmagnetic cases.
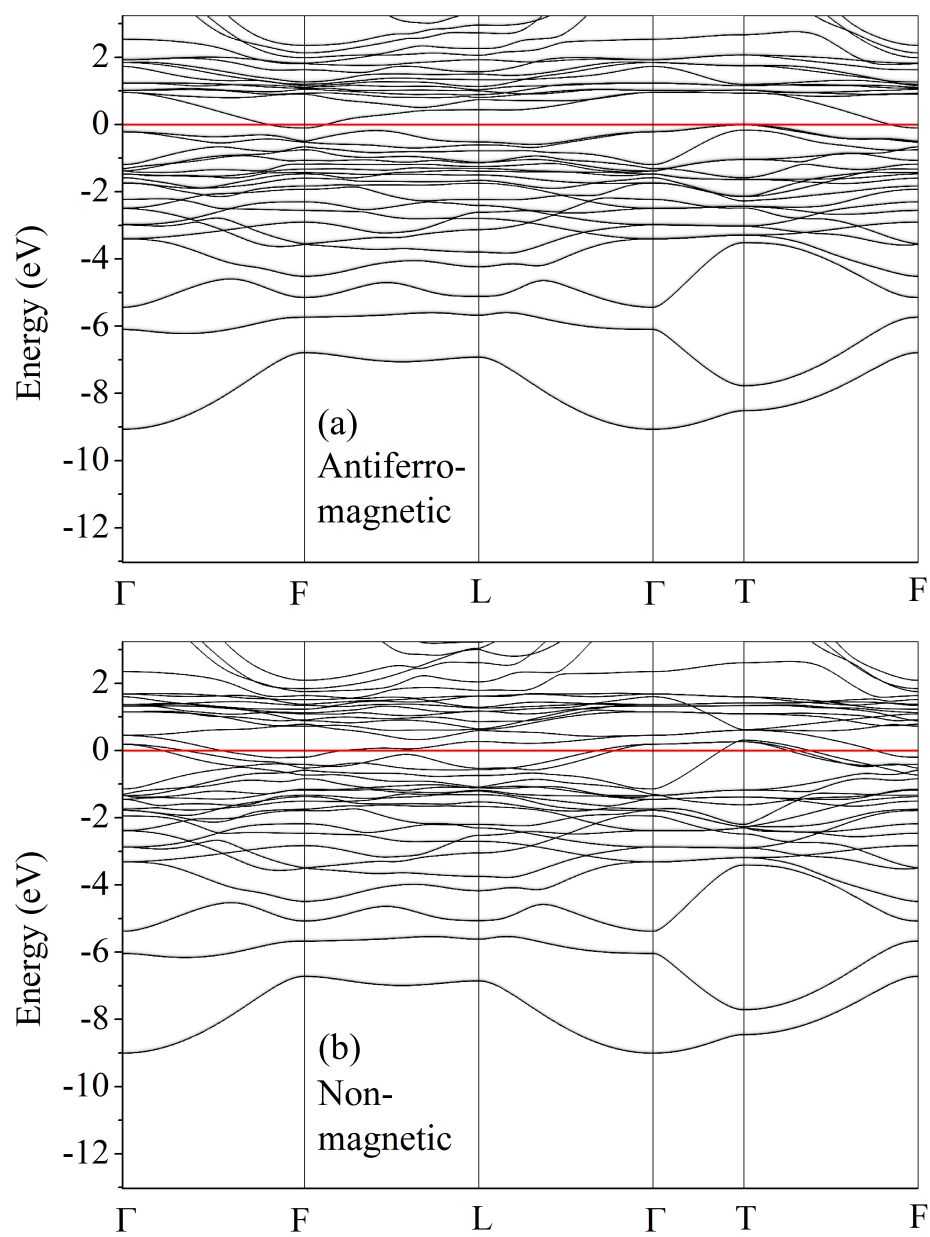
Figure 7.6: Band structure for Cr₃Al with X-phase ordering, for both antiferromagnetic and nonmagnetic cases.

Stoichiometry	Crystal structure	Magnetic state	Magnetic moment (μ_B)
Cr	bcc	simple antiferromag[a]	1.05
Cr$_3$Al	bcc solid solution	simple antiferromag	1.68
	C11$_b$	commensurate SDW	1.76, 1.74[b]
	D0$_3$	ferrimag[c]	↑2.16, ↑2.16, ↓1.75
	X-phase	commensurate SDW[d]	1.65, 1.49, 1.36[e]
Cr$_2$Al	C11$_b$	antiferromag	1.82

[a]assumption of the bcc unit cell forces simple antiferromagnetism
[b]moment of Cr atom on a Cr site and substituted onto Al site, respectively
[c]also see Ref. [81]
[d]wavelength of SDW is length of rhombohedral unit cell
[e]six Cr atoms in primitive X-phase unit cell have ↑ and ↓ of each of these three moment values

Table 7.2: Theoretical magnetic state and moment for Cr, Cr$_3$Al in four structures, and Cr$_2$Al from our calculations.

C11$_b$ Cr$_3$Al is also found to be antiferromagnetic. Although there are two different Cr sites (one Cr site and one site for Cr substituted onto the Al sublattice), the moments for these two sites are extremely similar.

D0$_3$ Cr$_3$Al is found to be ferrimagnetic, consistent with previous calculations[81] and with the expected Slater-Pauling behavior.[43] However, this structure has never been observed experimentally in Cr$_3$Al.

The X-phase Cr$_3$Al unit cell contains 6 Cr atoms and 2 Al atoms, aligned along the bcc <111> direction. The Cr atoms are antiferromagnetically aligned, but the distinct atoms have slightly different moments. This is a longer-wavelength SDW than that seen in simple antiferromagnetism, but it is still a commensurate SDW since the wavelength of moment modulation is a multiple of the lattice constant. The effect of this modulation of moment on the neutron diffraction peaks is unclear, as this structure only seems to order over the short- to medium-range.

The resulting moments from these calculations are all larger than is experimentally seen. The large calculated Cr moment is consistent with calculations in the literature and is due to overestimation of the moment by the GGA approximation.[53] However, the trend of an increased moment in Cr-Al alloys/compounds compared to Cr is consistent with experiment.

The DOS for each structure is shown in Figure 7.5, with the results from magnetic and nonmagnetic calculations compared. The DOS of pure Cr shows the well-known phenomenon of an antiferromagnetic pseudogap opening up at the Fermi energy E_F, due to an effective doubling of the lattice constant due to the magnetic ordering. This pseudogap results in a significant decrease in the DOS(E_F) of Cr; however states still remaining at E_F lead to the well known metallic behavior of Cr.[30]

Figure 7.5 shows the same phenomenon for all Cr-Al alloys/compounds considered. In all cases, the DOS(E_F) is significantly decreased by the effect of magnetism. This

observation alone cannot explain the semiconducting behavior experimentally seen in Cr_3Al, as in the case of Cr and Cr_2Al the antiferromagnetic state occurs but the material is clearly still metallic. However, it proves that magnetism is an essential ingredient in the semiconducting behavior of Cr_3Al.

In Chapter 6, we looked at chemical ordering as one route to explain the semiconducting behavior in Cr_3Al. The X-phase Cr_3Al structure has the lowest $DOS(E_F)$ of those considered. The band structure, shown in Figure 7.6(a) shows a semimetallic type band structure with a pseudogap. The nonzero $DOS(E_F)$ is the result of slightly overlapping flat band edges at E_F, which are more easily affected by localization than wider bands. Figure 7.6(b) shows the band structure of X-phase Cr_3Al when magnetism is not included in the calculation. Antiferromagnetic X-phase Cr_3Al clearly shows the pseudogap at E_F, while nonmagnetic Cr_3Al has several bands crossing E_F, suggesting a metal.

7.6   Conclusion

The results of Chapter 6, along with the current Chapter, suggest that both chemical ordering and magnetism play an important role in the anomalous transport behavior of Cr_3Al.

Our neutron diffraction results show that while manipulation of growth conditions leads to nonequilibrium structure and either semiconducting or metallic behavior, the antiferromagnetism is quite robust. In this case, the main difference between the two Cr_3Al films, one semiconducting and one metallic, is the chemical ordering and not the magnetism. This highlights the importance of chemical ordering and structure to the semiconducting behavior in Cr_3Al.

The theoretical results presented here show clearly that, for any Cr-Al structure, magnetism is a necessary ingredient for the creation of a pseudogap at E_F. Destruction of magnetism in Cr_3Al would likely result in a return to metallic behavior if it could be achieved.

Cr_3Al is a unique material where structure and magnetism come together to manipulate the band structure in such a way that a pseudogap is created, leading to semiconducting transport behavior.

Chapter 8

Conclusion

This thesis has studied the unique properties of Cr and Cr-Al alloys. Both Cr and Cr-Al alloys have sharp features in their d bands which affect their magnetic properties and ultimately lead to anomalous electrical transport. Although the specifics of the element and the alloy are quite different, they are united by the sensitivity of their magnetic and electronic states to external perturbation. This thesis in particular focused on the effects of nanoscale structure, in particular as a result of thin film growth techniques, on both the magnetism and the electronic transport properties of Cr and Cr-Al.

In Cr, we saw that disorder and stress, typical results of thin film growth, strongly affected the behavior of the spin-density wave, with different samples taking on the incommensurate, commensurate, or mixed spin-density wave depending on their deposition conditions. We used our results to create a low temperature magnetic phase diagram for Cr in the stress-disorder plane. Furthermore, we found that the disorder caused by thin film growth, in concert with the spin-density wave gap, produced anomalies in the electrical resistivity due to resonant scattering, such as increased residual resistivity and a resistivity minimum at low temperature.

In Cr-Al alloys, we found that the anomalous electrical and magnetic properties previously seen in bulk samples - semiconductor-like transport behavior and antiferromagnetism with an extremely high Neel temperature - were reproducible in thin film form, albeit intricately dependent on deposition conditions and ultimately structure. We used such a film to directly observe a narrow gap or pseudogap at the Fermi energy through photoemission measurements. The use of nonequilibrium thin film growth allowed us to probe the anomalous properties more deeply as a function of the chemical ordering and structure of the alloys. The combination of thin film growth and density-functional theoretical calculations allowed us to conclude the likely origin of the anomalous transport behavior: both chemical ordering of the X-phase Cr_3Al variety and the antiferromagnetic pseudogap are necessary ingredients to produce the gap at the Fermi energy and semiconductor-like transport behavior.

As common in research, this thesis has opened as many questions as it has closed. The work on the resistivity of Cr thin films clearly showed an effect of disorder, but further studies should attempt introduction of defects in a more controlled manner, such as ion bombardment. This work is already underway in our lab. The results on Cr-Al point to

the importance of short- to medium-range chemical ordering of the X-phase type, which is notoriously difficult to detect in thin films due to broadening of diffraction peaks and the small amounts of material involved. At this point, direct measurement and more complete understanding of the X-phase as it occurs in real samples would be hugely helpful. Finally, there remains the question of whether a complete gap or pseudogap exists in Cr_3Al. The current experimental and theoretical results are consistent with a pseudogap, with low but nonzero density of states existing at the Fermi energy. However, this could be caused by, experimentally, incomplete ordering of the X-phase structure and, theoretically, by the tendency for density-functional theory to underestimate the size of band gaps. More advanced density-functional theoretical calculations and extremely careful sample growth techniques may be able to resolve this question.

Bibliography

[1] H. Akai. Fast Korringa-Kohn-Rostoker coherent potential approximation and its application to FCC Ni-Fe systems. *Journal of Physics: Condensed Matter*, 1:8045, 1989.

[2] Hisazumi Akai. [online] http://sham.phys.sci.osaka-u.ac.jp/kkr/.

[3] Hisazumi Akai and Junjiro Kanamori. Antiferromagnetic susceptibility of chromium alloys with non-transition metal elements. *Journal of the Physical Society of Japan*, 54:3537, 1985.

[4] P. B. Allen. Empirical electron-phonon λ values from resistivity of cubic metallic elements. *Physical Review B*, 36:2920, 1987.

[5] M. A. Angadi and L. A. Udachan. The effect of substrate temperature on the electrical properties of thin chromium films. *Journal of Materials Science*, 16:1412, 1981.

[6] S. B. Arnason, S. P. Herschfield, and A. F. Hebard. Bad metals made with good-metal components. *Physical Review Letters*, 81:3936, 1998.

[7] Setsuro Asano and Jiro Yamashita. Band theory of antiferromagnetic chromium. *Journal of the Physical Society of Japan*, 23:714, 1967.

[8] M. Atoji. Antiferromagnetic structure of $AlCr_2$. *The Journal of Chemical Physics*, 43:222, 1965.

[9] G. E. Bacon and N. Cowlam. Magnetic studies of annealed and alloyed chromium by neutron diffraction. *Journal of Physics C*, 2:238, 1969.

[10] M. N. Baibich, J. M. Broto, A. Fert, F. Nguyen Van Dau, F. Petroff, P. Etienne, G. Creuzet, A. Friederich, and J. Chazelas. Giant magnetoresistance of (001)Fe/(001)Cr magnetic superlattices. *Physical Review Letters*, 61:2472, 1988.

[11] Jack Bass. Deviations from Matthiessen's rule. *Advances in Physics*, 21:431, 1972.

[12] M. Birkholz. *Thin Film Analysis by X-Ray Scattering*. Wiley-VCH, Weinheim, 2006.

[13] Z. Boekelehide, A. X. Gray, C. Papp, B. Balke, D. A. Stewart, S. Ueda, K. Kobayashi, F. Hellman, and C. S. Fadley. Band gap and electronic structure of an epitaxial, semiconducting $Cr_{0.80}Al_{0.20}$ thin film. *Physical Review Letters*, 105:236404, 2010.

[14] Z. Boekelheide, David W. Cooke, E. Helgren, and F. Hellman. Resonant impurity scattering and electron-phonon scattering in the electrical resistivity of Cr thin films. *Physical Review B*, 80:134426, 2009.

[15] Z. Boekelheide, E. Helgren, and F. Hellman. Spin-density wave in polycrystalline Cr films from infrared reflectivity. *Physical Review B*, 76:224429, 2007.

[16] Lawrence W. Bos and David W. Lynch. Optical properties of antiferromagnetic chromium and dilute Cr-Mn and Cr-Re alloys. *Physical Review B*, 2:4567, 1970.

[17] S. D. Brorson, A. Kazeroonian, J. S. Moodera, D. W. Face, T. K. Cheng, E. P. Ippen, M. S. Dresselhaus, and G. Dresselhaus. Femtosecond room-temperature measurement of the electron-phonon coupling constant λ in metallic superconductors. *Physical Review Letters*, 64:2172, 1990.

[18] D. J. Chakrabarti and P. A. Beck. Transport properties of Cr-Al solid solutions. *Journal of Physics and Chemistry of Solids*, 32:1609, 1971.

[19] C. H. Chiu, M. H. Jericho, and R. H. March. Magnetic susceptibility and electrical resistivity of dilute chromium-titanium alloys. *Canadian Journal of Physics*, 49:3010, 1971.

[20] Kurt J. Lesker Company. Material Deposition Reference Tables, 2008. [online] http://www.lesker.com/newweb/menu_techinfo.cfm.

[21] David W. Cooke. *Thermodynamic Measurements of Applied Magnetic Materials*. PhD thesis, University of California -Berkeley, 2010.

[22] David W. Cooke, Z. Boekelheide, D. R. Queen, and F. Hellman. The role of the spin-density wave and disorder in the density of states of sputtered Cr films. *Journal of Applied Physics*, 105:07C314, 2009.

[23] M. C. Cyrille, S. Kim, M. E. Gomez, J. Santamaria, C. Leighton, Kannan M. Krishnan, and Ivan K. Schuller. Effect of sputtering pressure-induced roughness on the microstructure and perpendicular giant magnetoresistance of Fe/Cr superlattices. *Physical Review B*, 62:15079, 2000.

[24] F. J. A. den Broeder, G. van Tendeloo, S. Amelinckx, J. Hornstra, R. de Ridder, J. van Landuyt, and H. J. van Daal. Microstructure of $Cr_{100-x}Al_x$ alloys (10 at% <x <33 at%) studied by means of transmission electron microscopy and diffraction II. Discovery of a new phase. *Physica Status Solidi A*, 67:233, 1981.

[25] C. J. Doherty, J. M. Poate, and R. J. H. Vorhoeve. Vacuum-evaporated films of chromium with the A-15 structure. *Journal of Applied Physics*, 48:2050, 1977.

[26] J. S. Dugdale. *The Electrical Properties of Metals and Alloys*. Edward Arnold, London, 1977.

[27] Milo A. Durand. The coefficient of thermal expansion of magnesium oxide. *Physics A: Journal of General and Applied Physics*, 7:297, 1936.

[28] L. M. Falicov and David R. Penn. Concentration dependence of the spin-density-wave periodicity in antiferromagnetic chromium alloys. *Physical Review*, 158:476, 1967.

[29] A. Fathalizadeh and Z. Boekelheide. Electric and magnetic characterization of sputtered iron thin films and the implications for chromium thin films. *Berkeley Scientific*, 11:29, 2007.

[30] E. Fawcett. Spin-density-wave antiferromagnetism in chromium. *Reviews of Modern Physics*, 60:209, 1988.

[31] E. Fawcett, H. L. Alberts, V. Yu. Galkin, D. R. Noakes, and J. V. Yakhmi. Spin-density-wave antiferromagnetism in chromium alloys. *Reviews of Modern Physics*, 66:25, 1994.

[32] J. L. Feldman. Lattice-vibrational properties of chromium in the harmonic approximation on the basis of the tensor model. *Physical Review B*, 1:448, 1970.

[33] Y. Feng, R. Jaramillo, G. Srajer, J. C. Lang, Z. Islam, M. S. Somayazulu, O. G. Shpyrko, J. J. Pluth, H. k Mao, E. D. Isaacs, G. Aeppli, and T. F. Rosenbaum. Pressure-tuned spin and charge ordering in an itinerant antiferromagnet. *Physical Review Letters*, 99:137201, 2007.

[34] A. Fert. The origin, development, and future of spintronics. *Les Prix Nobel 2007*, page 59, 2008.

[35] Paul F. Fewster. X-ray analysis of thin films and multilayers. *Reports on Progress in Physics*, 59:1339, 1996.

[36] Simon Foner. Hall effect in titanium, vanadium, chromium, and manganese. *Physical Review*, 107:1513, 1957.

[37] JCPDS International Centre for Diffraction Data. PCPDFWIN software v. 2.02, 1999.

[38] Eric E. Fullerton, S. D. Bader, and J. L. Robertson. Spin-density-wave antiferromagnetism of Cr in Fe/Cr(001) superlattices. *Physical Review Letters*, 77:1382, 1996.

[39] Eric E. Fullerton, M. J. Conover, J. E. Mattson, C. H. Sowers, and S. D. Bader. Oscillatory interlayer coupling and giant magnetoresistance in epitaxial Fe/Cr(211) and (100) superlattices. *Physical Review B*, 48:15755, 1993.

[40] Eric E. Fullerton, K. T. Riggs, C. H. Sowers, S. D. Bader, and A. Berger. Suppression of biquadratic coupling in Fe/Cr(001) superlattices below the Néel transition of Cr. *Physical Review Letters*, 75:330, 1995.

[41] Brent Fulz and James Howe. *Transmission Electron Microscopy and Diffractometry of Materials.* Springer, New York, 2002.

[42] Yhuzi Furuya. Temperature and magnetic field dependence of the hall coefficient on the antiferromagnetic chromium. *Journal of the Physical Society of Japan*, 40:490, 1976.

[43] Iosif Galanakis, Kemal Özdoğan, Ersoy Şaşioğlu, and Bekir Aktaş. Ferrimagnetism and antiferromagnetism in half-metallic Heusler alloys. *Physica Status Solidi A*, 205:1036, 2008.

[44] V. Yu Galkin. Resonance scattering of band electrons by localized impurity states in chromium-base antiferromagnetic alloys. *Fizika metallov i metallovedenie*, 64:1199, 1987.

[45] V. Yu Galkin, V. V. Tugushev, and T. E. Tugusheva. Resonance impurity scattering in dilute Cr-Fe-M (M = Mn,V) alloys. *Soviet Physics Solid State*, 28:1282, 1986.

[46] V. Yu Galkin and T. E. Tugusheva. Relationship between an anomalous temperature dependence of the electrical resistivity and resonance impurity scattering in dilute Cr-Fe alloys. *Soviet Physics Solid State*, 30:487, 1988.

[47] V. Yu Galkin and T. E. Tugusheva. Resonant impurity scattering in dilute chromium alloy swith an incommensurate structure of the spin density wave. *Soviet Physics Solid State*, 31:1626, 1989.

[48] J. F. Goff. Multiband model for the electronic heat capacity of chromium. *Physical Review B*, 4:1121, 1971.

[49] P. A. Gould. The resistivity and structure of chromium thin films. *British Journal of Applied Physics*, 16:1481, 1965.

[50] G. Grimvall. The electron-phonon interaction in normal metals. *Physica Scripta*, 14:63, 1976.

[51] Stacy Group. Stacy Group Lab Tour, 2011. [online] http://www.cchem.berkeley.edu/amsgrp/tour.html.

[52] M. Gurvitch. Ioffe-Regel criterion and resistivity of metals. *Physical Review B*, 24:7404, 1981.

[53] R. Hafner, D. Spišák, R. Lorenz, and J. Hafner. Magnetic ground state of Cr in density-functional theory. *Physical Review B*, 65:184432, 2002.

[54] F. Heiniger, E. Bucher, and J. Muller. Low temperature specific heat of transition metals and alloys. *Physik der Kondensierten Materie*, 5:243, 1966.

[55] D. W. Hoffman and M. R. Gaerttner. Modification of evaporated chromium by concurrent ion bombardment. *Journal of Vacuum Science and Technology*, 17:425, 1980.

[56] D. W. Hoffman and John A. Thornton. Internal stresses in sputtered chromium. *Thin Solid Films*, 40:355, 1977.

[57] D. W. Hoffman and John A. Thornton. Effects of substrate orientation and rotation on internal stresses in sputtered metal films. *Journal of Vacuum Science and Technology*, 16:134, 1979.

[58] D. W. Hoffman and John A. Thornton. Internal stresses in Cr, Mo, Ta, and Pt films deposited by sputtering from a planar magnetron source. *Journal of Vacuum Science and Technology*, 20:355, 1982.

[59] U. Holzwarth and H. Stamm. Mechanical and thermomechanical properties of commercially pure chromium and chromium alloys. *Journal of Nuclear Materials*, 300:161, 2002.

[60] Ayahiko Ichimiya and Philip I. Cohen. *Reflection high energy electron diffraction.* Cambridge University Press, New York, 2004.

[61] Sycon instruments. *User's Manual for Sycon instruments STC-2000A Deposition Rate Controller*, 2006.

[62] A. Kallel and F. deBergevin. Antiferromagnetisme de la solution solide de l'aluminium dans le chrome. *Solid State Communications*, 5:955, 1967.

[63] K. Kimoto and I. Nishida. A new modification of chromium. *Journal of the Physical Society of Japan*, 20:1963, 1965.

[64] K. Kimoto and I. Nishida. Crystal structure of very small particles of chromium and iron. *Thin Solid Films*, 17:49, 1973.

[65] C. Kittel. *Introduction to Solid State Physics.* John Wiley & Sons, New York, 1996.

[66] L. E. Klebanoff and D. A. Shirley. Surface dependence of the Cr(001) 3s photoemission line shape. *Physical Review B*, 33:5301, 1986.

[67] T. J. Klemmer, V. R. Inturi, M. K. Minor, and J. A. Barnard. Exchange induced unidirectional anisotropy observed using Cr-Al antiferromagnetic films. *Applied Physics Letters*, 70:2915, 1997.

[68] K. Kobayashi. Hard x-ray photoemission spectroscopy. *Nuclear Instruments and Methods A*, 601:32, 2009.

[69] K. Kobayashi, M. Yabashi1, Y. Takata, T. Tokushima, S. Shin, K. Tamasaku, D. Miwa, T. Ishikawa, H. Nohira, T. Hattori, Y. Sugita, O. Nakatsuka, A. Sakai, and S. Zaima. High resolution-high energy x-ray photoelectron spectroscopy using third-generation synchrotron radiation source, and its application to Si-high k insulator systems. *Applied Physics Letters*, 83:1005, 2003.

[70] W. Kohn and N. Rostoker. Solution of the Schrödinger equation in periodic lattices with an application to metallic lithium. *Physical Review*, 94:1111, 1954.

[71] J. Korringa. On the calculation of the energy of a Bloch wave in a metal. *Physica*, 13:392, 1947.

[72] W. Koster, E. Wachtel, and K. Grube. Aufbau und magnetische eigenschaften der aluminium-chrom-legierungen. *Zeitschrift fur Metallkunde*, 54:393, 1963.

[73] E. V. Kozlov, B. S. Semukhin, L. M. Rubinovich, and D. M. Shtern. Investigation of the order-disorder transformation in AlCr$_2$. *Fizika metallov i metallovedenie*, 56:547, 1983.

[74] A. Kubetzka, M. Bode, O. Pietzsch, and R. Wiesendanger. Spin-polarized scanning tunneling microscopy with antiferromagnetic probe tips. *Physical Review Letters*, 88:057201, 2002.

[75] J. Kübler, A. R. Williams, and C. B. Sommers. Formation and coupling of magnetic moments in Heusler alloys. *Physical Review B*, 28:1745, 1983.

[76] A. K. Kulkarni and L. C. Chang. Electrical and structural characteristics of chromium thin films deposited on glass and alumina substrates. *Thin Solid Films*, 301:17, 1997.

[77] K. S. Kumar, H. Van Swygenhoven, and S. Suresh. Mechanical behavior of nanocrystalline metals and alloys. *Acta Materialia*, 51:5743, 2003.

[78] D. G. Laurent, J. Callaway, J. L. Fry, and N. E. Brener. Band structure, Fermi surface, Compton profile, and optical conductivity of paramagnetic chromium. *Physical Review B*, 23:4977, 1981.

[79] K. Ławniczak-Jabłońska, E. Minni, J. Pełka, E. Suoninen, and J. Auleytner. XPS and XES study of the valence band of Cr-Al B.C.C. solid solutions. *Physica Status Solidi B*, 123:627, 1984.

[80] C. G. Lee, B. S. Kim, and K. Fukamichi. Fabrication of Cr-Al based multilayer spin valve with anti-corrosion and thermal stability. *IEEE Transactions on Magnetics*, 35:2928, 1999.

[81] Jia Li, Hongjian Chen, Yangxian Li, Yu Xiao, and Zhiqing Li. A theoretical design of half-metallic compounds by a long range of doping Mn for Heusler-type Cr$_3$Al. *Journal of Applied Physics*, 105:083717, 2009.

[82] M. A. Lind and J. L. Stanford. Optical measurements of the antiferromagnetic energy gaps in chromium. *Physics Letters*, 39A:5, 1972.

[83] M. A. Lind and J. L. Stanford. Measurements of the temperature dependence of energy gaps in magnetically-ordered Cr-rich Cr-Al alloys. *Journal of the Physical Society of Japan*, 53:4029, 1984.

[84] R. M. Martin. *Electronic Structure: Basic Theory and Practical Methods*. Cambridge University Press, New York, 2005.

[85] M. Mayer. SIMNRA, a Simulation Program for the Analysis of NRA, RBS and ERDA. *Proceedings of the 15th Inernational Conference on the Application of Accelerators in Research and Industry, American Institute of Physics Conference Proceedings*, 475:541, 1999.

[86] W. L. McMillan. Transition temperature of strong-coupled superconductors. *Physical Review*, 167:331, 1968.

[87] G. T. Meaden. *Electrical Resistance of Metals*. Plenum Press, New York, 1965.

[88] J. H. Mooij. Electrical conduction in concentrated disordered transition metal alloys. *Physica Status Solidi A*, 17:521, 1973.

[89] J. L. Murray. The Al-Cr (aluminum-chromium) system. *Joural of Phase Equilibria*, 19:367, 1998.

[90] Y. Nishino, M. Kato, S. Asano, K. Soda, M. Hayasaki, and U. Mizutani. Semiconductorlike behavior of electrical resistivity in Heusler-type Fe_2VAl compound. *Physical Review Letters*, 79:1909, 1997.

[91] L. V. Nomerovannaya and V. A. Rassokhin. Anomalies in the optical and electrical properties of Cr-Al alloys. *Physica Status Solidi A*, 79:87, 1983.

[92] P. Juichiro Ozawa, Sadao Yoshizaki, Shizuka Takeyama, Toshio Enjo, and Kenji Ikeuchi. *IEEE Transactions on Components, Hybrids, and Manufacturing Technology*, CHMT-9:391, 1986.

[93] J. S. Parker, L. Wang, K. A. Steiner, P. A. Crowell, and C. Leighton. Exchange bias as a probe of the incommensurate spin-density wave in epitaxial Fe/Cr(001). *Physical Review Letters*, 97:227206, 2006.

[94] J. P. Perdew, J. A. Chevary, S. H. Vosko, K. A. Jackson, M. R. Pederson, D. J. Singh, and C. Fiolhais. Atoms, molecules, solids, and surfaces: Applications of the generalized gradient approximation for exchange and correlation. *Physical Review B*, 46:6671, 1992.

[95] N. Pessall, K. P. Gupta, C. H. Cheng, and Paul A. Beck. Low temperature specific heat of B.C.C. alloys of 3d transition elements and aluminum. *Journal of Physics and Chemistry of Solids*, 25:993, 1964.

[96] A. R. E. Prinsloo, H. L. Alberts, and P. Smit. Electrical transport properties of Cr-Si and Cr-Ga alloy single crystals. *Journal of Physics: Condensed Matter*, 10:2715, 1998.

[97] A. R. E. Prinsloo, H. A. Derrett, H. L. Alberts, and A. M. Venter. Magnetic effects in an itinerant electron antiferromagnetic Cr + 1.72 at. % Fe alloy single crystal. *Journal of Applied Physics*, 99:08F706, 2006.

[98] V. G. Pynko and E. Z.-R. Lyudvik. Epitaxial film growth of b.c.c. metals on the cleavage surface of NaCl crystals. *Thin Solid Films*, 32:101, 1976.

[99] J. A. Rayne and W. R. G. Kemp. XCIII. The heat capacities of chromium and nickel. *Philosophical Magazine*, 1:918, 1956.

[100] L. Reddy, H. L. Alberts, A. M. Strydom, A. R. E. Prinsloo, and A. M. Venter. Quantum critical behavior of the $(Cr_{86}Ru_{14})_{1-x}V_x$ alloy system. *Journal of Applied Physics*, 103:07C903, 2008.

[101] F. Reniers, M. P. Delplancke, A. Asskali, V. Rooryck, and O. Van Sinay. Glow discharge sputtering deposition of thin films of Ag, Cr, Cu, Ni, Pd, Rh and their binary alloys onto NaCl and MgO: Experimental parameters and epitaxy. *Applied Surface Science*, 92:35, 1996.

[102] B. Revaz, M.-C. Cyrille, B. L. Zink, Ivan K. Schuller, and F. Hellman. Enhancement of the electronic contribution to the low-temperature specific heat of an Fe/Cr magnetic multilayer. *Physical Review B*, 65:094417, 2002.

[103] K. T. Roro, A. R. E. Prinsloo, and H. L. Alberts. Influence of V and Mn doping on the electrical transport properties of a Cr + 1.2 at. % Ga alloy. *Journal of Alloys and Compounds*, 393:16, 2005.

[104] Eli Rotenberg, B. K. Freelon, H. Koh, A. Bostwick, K. Rossnagel, Andreas Schmid, and S. D. Kevan. Electron states and the spin density wave phase diagram in Cr(110) films. *New Journal of Physics*, 7:114, 2005.

[105] S. Roth and J. Sonntag. Temperature dependence of the electrical resistivity of semi-conducting CrAl solid solutions at high temperatures. *Physica Status Solidi B*, 87:K69, 1978.

[106] J. H. Scofield. Theoretical photoionization cross sections from 1 to 1500 keV. Technical Report UCRL-51326, LLNL, 1973.

[107] G. Shimaoka. Preferential epitaxy of evaporated thin films produced by charged particles on NaCl substrates. *Surface Science*, 86:182, 1979.

[108] W. Smekal, W. S. M. Werner, and C. J. Powell. Simulation of electron spectra for surface analysis (SESSA): a novel software tool for quantitative Auger-electron spectroscopy and x-ray photoelectron spectroscopy. *Surface and Interface Analysis*, 37:1059, 2005.

[109] Donald L. Smith. *Thin-Film Deposition: Principles & Practice*. McGraw Hill, San Francisco, 1995.

[110] G. J. Snyder and E. S. Toberer. Complex thermoelectric materials. *Nature Materials*, 7:105, 2008.

[111] J. O. Sofo and G. D. Mahan. Optimum band gap of a thermoelectric material. *Physical Review B*, 49:4565, 1994.

[112] P. Soven. Coherent-potential model of substitutional disordered alloys. *Physical Review*, 156:809, 1967.

[113] J. O. Strom-Olsen, D. F. Wilford, and A. P. Morris. Electrical resistance of single-crystal single-domain chromium from 77 to 325 K. *Journal of Physics F*, 12:1247, 1982.

[114] H. Stupp, M. Hornung, M. Lakner, O. Madel, and H. v. Löhneysen. Possible solution of the conductivity exponent puzzle for the metal-insulator transition in heavily doped uncompensated semiconductors. *Physical Review B*, 71:2634, 1993.

[115] L. S. Suominen, C. Zhou, M. A. Korhonen, and C.-Y. Li. X-ray study of residual stresses in thin chromium metallizations on glass substrates. *Advances in X-ray Analysis*, 40:544, 1996.

[116] SPI Supplies. SPI-Chem[TM] Sodium Chloride Single Crystal Substrates, 2011. [online] http://www.2spi.com/catalog/submat/substr.shtml.

[117] V. N. Svechnikov, G. F. Kobzenko, V. G. Ivanchenko, and E. L. Martynchuk. Cr-N Phase Diagram. In P. Villars, editor-in-chief; H. Okamoto and K. Cenzual, editor, *ASM Alloy Phase Diagrams Center*. ASM International, Materials Park, OH, 2006. http://www1.asminternational.org/AsmEnterprise/APD.

[118] SVT Associates, Inc. Effusion Cells - Source Selection Guide, 2010. [online] http://svtald.com/products/sources/effusion.htm.

[119] Y. Takata, Y. Kayanuma, S. Oshima, S. Tanaka, M. Yabashi, K. Tamasaku, Y. Nishino, M. Matsunami, R. Eguchi, A. Chainani, M. Oura, T. Takeuchi, Y. Senba, H. Ohashi, S. Shin, and T. Ishikawa. Recoil effect of photoelectrons in the fermi edge of simple metals. *Physical Review Letters*, 101(13):137601, 2008.

[120] S. Tanuma, C. J. Powell, and D. R. Penn. Calculations of electron inelastic mean free paths. *Surface and Interface Analysis*, 37:1, 2005.

[121] John A. Thornton and David W. Hoffman. Internal stresses in titanium, nickel, molybdenum, and tantalum films deposited by cylindrical magnetron sputtering. *Journal of Vacuum Science and Technology*, 14:164, 1977.

[122] M. B. Trzhaskovskaya, V. I. Nefedov, and V. G. Yarzhemsky. Photoelectron angular distribution parameters for elements $Z=1$ to $Z=54$ in the photoelectron energy range 100-5000 eV. *Atomic Data and Nuclear Data Tables*, 77:97, 2001.

[123] M. B. Trzhaskovskaya, V. K. Nikulin, V. I. Nefedov, and V. G. Yarzhemsky. Nondipole second order parameters of the photoelectron angular distribution for elements $Z=1100$ in the photoelectron energy range 110 keV. *Atomic Data and Nuclear Data Tables*, 92:245, 2006.

[124] S. Tsukimoto, F. Phillipp, and T. Wagner. Texture of MBE grown Cr films on α-Al_2O_3(0001): the occurrence of Nishiyama-Wassermann (NW) and Kurdiumov-Sachs (KS) related orientation relationships. *Journal of the European Ceramic Society*, 23:2947, 2003.

[125] C. Uher, J. Yang, S. Hu, D. T. Morelli, and G. P. Meisner. Transport properties of pure and doped MNiSn ($M=$Zr, Hf). *Physical Review B*, 59:8615, 1999.

[126] L. Vegard. Die Konstitution der Mischkristalle und die Raumfüllung der Atome. *Zeitschrift für Physik*, 5:17, 1921.

[127] B. A. Volkov and V. V. Tugushev. Formation of local magnetic moments and resonant scattering in dilute chromium alloys containing nonmagnetic impurities. *Soviet Physics Solid State*, 26:1471, 1984.

[128] T. Wagner, Q. Fu, C. Winde, S. Tsukimoto, and F. Phillipp. A comparative study of the growth of Cr on (110) TiO_2 rutile, $(0001)\alpha$-Al_2O_3 and $(100)SrTiO_3$ surfaces. *Interface Science*, 12:117, 2004.

[129] M. Weinert and R. E. Watson. Hybridization-induced band gaps in transition-metal aluminides. *Physical Review B*, 58:9732, 1998.

[130] G. K. White and S. B. Woods. Electrical and thermal resistivity of the transition elements at low temperatures. *Philosophical Transactions of the Royal Society of London, Series A*, 251:273, 1959.

[131] Wikipedia. Electron diffraction, 2011. [online] http://en.wikipedia.org/wiki/Electron_diffraction.

[132] Wikipedia. Scanning electron microscope, 2011. [online] http://en.wikipedia.org/wiki/Scanning_electron_microscope.

[133] Wikipedia. Semimetal, 2011. [online] http://en.wikipedia.org/wiki/Semimetal.

[134] Wikipedia. Structure factor, 2011. [online] http://en.wikipedia.org/wiki/Structure_factor.

[135] I. S. Williams and R. Street. The effect of tensile stress on the Néel temperature in chromium. *Philosophical Magazine B*, 43:955, 1981.

[136] R. Xu and T.-C. Chiang. Observation of phonon softening in Cr near its Neel transition. In *APS March Meeting*, Dallas, TX, 2011. http://meetings.aps.org/link/BAPS.2011.MAR.X22.2.

[137] L. Zeng, E. Helgren, F. Hellman, R. Islam, and D. J. Smith. Growth and microstructure dependence of electronic and magnetic properties in magnetically doped Gd-Si amorphous semiconductors. *Physical Review B*, 75:184404, 2007.

[138] S. M. Zhou, Kai Liu, and C. L. Chien. Dependence of exchange coupling in permalloy/$Cr_{82}Al_{18}$ bilayers on the constituent layer thickness. *Journal of Applied Physics*, 87:6659, 2000.